COMPUTATIONAL MODELING OF FRONTAL POLYMERIZATION

A THESIS SUBMITTED TO
THE GRADUATE SCHOOL OF NATURAL AND APPLIED SCIENCES
OF
MIDDLE EAST TECHNICAL UNIVERSITY

BY

KORAY KAYA

IN PARTIAL FULFILLMENT OF THE REQUIREMENTS
FOR
THE DEGREE OF MASTER OF SCIENCE
IN
CIVIL ENGINEERING

FEBRUARY 2022

Approval of the thesis:

COMPUTATIONAL MODELING OF FRONTAL POLYMERIZATION

submitted by **KORAY KAYA** in partial fulfillment of the requirements for the degree of **Master of Science in Civil Engineering Department, Middle East Technical University** by,

Prof. Dr. Halil Kalıpçılar
Dean, Graduate School of **Natural and Applied Sciences**   ——————

Prof. Dr. Erdem Canbay
Head of Department, **Civil Engineering**   ——————

Assoc. Prof. Dr. Serdar Göktepe
Supervisor, **Civil Engineering, METU**   ——————

Examining Committee Members:

Prof. Dr. Kağan Tuncay
Civil Engineering, METU   ——————

Assoc. Prof. Dr. Serdar Göktepe
Civil Engineering, METU   ——————

Assoc. Prof. Dr. Ercan Gürses
Aerospace Engineering, METU   ——————

Assoc. Prof. Dr. Barış Sabuncuoğlu
Mechanical Engineering, Hacettepe Universtiy   ——————

Assoc. Prof. Dr. İzzet Özdemir
Civil Engineering, İzmir Institute of Technology   ——————

Date:09.02.2022

I hereby declare that all information in this document has been obtained and presented in accordance with academic rules and ethical conduct. I also declare that, as required by these rules and conduct, I have fully cited and referenced all material and results that are not original to this work.

Name, Surname: Koray Kaya

Signature   :

ABSTRACT

COMPUTATIONAL MODELING OF FRONTAL POLYMERIZATION

Kaya, Koray

M.S., Department of Civil Engineering

Supervisor: Assoc. Prof. Dr. Serdar Göktepe

February 2022, 112 pages

Polymer-based composites are widely applied in high-tech areas such as aerospace, automotive, marine, and energy industries where high performance under extreme conditions is crucial. However, the traditional methods used to manufacture polymeric materials are energy-inefficient, time-consuming, complex, and costly processes. Frontal polymerization, an alternative curing method, is based on a self-propagating, self-sustained exothermic reaction front that transforms liquid monomers into cured polymers where the disadvantages of traditional polymerization techniques are minimized. Furthermore, frontal polymerization opens up new possibilities for many new manufacturing concepts such as on-demand manufacturing, on-site, shapeless production, 3-D printing, and resin-infusion. Despite the intensive studies on the chemothermal aspects of frontal polymerization, the impact of the chemical shrinkage, the sharp temperature gradients, the temperature distribution, and the front velocity on the mechanical behavior of frontally produced polymers, especially on the development of the stress accumulations, remains unexamined to a great extent. This thesis, therefore, aims to develop novel constitutive models furnished with robust computational tools to describe the coupled process of frontal polymerization and the behavior of polymeric materials produced by frontal polymerization. To this end, the

thermodynamically consistent incremental framework of finite elasticity coupled with the inherent chemothermal fields is developed. In turn, this multi-field coupling allows us to calculate the accumulated stresses due to the chemically induced shrinkage and thermal expansion. Undoubtedly, the quantitative prediction of stress accumulations is of key importance to optimize the process of frontal polymerization towards the production of mechanically stronger and tougher polymer composites.

ÖZ

CEPHESEL POLİMERLEŞMENİN HESAPLAMALI MODELLENMESİ

Kaya, Koray
Yüksek Lisans, İnşaat Mühendisliği Bölümü
Tez Yöneticisi: Doç. Dr. Serdar Göktepe

Şubat 2022 , 112 sayfa

Polimer bazlı kompozitler zorlu koşullar altında yüksek performansın çok önemli olduğu havacılık, otomotiv, denizcilik ve enerji endüstrileri gibi yüksek teknolojili alanlarında yaygın olarak kullanılmaktadır. Öte yandan polimerik malzemeleri üretmek için kullanılan geleneksel yöntemler, enerji açısından verimsiz, zaman alıcı, karmaşık ve maliyetli tekniklerdir. Alternatif bir kürleme yöntemi olan cephesel polimerleşme, sıvı monomerleri polimerlere dönüştürürken geleneksel polimerleşme yöntemlerinin dezavantajlarını en aza indiren, reaksiyon cephesinin kendi kendine ilerleyip, kendi kendine devam eden ekzotermik tepkimeyi temel alan bir yöntemdir. Buna ek olarak, cephesel polimerleşme, talebe bağlı üretim, yerinde üretim, kalıpsız üretim, 3B baskı ve reçine infüzyonu gibi birçok yeni üretim yöntem olanakları sunmaktadır. Cephesel polimerizasyonun kemotermal yönleri üzerine yapılan yoğun çalışmalara rağmen, kimyasal büzülmenin, keskin sıcaklık gradyanlarının, sıcaklık dağılımının ve tepkime cephesinin hızının üretilen polimerlerin mekanik davranışı özellikle de gerilme birikimlerinin oluşumu üzerine etkisi hala büyük ölçüde incelenmemiştir. Buradan hareketle bu tez çalışması polimerleşmenin bağlaşık sürecini ve bu yöntem ile üretilen polimerik malzemelerin davranışını açıklamak için sağlam hesaplama araç-

ları ile donanmış yeni bünye denklemleri geliştirmeyi amaçlamaktadır. Bu amaçla, polimerleşmenin doğası gereği var olan kemotermal reaksiyonlar ile birleştirilmiş, artımlı çerçevede, termodinamik olarak tutarlı doğrusal olmayan elastik bir model geliştirilmiştir. Buna karşılık, bu çok alanlı bağlaşıklık kimyasal büzülme ve ısıl genleşme nedeniyle oluşan birikmiş gerilmeleri hesaplanmasına olanak sağlamaktadır. Kuşkusuz, mekanik olarak daha güçlü ve daha sağlam polimer kompozitlerin üretimini sağlayan cephesel polimerleşme işlemini eniyilemek için bu gerilmelerin nicel kestirimi kilit öneme sahiptir.

Anahtar Kelimeler: Cephesel Polimerizasyon, Kemo-Termo-Mekanik Model, Hesaplamalı Modelleme, Gerilme Birikimleri

To all my loved ones

ACKNOWLEDGMENTS

TABLE OF CONTENTS

LIST OF TABLES

TABLES

LIST OF FIGURES

FIGURES

LIST OF ABBREVIATIONS

2D	Two Dimensional
3D	Three Dimensional
FROMP	Frontal Ring-Opening Metathesis Polymerization
DCPD	Dicyclopentadiene
COD	Cyclooctadiene
DMA	Dynamic Mechanical Analysis
CTE	Thermal Expansion Coefficient
CCS	Coefficient of Cure Shrinkage
FRP	Fiber Reinforced Plastics
NMT	Numerical Material Test
DOC	Degree of Curing
PSU	Polyisocyanurate
DIC	Digital Image Correlation

CHAPTER 1

INTRODUCTION

1.1 Motivation and Objectives of Study

The frontal polymerization technique offers a cheaper, faster, and energy-efficient option for polymer-composite industries through a highly localized and self-propagating exothermic reaction zone where monomers polymerize into macromolecules [1].
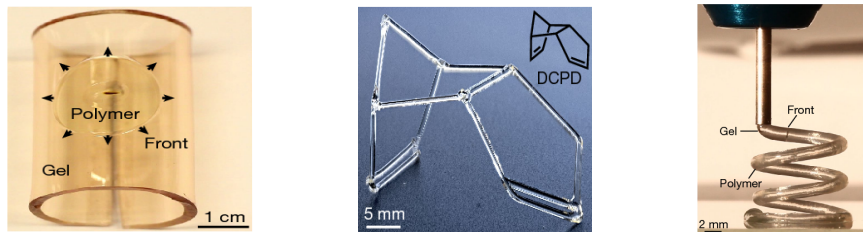
Figure 1.1: The examples of the polymer frontally cured [1]

Polymer-based composites are widely applied materials in many industries thereby allowing engineers to build strikingly impressive structures that were once unimaginable. For instance, SpaceX® has recently demonstrated the largest carbon fiber reinforced polymer fuel tank that has ever been manufactured for spacecraft. These materials offer new opportunities to keep the weight down while maintaining the strength at a level adequate to resist the internal pressure. It is an extremely challenging task to build a spaceship of this huge size. One of the challenges building such a giant structure monolithically made up of polymer-composite through traditional methods is that there exist no sufficiently big autoclave in the world to fit the tank spacecraft to attain the best quality of production. Hence, frontal polymerization is a breakthrough solution for these types of production owing to the self-sustained, self-propagating fast front driven by the exothermic reaction of polymerization.

It is now well-known that the climate change and environmental problems are among the most important challenges in the world. The main reason for these problems is the industrial processes [1]. For example, the curing of a small section of carbon fiber fuselage of the Boeing $787^{\circledR}$ requires about 350 giga Joules during an eight-hour cure cycle. Furthermore, it produces more than 80 tons of carbon dioxide. However, these materials can be produced with less energy, less cost, and reduced environmental impact using frontal polymerization. Also, according to Sottos and co-workers [4], the energy savings of polymer produced through frontal polymerization is up to 10 orders of magnitude as compared with the traditinal techniques of polymerization. Moreover, the resulting polymer composites have similar mechanical properties to those produced conventionally. Thus, these materials are practically widely applicable to various industries such as aerospace, automotive, energy to mention a few.

The frontal polymerization technique is based on useful autocatalytic reaction that rapidly transforms monomer to polymer upon a small thermal initiator [5]. Thus, there are possible advantages of using the frontal polymerization technique over the conventional methods of polymerization. The major ones being the speed at which a sample can be cured, the avoidance of autoclave and charring from thermal run away. However, there are some limitations associated with frontal polymerization. The limited pot life of the system is one of the principal issues. In addition, only the chemical, thermomechanical, and front propagation properties of the frontal polymerization technique have been studied until now. For example, Goli et al. [3] have studied the frontal polymerization of neat resins analytically and Goldfeder and Volpert [6] have estimated the rate of conversion of monomer and front velocity in an adiabatic system. However, there are several missing aspects in the literature regarding frontal polymerization. The development of a constitutive model accounting for chemo-thermo-mechanical coupling throughout the continuous curing process for frontally polymerized material is probably one of the most important and challenging aspects remained unstudied in the literature.

This thesis work, therefore, aims to develop novel constitutive models furnished with robust computational tools to describe the process of frontal polymerization and the behavior of polymeric materials produced by frontal polymerization. To this end, the incremental models of finite elasticity coupled with the inherent thermal and chemical

2

effects for the frontally polymerized materials are proposed. To our best knowledge, this is the first study where the coupled chemo-thermo-mechanical aspects of frontal polymerization are accounted for an aging (phase changing: monomer to polymer) material in the thermodynamically consistent framework and incremental setting. In turn, this multi-field coupling allows us to predict the accumulation of stresses due to the chemically induced shrinkage and thermal volume changes. Undoubtedly, the quantitative prediction of these stress accumulations of key importance to optimize the process of frontal polymerization towards the production of mechanically stronger and tougher polymer composites.

1.2 Polymerization and Manufacturing Techniques

Before we overview the literature on the experimental and analytical studies on frontal polymerization, it is worth summarizing the basic techniques of polymerization [7]. There are four different main techniques of polymerization. These conventional methods are commonly used for commercial production as summarized below.
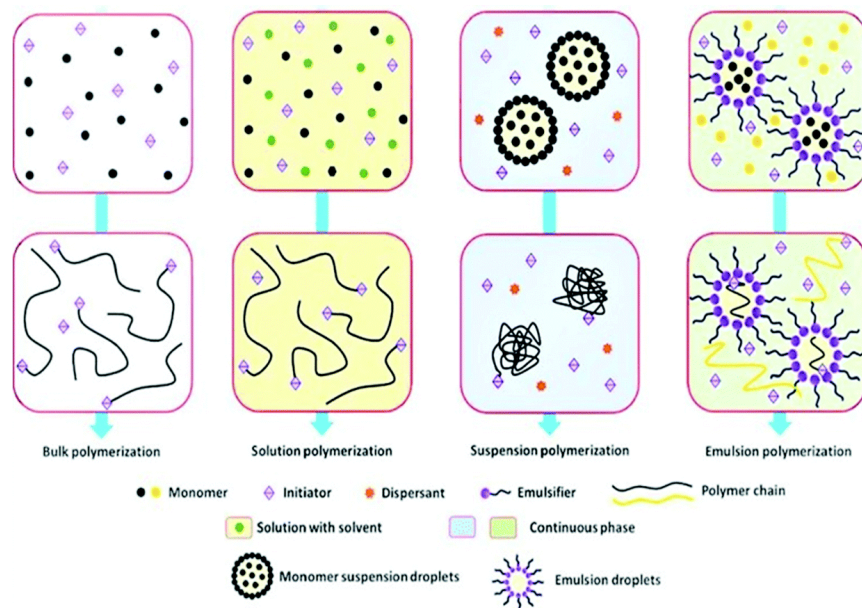
Figure 1.2: Polymerization technique schematic [2]

- **Bulk Polymerization.** It is a simple and homogeneous reaction system used to obtain the polymer. The reaction of polymerization is initiated by heating

3

monomer or exposing it to a light source. When the ingredients in the solution is further polymerized, the viscosity of the final product increases and mixing operation becomes a very difficult process. The product obtained from this polymerization type is called the pure polymer.

The advantages of bulk polymerization:

- It is simple technique.
- The final product is pure.
- It will be used for large casting directly.
- The distribution of molecular weight can be changed with the help of a chain transfer agent.

The disadvantages of bulk polymerization:

- The broad molecular weight distribution in the polymer product is obtained.
- The diffusion of a growing polymer chain is limited.
- The termination gets difficult due to the less amount of collisions.
- The uncontrolled exothermic reaction due to the increase of the rate of polymerization and active radical accumulation lead to eruption.

- **Solution Polymerization.** The monomer polymerizes in a suitable inert solvent with the chain transfer agents. Unlike the solvent medium, the free radical initiator can be suspended or dissolved for an ionic and coordination catalyst.

  The advantages of the solution polymerization:

  - It enables to temperature control thanks to facilitating heat transfer of polymerization.
  - The removal of polymer from the reactor is easily done by solvent.
  - It enables to easy stirring by decrasing viscosity of mixture.

  The disadvantages of the solution polymerization:
  -It is very challenging to obtain products with the high molecular weight.

-The complete solvent removal and isolation from the solution by evaporation and precipitation is extremely difficult.

- **Suspension Polymerization.** Unlike the bulk polymerization, suspension polymerization controls the enormous amount of heat release. Only water insoluble monomers are suitable for this technique. The suspended monomer is in the form of fine droplets in water and surface active agents. These are fixed and prevented from combining with suitable water soluble protective colloids. Agitators are employed in the aqueous phase to maintain a droplet size and dispersion. Heat is transferred between the droplets and water, which has huge amount of heat capacity and low viscous property. Isolation of the materials is easy.

  The advantages of suspension polymerization:

  - It is cheaper method due to involving only water.
  - The change in the viscosity is minor so it is unimportant.
  - Similar to solution polymerization, temperature control is easy for this technique.
  - The final product can be separated and purified.

  The drawbacks of suspension polymerization:

  - It cannot be used for polymers whose polymerization temperature is greater than glass transition temperature.
  - Agitation sensitivity is very high.
  - It is difficult to determine polymer size.

- **Emulsion Polymerization.** The monomer is spread in an aqueous phase as fine droplets which are then emulsified by surface active agents, protective colloids and also by certain buffers in emulsion polymerization. The initiators should be water soluble. The surfactants are used in order to reduce the surface tension at interface between monomer and water and facilitate emulsification of the monomer. When the monomer is added to system and provoked, emulsification starts. Emulsion systems use a water soluble initiators such as persulfate or hydrogen peroxide. It is the most widely used industrial technique.

The advantages of emulsion polymerization:

- It creates high molecular weight polymers.
- It has very fast polymerization rate.
- The heat is easily removed from system.

The shortcomings of emulsion polymerization:

- Additional cleanup and purification may be required for polymer.
- It is difficult to remove entrenched coagulants, emulsifiers, surfactants.

1.3 Literature Review

Although frontal polymerization is an active area of research in the self-autonomous material literature, the pioneering studies on frontal polymerization can be traced back to 1970s. Frontal polymerization was first discovered in Russia by Chechilo and Enikolopyan from the Institute of Chemical Physics and the Branch of the Institute of Chemical Physics of the Soviet Union Academy of Sciences in 1972, see [8]. They have studied the frontal polymerization of poly methyl methacrylate (PMMA) to determine the effect of initiator type than with traditional homogeneous methods and the concentration of initiator on front velocity because the rapid motion of front prevented sedimentation of pressure. The scientific fundamentals were researched for the technological development of the implementation of continuous frontal polymerization on the foundation basis of accumulated experience, see Davtyan et al. [9]. The most beneficial factor of frontal polymerization is that continuous reactors in laminar and particularly turbulent flows are used to complete the process from the implementation point of view. After 1991, Prof. J. Pojman of Mississippi State University, USA participated in the research and the first work was published by J.Pojman in 1991 [10]. Undoubtedly, frontal polymerization is currently a highly active area of research for many researchers due to Pojman's extensive efforts.

Sottos and coworkers claim that the properties of the frontal ring-opening meathesis polymerization (FROMP) of dicyclopentadiene (DCPD) are comparable to conventionally manufactured polymer, and energy savings of these materials are up to ten

orders of magnitude, see Dean et al. [4]. On the other hand, the mechanical properties of the rapidly manufactured robust elastomers using frontal polymerization could not achieve the sufficient capacity for being used as commercial rubbers. However, Dean et al. [4] have put forward a novel method, which is based on the co-polymerization of 1,5-cyclooctadiene (COD) with a norbornene derivative, to terminate crystallization and achieve a polymer that has a wider range of thermomechanical properties. They have worked on the FROMP of comonomer mixtures of COD and DCPD. Furthermore, the DCPD monomer with two reactive sites has enabled the formation of chemical cross-links. They have used the swelling tests and dynamic mechanical analysis (DMA) to observe that DCPD fraction increased by the degree of cross-linking in copolymers produced by FROMP.

According to another viewpoint, the complexity of the dynamic control of frontal polymerization causes it to be inefficiently utilized on the manufacturing side despite of its efficiency and reduced environmental effect.Geubelle and coworkers, see Gao et al. [11], immersed the phase-changing poly-caprolactone particles into DCPD resin. Thus, they clarify the control and patterning of the front propagation in a DCPD resin. Predictive and designed patterning shows that the velocity, temperature, and propagation path of the polymerization front between two different interaction regimes are governed by the exothermic chemical reaction, the interplay between endothermic phase transition, and heat exchange. The manufacturing methodology that is based on frontal polymerization and characterized by the self-propagating exothermic polymerization provides a rapid, environmentally friendly, and energy-saving alternative to the conventional autoclave-based curing techniques involving elevated temperatures and complex pressure cycles that are both energy- and time-consuming. As opposed to the latter, frontal polymerization has been utilized in the one-step fabrication of homogeneous polymeric parts where no secondary procedures such as deposition, etching, layer-by-layer assembly, or the introduction of a second phase is needed until now. The polymerization front controlled dynamically affects the patterns and properties of the polymeric product obtained by one-step manufacturing of parts. For instance, the mechanical, chemical, morphological, and chemical patterns in the polymer are greatly affected by the sharp variation in the frontal temperature spontaneously.

7

The other important issue regarding the manufacturing through frontal polymerization is the propagation of polymerization front, see Goli et al. [3]. The front of polymerization spreads in a steady-state fashion in most production cases. However, the instabilities of front affect the qualification of the composite under different conditions. Geubelle and coworkers [3] have developed a coupled thermo-chemical model and an adaptive nonlinear finite element solver to simulate the instabilities driven by frontal polymerization in dicyclopentadiene (DCPD) and in carbon-fiber DCPD-matrix composites computationally. They have investigated the effect of initial temperature and the carbon fiber volume fraction on the wavelength and amplitude of the thermal instabilities with the help of one-dimensional transient computations. The effect of convective heat loss on the frontal polymerization-driven instabilities in both neat resin and composite cases has been also emphasized in this precise study.

The influence of the chemical and physical properties of the resin on the evolution of frontal polymerization has also been investigated by Frulloni et al. [12]. In classical bulk polymerization, heat is uniformly distributed during the course of an entire curing process on the whole surface of the reactive monomers. Hence, it promotes their reaction. In frontal polymerization, however, the local increase in temperature for a short time interval triggers the polymerization of the monomers (or reactants). The reaction front propagates in the rest of monomers through the heat released by the curing process where the generated heat is dissipated eventually to surroundings. The degree of curing of a final product produced by frontal polymerization is relatively high.While the reaction is controlled by the reactor temperature during bulk polymerization, the chemical and physical properties of the reacting system (front) govern the reaction process in frontal polymerization.

In spite of various advantages of frontal polymerization compared to bulk polymerization, there are some drawbacks that need to be addressed, see Goldfeder and Volpert [6]. One of the downsides is that the conversion tends to be incomplete. Thus, the greater amounts of initiator should be used in order to overcome this issue that in turn leads to a large number of undesirably short polymer chains. Another potential problem is concerned with the heat loss and the extinction limit. The excessive heat losses beyond a certain critical value may cease the propagation of the front.

8

It has been shown by Davtyan et al. [9] that the heat loss during frontal polymerization could considerably affect the properties of the final polymeric material. In particular, the temperature measurements conducted using the thermo-couples installed in the central and peripheral regions of the solidifying samples indicate uneven distribution of temperature throughout the sample. Since the polymerization is a thermally activated process, the non-uniform distribution of temperature may result in heterogeneities in the properties of the product such as the molecular weight characteristics, the residual stress level, and the monolithic structure of the resulting polymer materials. Therefore, the effect of the factors such as heat loss and the cooling of reaction ampoules after polymerization at arbitrary rates on the properties of polymer materials produced by frontal polymerization have to be taken into account carefully.

Up to this point, the studies on the chemical, thermomechanical, and front propagation characteristics of frontal polymerization have been reviewed. Since there is no study on the mechanics of frontally polymerized polymers, we will review several studies that are concerned with the development of phenomenological constitutive models to simulate the thermal and cure-dependent deformations in polymer composites manufactured through conventional methods.

A remarkable study in this direction has been conducted by Höfer and Lion [13]. They have developed a finite thermo-viscoelastic model to represent an exothermal phase transformation from a viscous fluid to a viscoelastic solid. The deformation gradient has been multiplicatively decomposed into the thermal, chemical, and mechanical parts. The concept of intrinsic time [14] has been used to account for the viscous rate-dependency. The evolution of the viscoelastic properties of the material has been considered to be governed by the degree of curing. The model accounts for the phase transformation through the volume fraction changes.

Since monomer behaves as a deformable viscous liquid, it is only capable of sustaining hydrostatic load in practice. When the curing reactions continue, polymer chains are also connected to each other through cross-links. The viscosity of the liquid resin and its molecular weight increase as time evolves. The heat generated due to the formation of the polymer network results in a temperature increase since the cross-linking is an exothermal reaction. This causes some initial viscosity decrease,

see Hossain et al. [15]. The temperature- and shrinkage-induced deformations may give rise to the accumulations of stresses and strains or warping phenomena significantly. It is claimed that the warpage due to the curing-induced residual stresses has long been a major obstacle for reducing the cost of the manufacture of composites. Hossain et al. [15] developed a phenomenological model in order to represent the curing behaviour of thermosets within the geometrically linear setting where they have investigated the temporal evolution of shear modulus and relaxation time.

Steinman and coworkers [16] have extended their previous study to the finite strain regime. The main assumption of this study is that the existing chains between cross-links are deformed when the strain is applied. When the new cross-links are created, these are integrated to already deformed structure and they are never affected by previous deformation. This means that they meet the expectation for the incremental formulation. However, their approach holds only for materials in the state beyond being gel. They have been also interested in the temporal evolution of material properties simultaneously. In the follow-up work, they have taken their studies one step further by adding the intrinsic time approach of Höfer and Lion [17] in the viscoleastic model and focused on shrinkage effects [18].

Recently, Rajagopal and coworkers [19] have proposed a thermodynamic framework based on their previous work [20] of rubber within the framework of finite viscoelasticity involving the constitutive modeling of vulcanization chemical reactions. They have also used fused deposition modeling for the amorphous polymers. They have made predictions for the residual stresses and the accompanying distortion of the geometry of the printed part. They used the four ribbons of polymeric melt stacked on top of each other by extruding through a flat nozzle to show the usefulness and efficacy of the constitutive model. Similarly, Sain and coworkers [21] have also been interested in the residual stress and warpage in the glassy polymers. They proposed a model which is thermodynamically consistent, frame-indifferent, chemo–thermo–mechanical coupled constitutive framework for cured glassy polymers. The residual stresses due to the volume shrinkage accompanied by curing cause the cracks, interfacial delamination and warpage. It has been shown that the careful selection of processing parameters is of vital importance in order to decrease warpage and failure dramatically. The heat generated due to the curing can cause

10

uneven curing of the component, so a constitutive model which describes the coupled chemo–thermo-mechanical process is essential.

N'Guyen and coworkers [22] have contributed the literature by adding two points that are concerned with the new form of the chemical potential energy and the chemical evolution associated to this potential. They have developed a model for the thermo-chemo-mechanical behavior of polymer at large strains. Although material processing and curing may involve completely different phenomena, they require a rigorous thermodynamical framework. They have also used the thermal, chemical, and mechanical decomposition of the deformation gradient.

Another eye-opening study has been conducted by Saito and workers [23]. They have obtained the degree of curing dependent macroscopic viscoelastic properties, the macroscopic coefficients of thermal expansion (CTE), and the coefficient of cure shrinkage (CCS) from the relaxation curves obtained by the numerical material test (NMT) results and have also assumed that the orthotropic version of the model can be used to simulate the macroscopic mechanical behavior of fiber-reinforced plastics (FRP) for the resin. They have contributed to the literature by introducing a new configuration of the rheology elements. They also formulate the macroscopic CTE and CCS in the generalized Maxwell model for both equilibrium and non-equilibrium parts. In other words, they have proposed a viscoelastic analysis method of two-scale decoupling of unidirectional FRP subjected to the curing. To do so, they formulated continuum level constitutive functions whose material parameters depend on both the degree of curing and ambient temperature.

Yamanaka and coworkers [24] have had a different perspective with a different formulation. They have developed an incremental variational formulation for the thermo-mechanical coupled problem of curing resin. The dual dissipation potential is combined with viscoelasticity for the cure state. Thanks to the incremental variational formulation, they optimize the change of energy concerning an internal variable to obtain the instantaneous total equilibrium states of an inelastic continuum body. They have also discussed the existence and uniqueness of solutions and computational efficiency while strictly maintaining present formulation. They claim that this study is the first model proposed for thermo-mechanical analysis of thermosetting polymers.

However, finite strain and shrinkage effects have not been taken into account.

1.4 Contributions and Novelties

As outlined above, the experimental and computational studies on frontal polymerization have focused only on the chemical, thermo-mechanical, and the front velocity properties of the frontal polymerization so far. To this end, in this contribution, we develop novel constitutive models furnished with robust computational tools to describe the process of frontal polymerization and the behavior of polymeric materials produced by frontal polymerization. In particular,

- the incremental models of finite elasticity coupled with the inherent thermal and chemical aspects for the frontally polymerized materials are developed,

- the coupled chemo-thermo-mechanical constitutive models are constructed in a new thermodynamically consistent framework,

- the continuous evolution of material properties (aging) is accounted for in the incremental setting,

- the robust computational tools furnished with stable and efficient algorithms are developed to incorporate chemothermal, thermomechanical, and chemomechanical couplings,

- the developed multi-field coupled model is used to conduct numerical analysis to predict the accumulation of stresses due to the chemically induced shrinkage and thermal volume changes. Undoubtedly, the far-reaching goal of the developed computational models is the optimum design of frontal polymerization manufacturing technique to towards mechanically stronger and tougher polymer products and composites that have a broad spectrum of high-tech applications.

1.5 Outline of Thesis

This thesis is organized as follows:

In Chapter 2, the fundamental equations of the coupled boundary-value problem of chemo-thermo-mechanics for frontal polymerization are derived using the tools of continuum thermomechanics.

In Chapter 3, the kinematic and constitutive equations of the chemo-thermo-mechanical model are specified.

Chapter 4 is devoted to the finite element formulation of the coupled problem. The expressions of the residual vectors and the associated tangent matrices are derived consistently with the employed staggered solution strategy.

The representative numerical examples addressing chemo-thermo-mechanical couplings in frontal polymerization are presented in Chapter 5. In particular, these examples are designed to illustrate the effects of different types of material behavior, various boundary conditions on the evolution of the stress accumulations during the course of frontal polymerization.

In Chapter 6, the concluding remarks and outlook are given.

THERMODYNAMICAL FRAMEWORK

In this chapter, we introduce the fundamental equations of the chemo-thermo-mechanical coupled boundary-value problem to set the thermodynamical framework for the frontally polymerized thermoset materials at finite strains. A similar study was done by N'Guyen and his coworkers [22], but in our study, we will discuss the framework for materials produced with a different polymerization method (frontal polymerization). Thus, we describe the principal equations of the fundamental maps, the fundamental balance equations of solid body, and the stress measures. For more detailed description the reader is referred to studies [25, 26, 27, 28, 29].

2.1   The Motion, Fundamental Geometric Maps and Deformation Measures

A solid body B is composed of infinitely many material points $P \in B$ which also indicate positions in the Eucledian space $\mathbb{R}^3$. The geometry of the body B in $\mathbb{R}^3$ in (2.1) at time t is expressed by a bijective nonlinear deformation map as shown in Figure 2.1 and described mathematically in (2.1).

$$\boldsymbol{\mathcal{X}}_t := \begin{cases} B \rightarrow \mathcal{B}_t \in \mathbb{R}^3 \\ P \in B \mapsto \boldsymbol{x}_t = \boldsymbol{\mathcal{X}}_t(P) \in \mathcal{B}_t, \end{cases} \tag{2.1}$$
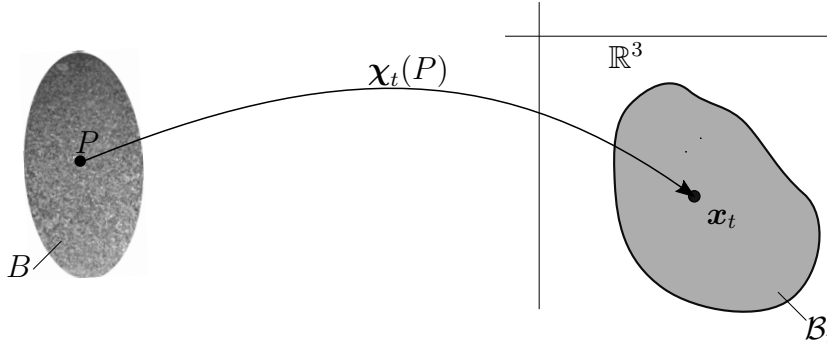
Figure 2.1: The map from the material space to the Euclidean space

The motion of a body can then be considered as a group of location parameterized by time. Thus, in a motion, the particle P occupies a sequence of places $\boldsymbol{x}_t$ in space. The position of the material points at t_0 $\boldsymbol{X} = \boldsymbol{\chi}_{to}(P) \in \mathcal{B}$ is named as the **Reference Configuration** that is generally assumed to be an undeformed state. Likewise, the **Spatial / Eulerian Configuration** of the body at time t is indicated by $\boldsymbol{x} = \boldsymbol{\chi}_t(P) \in \mathcal{S}$ as shown in Figure 2.2:
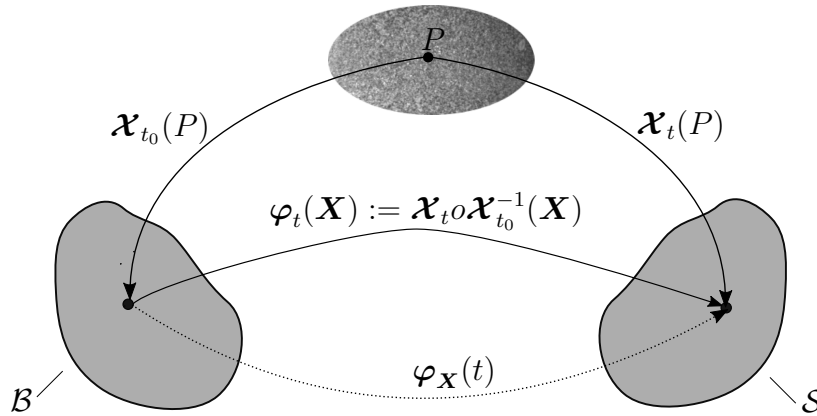
Figure 2.2: The nonlinear deformation map $\boldsymbol{\varphi}(\boldsymbol{X})$ from the referential configuration to the spatial configuration

In this manner, the deformation map $\boldsymbol{\varphi}_t(\boldsymbol{X})$ can be defined between $\boldsymbol{\chi}_{t0}(P)$ and $\boldsymbol{\chi}_t(P)$ to illustrate the motion of the body in the Euclidean space with the one-to-one relation in (2.2).

$$\boldsymbol{\varphi}_t := \begin{cases} \mathcal{B} \to & \mathcal{S} \\ \boldsymbol{X} \mapsto & \boldsymbol{x} = \boldsymbol{\varphi}_t(\boldsymbol{X}) \end{cases} \tag{2.2}$$

It is also possible to find the position of Euclidean point in the reference configuration

thanks to bijectivity of deformation map. The inverse deformation map is represented in (2.3).

$$\varphi_t^{-1} := \begin{cases} \mathcal{S} \to & \mathcal{B} \\ \boldsymbol{x} \mapsto & \boldsymbol{X} = \varphi_t^{-1}(\boldsymbol{x}) \end{cases} \tag{2.3}$$

The differential geometry of material and spatial curves on the geometry of the body as depicted in Figure 2.3 is described by tangent vectors. Beside, $\boldsymbol{\chi}_0(\Theta)$ and $\boldsymbol{\chi}_t(\Theta)$ which are material and spatial curves respectively are parameterized by variable $\Theta \in \mathbb{R}$ as shown in Figure 2.3.
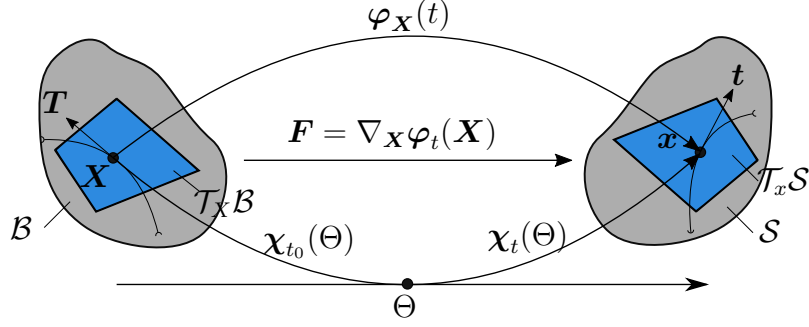
Figure 2.3: The mapping between the material space and the Euclidean space

The tangent vector is a useful tool for the calculation of the stretch, and the deformation gradient so the referential and spatial tangent vectors are calculated in (2.4), respectively.

$$\boldsymbol{T} := \frac{d(\boldsymbol{\chi}_{t_0}(\Theta))}{d\Theta} \in \mathcal{T}_{\boldsymbol{X}}\mathcal{B} \quad \text{and} \quad \boldsymbol{t} := \frac{d(\boldsymbol{\chi}_t(\Theta))}{d\Theta} \in \mathcal{T}_{\boldsymbol{x}}\mathcal{S} \tag{2.4}$$

We use the chain rule operation in the tangent vector calculation for the spatial curves, and we found the relation in (2.5).

$$\boldsymbol{t} = \frac{d(\boldsymbol{\chi}_t(\Theta))}{d\Theta} = \nabla_{\boldsymbol{X}}\varphi_t(\boldsymbol{X})\frac{d(\boldsymbol{\chi}_{t_o}(\Theta))}{d\Theta} \tag{2.5}$$

It is obvious that the deformation gradient $\boldsymbol{F}$ is none other than the first term in the right hand side of (2.5).

$$\boldsymbol{F} = \nabla_X\varphi_t(\boldsymbol{X}) \quad \text{and} \quad \boldsymbol{T} = \frac{d\boldsymbol{\chi}_{t_o}(\Theta)}{d\Theta} \tag{2.6}$$

According to the result in (2.5), we can write the relation between the referential and spatial tangent vectors as shown in (2.7).

$$\boldsymbol{t} = \boldsymbol{FT} \tag{2.7}$$

17

Then, the map of the referential tangent vectors to the spatial counter parts described by the tensor called the deformation gradient ($\boldsymbol{F}$) is expressed mathematically in (2.8).

$$\boldsymbol{F}(\boldsymbol{X},t) := \begin{cases} \mathcal{T}_{\boldsymbol{X}}\mathcal{B} & \to \mathcal{T}_{\boldsymbol{x}}\mathcal{S}, \\ \boldsymbol{T} & \mapsto \boldsymbol{t} = \boldsymbol{F}\boldsymbol{T} \end{cases} \tag{2.8}$$

Each spatial tangent vector $d\boldsymbol{x}$ is identified as the tangent map of its material counterpart as described in (2.9).

$$d\boldsymbol{x} = \boldsymbol{F}d\boldsymbol{X} \tag{2.9}$$

Then, we define the Jacobi map through the conventional coordinate free definition of the determinant of a second-order tensor of the deformation gradient. The volume map J is restricted to positive numbers $\mathbb{R}_+$ to ensure the function bijectivity. We use dV and dv to describe the infinitesimal volume elements of parallelepipeds as given in (2.10) and (2.11).

The volume in material space is introduced as shown in (2.10) and depicted in Figure 2.4:

$$dV := d\boldsymbol{X}_3 \cdot (d\boldsymbol{X}_2 \times d\boldsymbol{X}_1) \tag{2.10}$$

The spatial counterpart of (2.10) is described in (2.11) and shown in Figure 2.4:

$$dv := d\boldsymbol{x}_3 \cdot (d\boldsymbol{x}_2 \times d\boldsymbol{x}_1) \tag{2.11}$$

where $d\boldsymbol{x}_i = \boldsymbol{F}d\boldsymbol{X}_i$ for $i = 1,2,3$.

If we put the relation in (2.9) into (2.11), we observe that $\det(\boldsymbol{F})$ is the map of the volume in spatial space to the material counterpart as specified in (2.12).

$$\begin{aligned} dv &= (\boldsymbol{F}d\boldsymbol{X}_3) \cdot (\boldsymbol{F}d\boldsymbol{X}_2 \times \boldsymbol{F}d\boldsymbol{X}_1) \\ &= \det(\boldsymbol{F}) \ d\boldsymbol{X}_3 \cdot (d\boldsymbol{X}_1 \times d\boldsymbol{X}_2) \end{aligned} \tag{2.12}$$

When we compare (2.12) with (2.11), we obtained the Jacobi mapping J in (2.13) which is one-to-one relation and restricted to positive real numbers to satisfy the impenetrability of matter.

$$dv = JdV \tag{2.13}$$

18
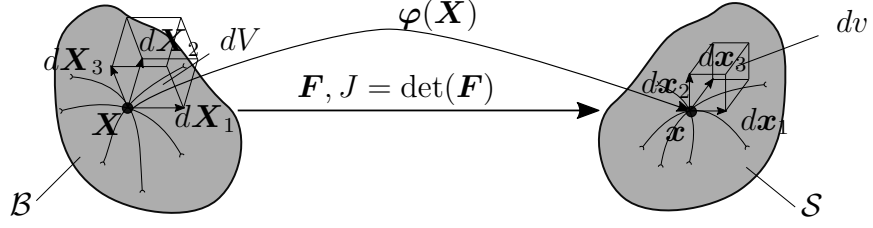
Figure 2.4: The volume (Jacobian) map

The other transformation is area map that transformed the normals of material surfaces onto the normals of spatial surfaces which is depicted in Figure 2.5. To make it clear, the reference and spatial areas have to be calculated as the cross product of two non-colinear tangent vectors as defined in (2.14).
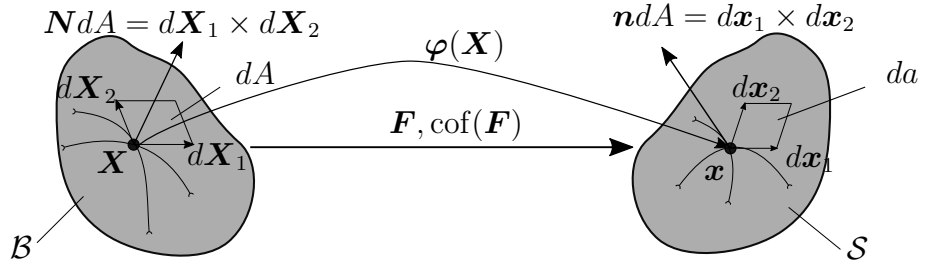
Figure 2.5: The illustration regarding the mapping between normal spaces

$$\boldsymbol{N}dA = d\boldsymbol{X}_1 \times d\boldsymbol{X}_2$$
$$\boldsymbol{n}da = d\boldsymbol{x}_1 \times d\boldsymbol{x}_2$$

(2.14)

When we consider the relation $d\boldsymbol{x}_i = \boldsymbol{F}d\boldsymbol{X}_i$ for $i = 1,2,3$ in (2.9) and using the Jacobi map (2.13), we arrive at,

$$d\boldsymbol{x}_3 \cdot \boldsymbol{n}da = Jd\boldsymbol{X}_3 \cdot \boldsymbol{N}dA$$

(2.15)

Then, we solve (2.15) for $\boldsymbol{n}da$ for an arbitrary tangent vector $\mathrm{d}\boldsymbol{X}$, the co-factor of the deformation gradient comes out as in (2.16).

$$\boldsymbol{n}da = \mathrm{cof}(\boldsymbol{F})\boldsymbol{N}dA \quad \text{where} \quad \mathrm{cof}(\boldsymbol{F}) := J\boldsymbol{F}^{-T}$$

(2.16)

The tensorial quantity carrying out the map in (2.17) is $\boldsymbol{F}^{-T}$, so $\boldsymbol{F}^{-T}$ should be considered as the normal map transforming the reference normals $\boldsymbol{N}$ onto the spatial

19

normals $\boldsymbol{n}$ belonging to the respective co-tangent (normal) spaces $\mathcal{T}_X^*\mathcal{B}$ and $\mathcal{T}_x^*\mathcal{S}$ as depicted in Figure 2.6.

$$\boldsymbol{F}^{-T} := \begin{cases} \mathcal{T}_{\boldsymbol{X}}^*\mathcal{B} \to \mathcal{T}_{\boldsymbol{x}}^*\mathcal{S} \\ \boldsymbol{N} \mapsto \boldsymbol{n} = \boldsymbol{F}^{-T}\boldsymbol{N} \end{cases} \tag{2.17}$$
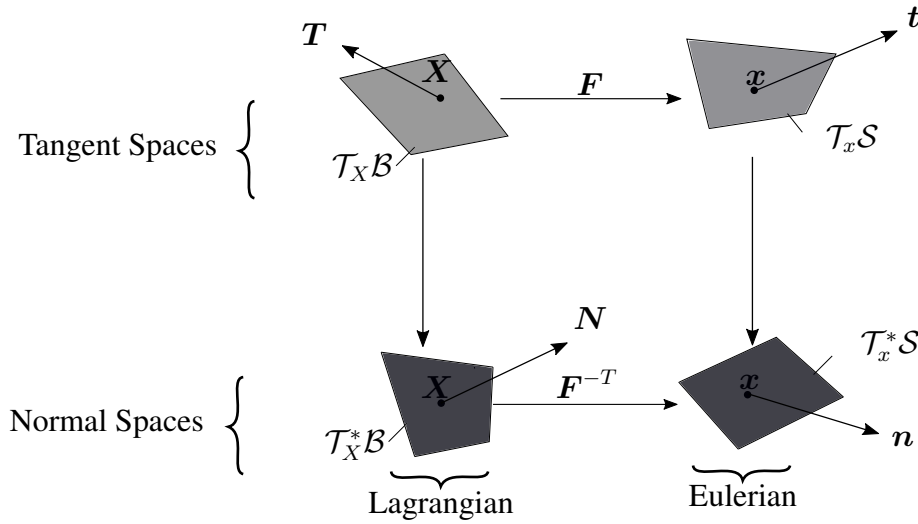
Figure 2.6: The map of the material normal to the spatial normal in the commutative diagram

At this point, we have to introduce the right and left Cauchy-Green tensors. Thus, first of all, the reference $\mathcal{B}$ and spatial $\mathcal{S}$ configurations of a body are locally furnished by coordinate systems in the neighborhood of the reference coordinates $X_{A=1,2,3}$ and the spatial coordinates $x_{a=1,2,3}$. These coordinates systems are generally non-orthogonal but equipped with the reference $\boldsymbol{G} = G_{AB}$ and spatial $\boldsymbol{g} = g_{ab}$ metrics, respectively. The both metric tensors reduce to Kronecker's delta (δ_{ij}) $\boldsymbol{G} = \delta_{AB}$ and $\boldsymbol{g} = \delta_{ab}$ in the case of Cartesian coordinate systems.

To make the geometric meaning of the right and left Cauchy-Green tensors more transparent, it is neccessary to utilize these metric tensors as the mappings from the tangent spaces to the normal spaces of the Lagrangian and Eulerian configurations as defined in (2.18).

$$\boldsymbol{G} : T_{\boldsymbol{X}}\mathcal{B} \longrightarrow T_{\boldsymbol{X}}^*\mathcal{B}$$
$$\boldsymbol{g} : T_{\boldsymbol{x}}\mathcal{S} \longrightarrow T_{\boldsymbol{x}}^*\mathcal{S} \tag{2.18}$$

20

The right and left Cauchy-Green tensors are introduced as shown in (2.19):

$$
\begin{aligned}
\boldsymbol{C} := \boldsymbol{\varphi}^*(\boldsymbol{g}) \qquad &= \boldsymbol{F}^T \boldsymbol{g} \boldsymbol{F} \quad \text{with} \quad C_{AB} = F_{aA} g_{ab} F_{bB} \\
\boldsymbol{b} := \boldsymbol{\varphi}_*(\boldsymbol{G}^{-1}) \quad &= \boldsymbol{F} \boldsymbol{G}^{-1} \boldsymbol{F}^T \quad \text{with} \quad b_{ab} = F_{aA} G_{AB}^{-1} F_{bB}
\end{aligned}
\tag{2.19}
$$

The pull-back operation is defined as $\boldsymbol{C} := \boldsymbol{\varphi}^*(\boldsymbol{g})$ and is represented in the commutative diagram in Figure 2.7:
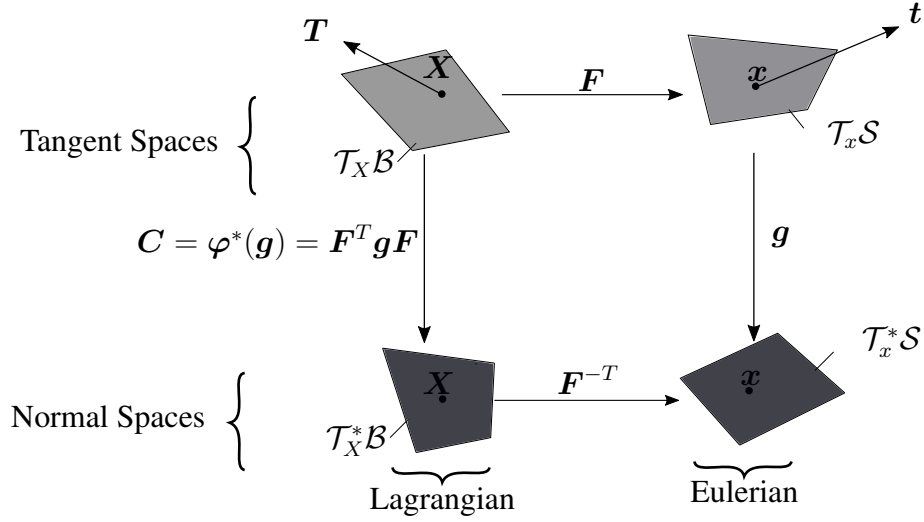
Figure 2.7: The right Cauchy-green tensor and pull-back operation diagram

The push-forward operation is described by $\boldsymbol{b}^{-1} := \boldsymbol{\varphi}_*(\boldsymbol{G})$ and is demonstrated commutative diagram as shown in Figure 2.8:
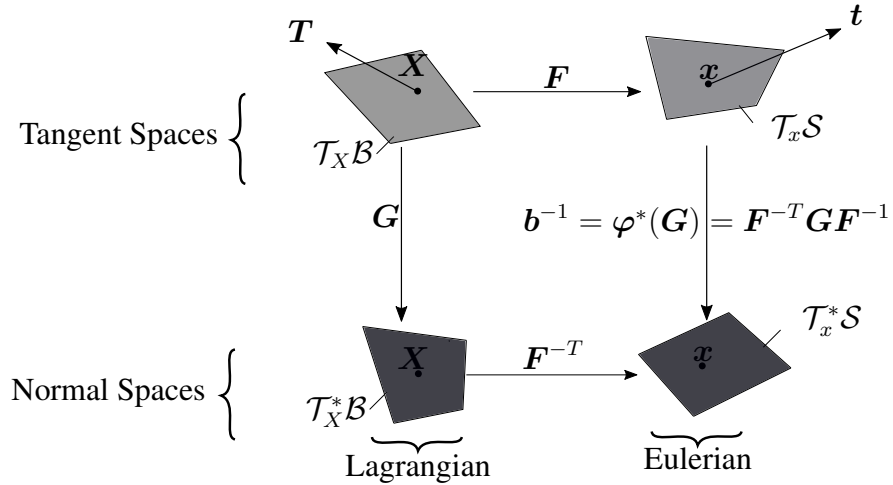
Figure 2.8: The inverse left Cauchy-Green tensor and push-forward operation diagram

Cauchy's Theorem : The theorem states that $\boldsymbol{\sigma}(\boldsymbol{x}, t)$ is a unique second-order tensor to satisfy (2.20).

$$\boldsymbol{t}(\boldsymbol{x}, t, \boldsymbol{n}) = \boldsymbol{\sigma}(\boldsymbol{x}, t)\boldsymbol{n} \quad \text{with} \quad t_a = \sigma_{ab} n_b \tag{2.20}$$

where $\boldsymbol{\sigma}$ is the Cauchy stress tensor which is a symmetric spatial tensor field. The relation in (2.20) is the transformation between the traction vector $\boldsymbol{t}$ and $\boldsymbol{\sigma}$. The prompt result of (2.20) is

$$\boldsymbol{t}(\boldsymbol{x}, t, \boldsymbol{n}) = -\boldsymbol{t}(\boldsymbol{x}, t, -\boldsymbol{n}) \tag{2.21}$$

The relation in (2.21) is none other than the Newton's third law of action and reaction. The Cauchy stress can be shown as a mapping of the normal vector $\boldsymbol{n} \in \mathcal{T}^*\mathcal{S}$ onto the tangent vector $\boldsymbol{t} \in \mathcal{T}^*\mathcal{S}$ as described in (2.22).

$$\boldsymbol{\sigma}(\boldsymbol{x}, t) := \begin{cases} \mathcal{T}_{\boldsymbol{x}}^*\mathcal{S} \to \mathcal{T}_{\boldsymbol{x}}\mathcal{S} \\ \boldsymbol{n} \mapsto \boldsymbol{t} = \boldsymbol{\sigma}\boldsymbol{n} \end{cases} \tag{2.22}$$

2.2 Balance Equations

2.2.1 Balance of Mass

In a closed system, we assume that mass cannot be produced or destroyed: similarly, N'Guyen and coworkers [22] assumed that neither mass creation nor destruction of mass is accepted. Thus, the mass M of a body is a conserved quantity.
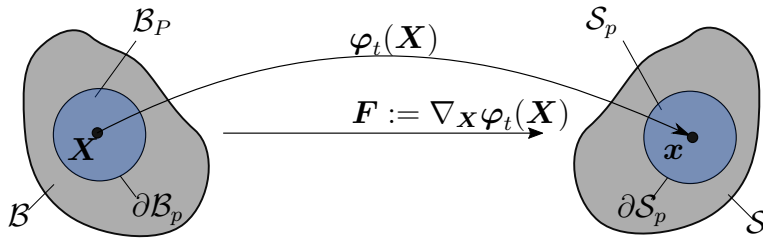
Figure 2.9: The cut out parts $\mathcal{B}_p \subset \mathcal{B}$ and $\mathcal{S}_p \subset \mathcal{S}$ in Lagrangian and Eulerian configuration, respectively

We define the mass of cut out $\mathcal{S}_p \in \mathcal{S}$ in (2.23). The both cut out parts are depicted in

Figure 2.9.

$$M_{\mathcal{S}_p} = \int_{\mathcal{S}_p} \rho(\boldsymbol{x}, t)\, dv = \int dm > 0 \tag{2.23}$$

where $\rho(\boldsymbol{x}, t)$ is the spatial mass density (continuous scalar field).

Since the mass is conserved:

$$\frac{d}{dt}(M_{\mathcal{S}_p}) = 0 \longrightarrow \frac{d}{dt}(dm) = \frac{d}{dt}(\rho dv) = 0 \tag{2.24}$$

The balance of mass requires that the mass of the cut out $\mathcal{B}_p$ is the same as that of $\mathcal{S}_p$. In other words, it is obvious that $M_{\mathcal{S}_p}$ is equal to $M_{\mathcal{B}_p}$.

where

$$M_{\mathcal{B}_p} = \int_{\mathcal{B}_p} \rho_0(\boldsymbol{X}, t)\, dV > 0 \tag{2.25}$$

Therefore, we have

$$\int_{\mathcal{S}_p} \rho(\boldsymbol{x}, t)\, dv = \int_{\mathcal{B}_p} \rho_0(\boldsymbol{X}, t)\, dV \tag{2.26}$$

Then, we obtain in (2.27) which is valid for any cut out part of $\mathcal{B}_p$ by subtracting the mass in the Eulerian configuration from the Lagrangian counterpart and using a jacobian map of the volume elements $dv = JdV$.

$$\int_{\mathcal{B}_p} (J\rho - \rho_0)\, dV = 0 \tag{2.27}$$

The identity in (2.27) is valid for any section of $\mathcal{B}_p$, we arrive the transformation locally with Jacobi map J in (2.28).

$$\rho_0(\boldsymbol{X}, t) = J(\boldsymbol{X}, t)\rho(\boldsymbol{x}, t) \tag{2.28}$$

Since the reference mass density should not be changed with respect to time in closed systems, so we generalize in (2.24) as shown in (2.29):

$$\frac{d\rho_0(\boldsymbol{X})}{dt} = \dot{\rho}_0(\boldsymbol{X}, t) = 0 \tag{2.29}$$

23

Then, we put (2.29) into (2.24), and the relation in (2.30) is obtained.

$$\frac{dM_{\mathcal{S}_p}}{dt} = \frac{d}{dt}\int_{\mathcal{S}_p} \rho\,dv = \frac{d}{dt}\int_{\mathcal{B}_p} \rho J\,dV = 0 \tag{2.30}$$

Due to time dependency of the domain of integration, we use the time derivation through integrand of the Lagrangian integral. Then, we find

$$\frac{dM_{\mathcal{B}_p}}{dt} = \int_{\mathcal{B}_p} \frac{d(\rho J)}{dt}\,dV = \int_{\mathcal{B}_p} [\dot{\rho}J + \dot{J}\rho]\,dV = 0 \tag{2.31}$$

We arrived the relation in (2.32) as the integral identity of (2.31) holds for any $\mathcal{B}_p$.

$$[\dot{\rho}J + \dot{J}\rho] = 0 \tag{2.32}$$

The result in (2.32) is valid for any $\mathcal{B}_p$. The time derivative of Jacobian can be derived as in (2.33).

$$\begin{aligned}
\dot{J} &= \partial_{\boldsymbol{F}}J : \dot{\boldsymbol{F}} = \operatorname{cof}(\boldsymbol{F}) : \dot{\boldsymbol{F}} \\
&= J\boldsymbol{F}^{-T} : \dot{\boldsymbol{F}} = J\boldsymbol{1} : \underbrace{(\dot{\boldsymbol{F}}\boldsymbol{F}^{-1})}_{\boldsymbol{l}} \\
&= J\operatorname{tr}(\boldsymbol{l}) = J\nabla_{\boldsymbol{x}}(\boldsymbol{v}) : \boldsymbol{1} \\
&= J\operatorname{div}(\boldsymbol{v})
\end{aligned} \tag{2.33}$$

Then, we insert (2.33) into (2.32), and we arrive

$$\dot{\rho} + \rho\operatorname{div}(\boldsymbol{v}) = 0 \tag{2.34}$$

2.2.2 Balance of Linear Momentum

We have two types of forces which are the body forces (mass specific) $\boldsymbol{\gamma}(\boldsymbol{x}, t)$ due to the action of other bodies at a distance and the surface forces (traction vectors) $\boldsymbol{t}$ due to the action at a vicinity. The balance of linear momentum states that the time rate of change of linear momentum $\mathcal{L}_{\mathcal{B}_p}$ of $\mathcal{B}_p \in \mathcal{B}$ is equal to the sum of the these forces $\mathcal{F}_{\mathcal{B}_p}$. We arrange this phenomena for the referential and spatial space as shown in Figure 2.10.

The linear momentum can be described mathematically in (2.35).

$$\mathcal{L}_{\mathcal{S}_p} := \int_{\mathcal{S}_p} \boldsymbol{v}\,dm = \int_{\mathcal{S}_p} \rho\boldsymbol{v}\,dv \tag{2.35}$$
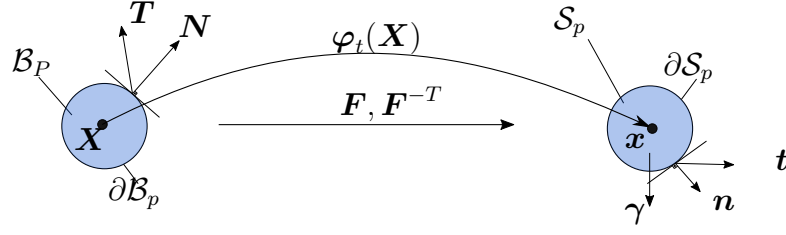
Figure 2.10: Surface and body forces acting on cut out parts $\mathcal{B}_p$ and $\mathcal{S}_p$

The forces acting on body mentioned above are given in (2.36).

$$\mathcal{F}_{S_p} = \underbrace{\int_{\partial \mathcal{S}_p} \boldsymbol{t}\, da}_{\text{traction forces}} + \underbrace{\int_{\mathcal{S}_p} \boldsymbol{\gamma}\, dm}_{\text{body forces}} \tag{2.36}$$

To make it clearer, the change of linear momentum with per unit time is equal to total forces which are mass-specific body forces and traction forces which is described in (2.37) as mathematically.

$$\frac{d}{dt}(\mathcal{L}_{S_p}) = \mathcal{F}_{S_p} \tag{2.37}$$

If we put (2.35) and (2.36) into (2.37), we arrive at

$$\frac{d}{dt}\int_{\mathcal{S}_p} \rho \boldsymbol{v}\, dV = \int_{\mathcal{S}_p} \rho \boldsymbol{\gamma}\, dv + \int_{\partial \mathcal{S}_p} \boldsymbol{t}\, da \tag{2.38}$$

Then, we focus on the left hand side of (2.39), and take a time derivative.

$$\frac{d}{dt}\int_{\mathcal{S}_p} \rho \boldsymbol{v}\, dv = \int_{\mathcal{S}_p} \dot{\boldsymbol{v}}\rho\, dv + \int_{\mathcal{S}_p} \boldsymbol{v}\frac{d}{dt}(\rho\, dv) \tag{2.39}$$

Due to the balance of mass, the last term in the right hand side of the equality in (2.39) should be zero.

$$\int_{d\mathcal{S}_p} \frac{d}{dt}(\rho dv) = 0 \tag{2.40}$$

The other side of the equality in (2.38) can be derived as follows by using Cauchy stress theorem as explained in (2.22):

$$\int_{\partial \mathcal{S}_p} \boldsymbol{t}\, da = \int_{\partial \mathcal{S}_p} \boldsymbol{\sigma}\boldsymbol{n}\, da = \int_{\mathcal{S}_p} \text{div}(\boldsymbol{\sigma})\, dv \tag{2.41}$$

As a result, we can find the most famous conservation of linear momentum expression in (2.42).

$$\int_{\mathcal{S}_p} \rho \dot{\boldsymbol{v}}\, dV = \int_{\mathcal{S}_p} \rho \boldsymbol{\gamma}\, dv + \int_{\mathcal{S}_p} \text{div}(\boldsymbol{\sigma})\, dv \tag{2.42}$$

For the local form of the balance of linear momentum in the Eulerian setting is given in (2.43):

$$\rho \boldsymbol{a} = \rho \boldsymbol{\gamma} + \operatorname{div}(\boldsymbol{\sigma}) \tag{2.43}$$

where $\boldsymbol{a}$ is the acceleration.

2.2.3 Balance of Angular Momentum

The conservation of the angular momentum is defined by equating the rate of moment of momentum to the net moment formed by total forces acting on body. The angular momentum of $\mathcal{S}_p$ is described as

$$\boldsymbol{\mathcal{D}}_{\mathcal{S}_p} := \int_{\mathcal{S}_p} \boldsymbol{x} \times \boldsymbol{v} \, dm = \int_{\mathcal{S}_p} \boldsymbol{x} \times \boldsymbol{v} \rho \, dv \tag{2.44}$$

The resultant moment generated by forces acting on $\mathcal{S}_p$ is derived in (2.45)

$$\boldsymbol{\mathcal{M}}_{\mathcal{S}_p} := \int_{\mathcal{S}_p} \rho \boldsymbol{x} \times \boldsymbol{\gamma} \, dv = \int_{\partial \mathcal{S}_p} \boldsymbol{x} \times \boldsymbol{t} \, da \tag{2.45}$$

$\boldsymbol{\mathcal{D}}_{\mathcal{S}_p}$ and $\boldsymbol{\mathcal{M}}_{\mathcal{S}_p}$ are considered with respect to the fixed origin in the space so this notation is used in (2.44), (2.45). The balance of angular momentum equation can be described as shown in (2.46):

$$\frac{d}{dt}(\boldsymbol{\mathcal{D}}_{\mathcal{S}_p}) = \boldsymbol{\mathcal{M}}_{\mathcal{S}_p} \tag{2.46}$$

The meaning of the mathematical expression in (2.46) is the time change of the angular momentum $\boldsymbol{\mathcal{D}}_{\mathcal{S}_p}$ of $\mathcal{S}_p \in \mathcal{S}$ is identical to the sum of the moment $\boldsymbol{\mathcal{M}}_{\mathcal{S}_p}$ generated by the forces acting on $\mathcal{S}_p$ as in (2.47).

$$\underbrace{\frac{d}{dt} \int_{\mathcal{S}_p} \boldsymbol{x} \times \rho \boldsymbol{v} \, dv}_{T2} = \int_{\mathcal{S}_p} \boldsymbol{x} \times \rho \boldsymbol{\gamma} \, dv + \underbrace{\int_{\partial \mathcal{S}_p} \boldsymbol{x} \times \boldsymbol{t} \, da}_{T1} \tag{2.47}$$

The last term (T1) on the right hand side of the equality in (2.47) can be written as follows:

$$\int_{\partial \mathcal{S}_p} \boldsymbol{x} \times \boldsymbol{t} \, da = \int_{\partial \mathcal{S}_p} \epsilon_{ijk} x_j t_k \, da \overset{\text{Cauchy's theorem}}{=} \int_{\partial \mathcal{S}_p} \epsilon_{ijk} x_j \sigma_{kl} n_l \, da$$

$$\overset{\text{Gauss Theorem}}{=} \int_{\mathcal{S}_p} \frac{\partial(\epsilon_{ijk} x_j \sigma_{kl})}{\partial x_l} \, dv = \int_{\mathcal{S}_p} \left(\epsilon_{ijk} \frac{\partial x_j}{\partial x_l} \sigma_{kl} + \epsilon_{ijk} x_j \frac{\partial \sigma_{kl}}{\partial x_l} \right) dv \tag{2.48}$$

$$= \int_{\mathcal{S}_p} (\epsilon_{ijk} \sigma_{kl}) \, dv + \int_{\mathcal{S}_p} \boldsymbol{x} \times \operatorname{div}(\boldsymbol{\sigma}) \, dv$$

26

The other term (T2) on the left hand side of the equality in (2.47) can be derived as follow:

$$\frac{d}{dt}\int_{\mathcal{S}_p} \boldsymbol{x} \times \rho\boldsymbol{v}\, dv = \underbrace{\int_{\mathcal{S}_p} \boldsymbol{v} \times \rho\boldsymbol{v}\, dv}_{\mathbf{0}} + \int_{\mathcal{S}_p} \boldsymbol{v} \times \rho\boldsymbol{a}\, dv + \underbrace{\int_{\mathcal{S}_p} \boldsymbol{v} \times \rho\boldsymbol{v}\, \frac{d}{dt}(\rho dv)}_{\mathbf{0} \quad \text{due to} \quad (2.29)}$$

$$= \int_{\mathcal{S}_p} (\boldsymbol{x} \times \rho\boldsymbol{a})\, dv \tag{2.49}$$

We end up with

$$\int_{\mathcal{S}_p} (\boldsymbol{x} \times \rho\boldsymbol{a})\, dv = \int_{\mathcal{S}_p} \boldsymbol{x} \times \rho\boldsymbol{\gamma}\, dv + \int_{\mathcal{S}_p} \epsilon_{ijk}\sigma_{kj}\, dv + \int_{\mathcal{S}_p} \boldsymbol{x} \times \mathrm{div}(\boldsymbol{\sigma})\, dv \tag{2.50}$$

If we rearrange the relation in (2.50), we arrive at

$$\int_{\mathcal{S}_p} \underbrace{(\boldsymbol{x} \times (\rho\boldsymbol{a} - \rho\boldsymbol{\gamma} - \mathrm{div}(\boldsymbol{\sigma}))\, dv}_{\substack{\mathbf{0} \\ \text{due to the balance of linear momentum}}} = \int_{\mathcal{S}_p} \epsilon_{ijk}\sigma_{kj}\, dv \tag{2.51}$$

Due to the balance of linear momentum equation in (2.43), we obtain equality in (2.52):

$$\int_{\mathcal{S}_p} \epsilon_{ijk}\sigma_{kj}\, dv = \mathbf{0} \tag{2.52}$$

If we localize the integral domain $\mathcal{S}_p$ to a point, we find the expression in (2.53).

$$\epsilon_{ijk}\sigma_{kj} = \mathbf{0} \tag{2.53}$$

To make the equation in (2.53) more transparent, the relations are expressed as

$$\begin{aligned}
i = 1 &\mapsto \epsilon_{123}\sigma_{32} + \epsilon_{132}\sigma_{23} = \sigma_{32} - \sigma_{23} = 0 \\
i = 2 &\mapsto \epsilon_{231}\sigma_{13} + \epsilon_{213}\sigma_{31} = \sigma_{13} - \sigma_{31} = 0 \\
i = 3 &\mapsto \epsilon_{312}\sigma_{21} + \epsilon_{312}\sigma_{12} = \sigma_{21} - \sigma_{12} = 0
\end{aligned} \tag{2.54}$$

According to the results in (2.54), the Cauchy stress tensor is symmetric. Thus, this implies the symmetry of the second Piola Kirchhoff stress tensor $\boldsymbol{S}$ and the Kirchhoff stress tensor $\boldsymbol{\tau}$ as described in (2.55).

$$\boldsymbol{\sigma} = \boldsymbol{\sigma}^T, \quad \boldsymbol{S} = \boldsymbol{S}^T, \quad \boldsymbol{\tau} = \boldsymbol{\tau}^T \tag{2.55}$$

2.2.4 Balance of Energy (The First Law of Thermodynamics)

The energy equation is a result of the energy balance postulate of the first law of thermodynamics. The rate of change of kinetic energy ($\mathcal{K}$) and internal potential energy ($\mathcal{E}$) of spatial cut out body is equal to the summation of thermal ($\mathcal{Q}$) and mechanical power ($\mathcal{P}$) as expressed in (2.56).

$$\frac{d}{dt}(\mathcal{K} + \mathcal{E}) = \mathcal{P} + \mathcal{Q} \tag{2.56}$$

The external traction forces and the body forces act on the body $\mathcal{S}_p$ and the rate of this action is called the external mechanical power as shown in (2.57).

$$\mathcal{P}_{ext} = \int_{\partial \mathcal{S}_p} \boldsymbol{t} \cdot \boldsymbol{v} \, da + \int_{\mathcal{S}_p} \rho \boldsymbol{\gamma} \cdot \boldsymbol{v} \, dv \tag{2.57}$$

On the other hand, the outward heat flux acts on the boundary of the body $\partial \mathcal{S}_p$ and the internal heat source per unit volume r acts on the cut out body. The sum of these actions is the thermal power ($\mathcal{Q}$) defined as in (2.58).

$$\mathcal{Q} = - \int_{\partial \mathcal{S}_p} \boldsymbol{q} \cdot \boldsymbol{n} \, da + \int_{\mathcal{S}_p} \rho r \, dv \tag{2.58}$$

The kinetic energy is described in (2.59).

$$\mathcal{K} = \int_{\mathcal{S}_p} \frac{1}{2} \rho \boldsymbol{v} \cdot \boldsymbol{v} \, dv \tag{2.59}$$

Similarly, the internal potential energy is also defined as (2.60).

$$\mathcal{E} = \int_{\mathcal{S}_p} \rho e \, dv \tag{2.60}$$

where e is the mass-specific internal energy density.

We take some derivation and arrange the mechanical power expression as shown in

(2.61).

$$\mathcal{P}_{ext} = \int_{\partial \mathcal{S}_p} \boldsymbol{t} \cdot \boldsymbol{v}\, da + \int_{\mathcal{S}_p} \rho \boldsymbol{\gamma} \cdot \boldsymbol{v}\, dv$$

$$= \int_{\partial \mathcal{S}_p} (\sigma_{ij} n_j) v_i\, da + \int_{\mathcal{S}_p} \rho \gamma_i v_i\, dv$$

$$= \int_{\mathcal{S}_p} \frac{\partial (\sigma_{ij} v_i)}{\partial x_j}\, dv + \int_{\mathcal{S}_p} \rho \gamma_i v_i\, dv$$

$$= \int_{\mathcal{S}_p} (\frac{\partial \sigma_{ij}}{\partial x_j} + \gamma_i) v_i\, dv + \int_{\mathcal{S}_p} \sigma_{ij} \underbrace{\frac{\partial v_i}{\partial x_j}}_{l_{ij}}\, dv \qquad (2.61)$$

$$= \int_{\mathcal{S}_p} \rho \dot{v}_i v_i\, dv + \int_{\mathcal{S}_p} \sigma_{ij} l_{ij}\, dv$$

$$= \int_{\mathcal{S}_p} \rho \dot{\boldsymbol{v}} \cdot \boldsymbol{v}\, dv + \int_{\mathcal{S}_p} \boldsymbol{\sigma} : \boldsymbol{l}\, dv$$

When we use the $\boldsymbol{l} = \boldsymbol{d} + \boldsymbol{w}$ by using the rate of deformation and spin tensors concept, we rearrange the result in (2.61) to obtain

$$\mathcal{P}_{ext} = \ = \frac{d}{dt} \int_{\mathcal{S}_p} \frac{1}{2} \rho \boldsymbol{v} \cdot \boldsymbol{v}\, dv + \int_{\mathcal{S}_p} \boldsymbol{\sigma} : \boldsymbol{d}\, dv \qquad (2.62)$$

Moreover, we deal with the thermal power part in (2.58):

$$\mathcal{Q} = - \int_{\partial \mathcal{S}_p} q_i n_i\, da + \int_{\mathcal{S}_p} \rho r\, dv$$

$$= - \int_{\mathcal{S}_p} \frac{\partial q_i}{\partial x_i}\, dv + \int_{\mathcal{S}_p} \rho r\, dv \qquad (2.63)$$

$$= - \int_{\mathcal{S}_p} \operatorname{div}(\boldsymbol{q})\, dv + \int_{\mathcal{S}_p} \rho r\, dv$$

If we insert (2.62), (2.63), (2.59) and (2.60) into (2.56), we get

$$\frac{d}{dt} \int_{\mathcal{S}_p} (\frac{1}{2} \rho \boldsymbol{v}.\boldsymbol{v} + \rho e)\, dv = \frac{d}{dt} \int_{\mathcal{S}_p} \frac{1}{2} \rho \boldsymbol{v} \cdot \boldsymbol{v}\, dv + \int_{\mathcal{S}_p} \boldsymbol{\sigma} : \boldsymbol{d}\, dv$$

$$+ \int_{\mathcal{S}_p} (\rho r - \operatorname{div}(\boldsymbol{q}))\, dv \qquad (2.64)$$

When we rearrange the (2.64), we arrive at

$$\int_{\mathcal{S}_p} (\rho \dot{e} + \operatorname{div}(\boldsymbol{q}) - \boldsymbol{\sigma} : \boldsymbol{d} - \rho r)\, dv = 0 \qquad (2.65)$$

In addition to (2.65), the local form of the balance of energy in the Eulerian setting is given in (2.66) by localizing the result in (2.65):

$$\rho \dot{e} + \operatorname{div}(\boldsymbol{q}) - \boldsymbol{\sigma} : \boldsymbol{d} - \rho r = 0 \qquad (2.66)$$

2.2.5 Balance of Entropy (The Second Law of Thermodynamics)

The first law of thermodynamics specifies the conservation of energy but it does not determine the direction of a process restriction. There is a preferred direction of the process. For instance, the preferred direction of the heat flow between two systems at different temperatures is always from the warmer to cooler one, when thermal phenomena are considered. It will be expressed as an inequality stating that the internal entropy production rate is always non-negative and is positive for an irreversible process.

$$\dot{S} = \int_{\mathcal{S}_p} \frac{\rho r}{\theta} \, dv - \int_{\partial \mathcal{S}_p} \frac{\boldsymbol{q} \cdot \boldsymbol{n}}{\theta} \, da \tag{2.67}$$

where θ is absolute temperature and r is the internal heat supply per unit mass.

The rate of entropy change is given by

$$\dot{\mathcal{H}} = \frac{d}{dt} \int_{\mathcal{S}_p} \rho \eta \, dv \tag{2.68}$$

The second law can be regenerated as form in (2.69):

$$\frac{d}{dt} \int_{\mathcal{S}_p} \rho \eta \, dv \geq \int_{\mathcal{S}_p} \rho \frac{r}{\theta} \, dv - \int_{\partial \mathcal{S}_p} \frac{\boldsymbol{q} \cdot \boldsymbol{n}}{\theta} \, da \tag{2.69}$$

We can rewrite the above inequality as in (2.70) alternatively.

$$\Gamma := \int_{\mathcal{S}_p} \rho \gamma \, dv := \frac{d}{dt} \int_{\mathcal{S}_p} \rho \eta \, dv - \int_{\mathcal{S}_p} \rho \frac{r}{\theta} \, dv + \int_{\partial \mathcal{S}_p} \frac{\boldsymbol{q} \cdot \boldsymbol{n}}{\theta} \, da \geq 0 \tag{2.70}$$

where Γ is the total rate of entropy production, and γ is the mass specific spatial rate of entropy production.

We transform the second law inequality equation above into a totaly volume integral.

$$\int_{\partial \mathcal{S}_p} \frac{\boldsymbol{q} \cdot \boldsymbol{n}}{\theta} \, da = \int_{\partial \mathcal{S}_p} \frac{q_i n_i}{\theta} \, da = \int_{\mathcal{S}_p} \frac{\partial}{\partial x_i} \left(\frac{q_i}{\theta} \right) dv$$

$$= \int_{\mathcal{S}_p} \frac{1}{\theta} \frac{\partial q_i}{\partial x_i} \, dv - \int_{\mathcal{S}_p} \frac{1}{\theta^2} q_i \frac{\partial \theta}{\partial x_i} \, dv \tag{2.71}$$

$$= \int_{\mathcal{S}_p} \frac{1}{\theta} \operatorname{div}(\boldsymbol{q}) \, dv - \int_{\mathcal{S}_p} \frac{1}{\theta^2} \boldsymbol{q} \cdot \nabla_{\boldsymbol{x}} \theta \, dv$$

If we put (2.71) into (2.70), we obtain the rearranged the relation as shown in (2.72).

$$\int_{\mathcal{S}_p} \rho \gamma \, dv = \int_{\mathcal{S}_p} \rho \dot{\eta} \, dv - \int_{\mathcal{S}_p} \frac{\rho r}{\theta} \, dv + \int_{\mathcal{S}_p} \frac{\operatorname{div}(\boldsymbol{q})}{\theta} \, dv - \int_{\mathcal{S}_p} \frac{1}{\theta^2} \boldsymbol{q} \cdot \nabla_{\boldsymbol{x}} \theta \, dv \geq 0 \tag{2.72}$$

Then, the local form known Clausius-Duhem inequality (CDI) equation is given in (2.73) :

$$\rho\gamma = \rho\dot{\eta} - \rho\frac{r}{\theta} + \frac{\operatorname{div}(\boldsymbol{q})}{\theta} - \frac{1}{\theta^2}\boldsymbol{q}\cdot\nabla_{\boldsymbol{x}}\theta \geq 0 \tag{2.73}$$

We introduce the dissipation equation per unit deformed volume as (2.74):

$$\rho\mathcal{D} = \rho\theta\boldsymbol{\gamma} = \boldsymbol{\sigma}:\boldsymbol{d} - \rho\dot{e} + \rho\theta\dot{\eta} - \frac{1}{\theta^2}\boldsymbol{q}\cdot\nabla_{\boldsymbol{x}}\theta \geq 0 \quad (CDI) \tag{2.74}$$

We decompose the Clausius-Duhem Inequality (CDI) equation into two parts namely, the local Clausius-Planck Inequality (CPI) and the conductive Fourier Inequality (FI) as shown in (2.75).

$$
\begin{aligned}
\rho\mathcal{D}_{loc} &= \boldsymbol{\sigma}:\mathbf{d} - \rho\dot{e} + \rho\theta\dot{\eta} \geq 0 \qquad (CPI) \\
\rho\mathcal{D}_{con} &= -\frac{1}{\theta^2}\boldsymbol{q}\cdot\nabla_{\boldsymbol{x}}\theta \geq 0 \qquad\qquad (FI)
\end{aligned} \tag{2.75}
$$

The first inequality in (2.75) is in local terms and responsible for internal dissipation, on the other hand, the latter in (2.75) is responsible for dissipation due to conduction.

2.3   Theory of Frontal Polymerization and Polymerized Material Behavior

In this subsection, we consider the chemical, thermal and mechanical coupling phenomena in order to demonstrate the behavior of frontally cured polymers. A coupled problem of frontal polymerization thermo-mechanics is formulated in terms of three primary field variables, specifically the deformation map φ, the temperature θ and the degree of curing α.

Therefore, a chemo-thermo-mechanical state of a material point $\boldsymbol{X}$ at time t is defined as

$$\text{State}(\boldsymbol{X},t) := \{\boldsymbol{\varphi}(\boldsymbol{X},t), \theta(\boldsymbol{X},t), \alpha(\boldsymbol{X},t)\} \tag{2.76}$$

The basic set of equations required to solve the initial-boundary value problem (IBVP) of chemo-thermo-mechanics are the balance of linear momentum, the conservation of energy, and the chemical evolution equation for the degree of curing. Therefore, we introduce the differential equations that govern the evolution of the state variables.

In what follows, we consider a certain spatial body $\mathcal{S}$ closed by the boundary $\partial\mathcal{S}$ as shown in Figure 2.1. The following linear momentum equation recalled from (2.43)

31

in order to represent the quasi-static stress equilibrium:

$$\text{div}(\boldsymbol{\sigma}) + \boldsymbol{B} = \boldsymbol{0} \tag{2.77}$$

where $\boldsymbol{B}$ is equal to $\rho\boldsymbol{\gamma}$.

It governs the evolution of the deformation field $\boldsymbol{\varphi}(\boldsymbol{X}, t)$ along with the Dirichlet and Neumann boundary conditions.

In the thermo-chemo-mechanics problem, we also utilize the Helmholtz free energy to characterize the thermodynamic state as described in (2.78).

$$\Psi := e - \theta\eta \tag{2.78}$$

The first law of thermodynmamics states the power equilibrium as described in (2.79).

$$\rho\dot{e} + \text{div}(\boldsymbol{q}) - \boldsymbol{\sigma} : \boldsymbol{d} - \rho r = 0 \tag{2.79}$$

In other words, the equality in (2.79) describes the rate of energy balance in terms of the volume-specific internal energy e, the internal stress power $\boldsymbol{\sigma} : \boldsymbol{d}$, and the externally supplied thermal power comprised of the outward heat flux vector $\boldsymbol{q}$ and the given volume-specific external heat source ρr.

However, the first law does not place any restriction on the direction of a process. The preferred direction of the heat flow due to the thermal heating defined at beginning of the problem in between two systems is always from the warmer to cooler one. Thus, we need the preferred direction in order to simulate correct behavior of material nature. This limitation will be expressed below mathematically as an inequality stating that the internal entropy production rate is always non-negative and is positive for an irreversible process.

When we take a time derivative of the Helmholtz free energy function, and rearrange them, we obtain

$$\dot{e} = \dot{\Psi} + \dot{\theta}\eta + \theta\dot{\eta} \tag{2.80}$$

We put (2.80) into (2.79), and can be expressed as in (2.81).

$$\rho\theta\dot{\eta} = \underbrace{\boldsymbol{\sigma} : \boldsymbol{d} - \rho\dot{\Psi} - \rho\dot{\theta}\eta}_{\rho\mathcal{D}_{loc}} \underbrace{- \text{div}(\boldsymbol{q}) + \rho r}_{Q} \tag{2.81}$$

where, $\rho\mathcal{D}_{loc}$ is the local dissipation, and Q accounts for the local thermal power. We can also rewrite the Clausius-Planck Inequality by inserting (2.80) into first relation in (2.75) in Eulerian setting.

$$\rho\mathcal{D}_{loc} = \boldsymbol{\sigma} : \boldsymbol{d} - \rho\dot{\Psi} - \rho\dot{\theta}\eta \geq 0 \quad \text{in} \quad \mathcal{S} \tag{2.82}$$

The Lagrangian counterpart is

$$\rho_0\mathcal{D}_{loc} = \boldsymbol{S} : \frac{1}{2}\dot{\boldsymbol{C}} - \rho_0\dot{\Psi} - \rho_0\dot{\theta}\eta \geq 0 \quad \text{in} \quad \mathcal{B} \tag{2.83}$$

The right Cauchy-Green tensor in (2.84) is introduced to use in the functional form of the free energy function. The functional form of the free energy function can be written as

$$\Psi = \Psi(\boldsymbol{C}, \theta, \alpha) \quad \text{with} \quad \boldsymbol{C} = \boldsymbol{F}^T\boldsymbol{F} \tag{2.84}$$

Then, we can rewrite the expression in (2.83) with help of functional form of the free energy function in (2.84) as shown in (2.85).

$$\rho_0\mathcal{D}_{loc} = [\boldsymbol{S} - 2\rho_0\partial_{\boldsymbol{C}}\Psi] : \frac{1}{2}\dot{\boldsymbol{C}} - \rho_0[\eta + \partial_\theta\Psi]\dot{\theta} - \rho_0\partial_\alpha\Psi\dot{\alpha} \geq 0 \tag{2.85}$$

At this point, we use the Coleman's exploitaiton method [30] to satisfy the thermodynamical consistency. Thus, it implies the particular form of the constitutive equations described in (2.86).

$$\boldsymbol{S} = 2\rho_0\partial_{\boldsymbol{C}}\Psi$$
$$\eta = -\partial_\theta\Psi \tag{2.86}$$

Therefore, the local dissipation reduces to the expression in (2.87).

$$\rho_0\mathcal{D}_{loc}^{red} = -\rho_0\partial_\alpha\Psi\dot{\alpha} \geq 0 \tag{2.87}$$

We define the chemical driving force by using the relation in (2.87), and we obtain

$$\rho_0\mathcal{D}_{loc}^{red} = \mathcal{A}_\alpha\dot{\alpha} \geq 0 \quad \text{where} \quad \mathcal{A}_\alpha := -\rho_0\partial_\alpha\Psi(\boldsymbol{C}, \theta, \alpha) \tag{2.88}$$

We can describe the chemical part as the main dissipative mechanism for the frontal polymerization which is highly exothermic. $\mathcal{A}_\alpha$ and α are energy conjugate variables since the chemical driving force $(\mathcal{A}_\alpha)$ is the partial derivative with respect to degree of curing (α) as shown in (2.88). Due to the minor coupling with deformation, the chemical driving force $(\mathcal{A}_\alpha)$ can be considered to be a function of temperature (θ) and the degree of curing (α) as expressed in (2.89).

$$\mathcal{A}_\alpha = \mathcal{A}_\alpha(\theta, \alpha) \tag{2.89}$$

33

Thanks to this observation and thermally activated polymerization process, we postulate general form of the evolution equation for the degree of curing (α) in (2.90).

$$\dot{\alpha} = f(\theta, \alpha) \tag{2.90}$$

where f is defined as an Arhenius and Prout-Tompkins type equation dependent on θ and α. It is explained in more detail in Chapter 3.

It is obvious that $\dot{\alpha}$ is always positive, so the thermodynamical consistency depends on $\mathcal{A}_\alpha$. In other words, when the $\mathcal{A}_\alpha$ is positive, the thermodynamical consistency is satisfied.

2.3.1 Transient Heat Conduction Equation

The energy equation is a result of the energy balance postulate of the first law of thermodynamics. Loeffel and Anand [31] develops the energy balance equations with inertial effects but they neglect the kinetic energy. The same methodology are used in our study, and the conservation of energy equation in (2.79) recalled as shown in (2.91).

$$\rho \dot{e} + \mathrm{div}(\boldsymbol{q}) - \boldsymbol{\sigma} : \boldsymbol{d} - \rho r \tag{2.91}$$

where r is the heat source per unit mass.

We used the Piola transformation to transform the flux action on a spatial surface onto their material counterpart as described in (2.92).

$$\boldsymbol{Q} \cdot \boldsymbol{N} dA := \boldsymbol{q} \cdot \underbrace{\boldsymbol{n} da}_{J\boldsymbol{F}^{-T}\boldsymbol{N} dA} \quad \text{with} \quad \boldsymbol{Q} = J\boldsymbol{q}\boldsymbol{F}^{-T} \tag{2.92}$$

We can write the identity in (2.93) by using (2.92).

$$J \, \mathrm{div}(\boldsymbol{q}) = \mathrm{DIV}(\boldsymbol{Q}) \tag{2.93}$$

Therefore, we multiply (2.91) with Jacobi map (J) and rearrange some terms according to derivations in (2.92) and (2.93) to extend the conservation of energy equation into the Lagrangian setting as expressed in (2.94).

$$\rho_0 \dot{e} = \boldsymbol{S} : \frac{1}{2}\dot{\boldsymbol{C}} + \rho_0 r_b - \mathrm{DIV}(\boldsymbol{Q}) \tag{2.94}$$

If we insert (2.80) which is time derivative of (2.78) into (2.91), and then express the relation as in (2.95).

$$\rho_0 \dot{\eta}\theta = \boldsymbol{S} : \frac{1}{2}\dot{\boldsymbol{C}} + \rho_0 r_b - \text{DIV}(\boldsymbol{Q}) - \rho_0 \dot{\Psi} - \rho_0 \eta \dot{\theta} \qquad (2.95)$$

We rearrange the (2.95), and we arrive

$$\rho_0 \dot{\eta}\theta = \underbrace{\boldsymbol{S} : \frac{1}{2}\dot{\boldsymbol{C}} - \rho_0 \dot{\Psi} - \rho_0 \eta \dot{\theta}}_{\rho_0 \mathcal{D}_{loc}} + \underbrace{\rho_0 r_b - \text{DIV}(\boldsymbol{Q})}_{Q} \qquad (2.96)$$

Then, we can obtain the time derivative of entropy in (2.97) by using functional free energy relation in (2.86).

$$\begin{aligned}
\dot{\eta} &= -\overline{\partial_\theta \Psi(\boldsymbol{C}, \theta, \alpha)} \\
&= -\frac{\partial^2 \Psi}{\partial \theta^2}\dot{\theta} - \frac{\partial^2 \Psi}{\partial \alpha \partial \theta}\dot{\alpha} - 2\frac{\partial^2 \Psi}{\partial \boldsymbol{C} \partial \theta} : \frac{1}{2}\dot{\boldsymbol{C}}
\end{aligned} \qquad (2.97)$$

The specific heat capacity is derived as shown in (2.98).

$$c := -\theta\frac{\partial^2 \Psi}{\partial \theta^2} \qquad (2.98)$$

If we can simplify (2.96), we obtain

$$\rho_0 c\dot{\theta} = \rho_0 \mathcal{D}_{loc} + \rho_0 \theta \partial^2_{\alpha\theta}\Psi\dot{\alpha} + \rho_0 \theta \partial^2_{\boldsymbol{C}\theta}\Psi : \dot{\boldsymbol{C}} + Q \qquad (2.99)$$

We group the terms in (2.99), and they are named as shown in (2.100).

$$\rho_0 c\dot{\theta} = \underbrace{(\mathcal{A}_\alpha - \theta\partial_\theta\mathcal{A}_\alpha)\dot{\alpha}}_{\text{chemical heating} \quad \mathcal{H}_c} + \underbrace{\theta\partial_\theta\boldsymbol{S} : \frac{1}{2}\dot{\boldsymbol{C}}}_{\text{thermoelastic heating}} + \underbrace{Q}_{\mathcal{H}_e} \qquad (2.100)$$

To make the meaning of (2.100) more clear, we focus on the terms in (2.44) in depth. During the polymerization, exothermic energy is released. This energy is measured with the help of differential scanning calorimetry experiment. We assume that there is a linear relationship between degree of curing and main dissipation mechanism. Thus, we continue by considering that this released energy is equal to $\mathcal{A}_\alpha - \theta\partial_\theta\mathcal{A}_\alpha$.

The second term on the right hand side in (2.100) ($\theta\partial_\theta\boldsymbol{S} : \frac{1}{2}\dot{\boldsymbol{C}}$) is the thermoelastic heating and is negligible compared to other terms. We can reexpress the relation in (2.100) as in (2.101):

$$\rho_0 c\dot{\theta} = \mathcal{H}_c + \mathcal{H}_e \qquad (2.101)$$

After finalizing all derivations regarding the balance laws, we have three differential equations to evaluate. These differential equations are tabulated in Table 2.1.

Table 2.1: The summary of primary field, governing equation and initial-boundary conditions

Field	Problem	Equation	#	BC's/IC's
$\varphi(\boldsymbol{X}, t)$	Mechanical	$\operatorname{div}(\boldsymbol{\sigma}) + \boldsymbol{B} = 0$	(2.77)	$\varphi = \bar{\varphi}$ on $\partial \mathcal{S}_\varphi$
				$\boldsymbol{\sigma} \boldsymbol{n} = \boldsymbol{t}$ on $\partial \mathcal{S}_t$
$\theta(\boldsymbol{X}, t)$	Thermal	$\rho_0 c \dot{\theta} = \mathcal{H}_c + \mathcal{H}_e$	(2.101)	$\theta = \bar{\theta}$ on $\partial \mathcal{B}_\theta$
				$\boldsymbol{Q} \cdot \boldsymbol{N} = H_\theta$ on $\partial \mathcal{B}_H$
				$\theta_0(\boldsymbol{X}) = \theta(\boldsymbol{X}, t = 0)$ in $\mathcal{B}$
$\alpha(\boldsymbol{X}, t)$	Chemical	$\dot{\alpha} = f(\alpha, \theta)$	(2.90)	$\alpha_0(\boldsymbol{X}) = \alpha(\boldsymbol{X}, t = 0)$ in $\mathcal{B}$

36

CHAPTER 3

CONSTITUTIVE EQUATIONS

The governing differential equations of the chemo-thermo-mechanical problem of frontal polymerization, given in Table (2.1), are coupled through the constitutive equations for the stress tensor $\boldsymbol{\sigma}$ in (2.77), the chemical equation in (2.90), and the transient heat conduction equation in (2.101). Moreover, we need to define the chemical driving force $\mathcal{A}_\alpha$ and the heat flux vector $\boldsymbol{q}$ in (2.101) in the theoretical foundation for curing of polymer. Thus, we aim to develop the constitutive models in this section.

3.1 Curing and Growth in Rigidity and Strength

The polymerization process should be modeled in order to make precise prediction in the mechanical properties, defect and shape etc. of the final product by using chemo-thermo-mechanical tools. Therefore, chemo-thermo-mechanical coupled models have been studied and proposed previously in literature such as [17, 22]. Thus, we also need to advance the computational model for the initiation and propagation of a polymerization front in polymer, so we developed the chemo-thermo-mechanical model based on the coupled system of differential equation studied by Sottos and coworkes [3]. Furthermore, the classical Prout-Tompkins autocatalytic model depended on the degree of curing $\alpha(\theta, t)$ and the temperature $\theta(t)$ [3] is used for the chemical heating in (3.1).

The evolution of the degree of curing is described as in (3.1).

$$\frac{\partial \alpha}{\partial t} = f(\alpha, \theta) \tag{3.1}$$

The degree of curing α characterizing the chemical state is an essential field variable

representing the growth of rigidity and strength of frontally polymerized material. This body is shown as a closed system that mass exchange with outside of the system is not permissible, and the degree of curing is considered as a thermodynamical internal state variable whose thermally activated evolution is governed by an Arrhenius-type equation.

The modeling of the curing evolution is essential for an accomplished manufacturing process which satisfies the conversion of the liquid monomer to robust polymer in both mechanical and thermal settings. Thus, we can focus on more transparent the degree of curing evolution equation in (3.2).

$$f(\alpha, \theta) = A \exp(-\frac{E}{R\theta})(1-\alpha)^n \alpha^m \frac{1}{1 + \exp[C(\alpha - \alpha_c)]} \tag{3.2}$$

where θ is the absolute temperature. A and E are the pre-exponential factor and the activation energy, respectively. C and α_c are constant parameters capturing the diffusion at higher temperature. Moreover, n, m are parameters denoting the order of the reactions.

Sottos and coworkers [3] deal with the optimization of the nonlinear fitting for the cure rate evolution obtained from the Differential Scanning Calorimetry experiment to specify the cure kinetic parameters which are A, E, n, m, C and α_c.

We deal with the the ordinary differential equation (ODE) problem of the degree of curing evolution with the help of the experiment result obtained by Sottos and coworkers [1]. The evolution of the degree of curing depends on temperature and polymerization degree at a quadrature point. Hence, it is solved as an internal variable by discretizing governing equation in time. In turn, we apply the Backward Euler time integration scheme to the governing ordinary differential equation in (3.2). Then, we linearize the equation and apply the iterative Newton-Raphson method.

$$\alpha = \alpha_n + \Delta t \dot{\alpha} \quad \text{with} \quad \dot{\alpha} = f(\theta, \alpha)$$
$$\alpha = \alpha_n + \Delta t f(\theta, \alpha) \tag{3.3}$$

Given the temperature, we form the residual of the curing evolution equation in (3.4).

$$r(\alpha, \theta) = \alpha - \alpha_n - \Delta t f(\theta, \alpha) \tag{3.4}$$

38

Then, we linearize the residual term in (3.5).

$$\text{Lin}(r(\alpha, \theta))|_{\alpha=\bar{\alpha}} = \bar{r} + \bar{a}(\alpha - \bar{\alpha})$$

where (3.5)

$$\bar{r} = r(\bar{\alpha}, \theta) \quad \text{and} \quad \bar{a} := \frac{\partial r}{\partial \alpha}|_{\theta, \bar{\alpha}}$$

Consequently, we try to solve the linearized equation by iterating for α in (3.6).

$$\alpha = \bar{\alpha} - \bar{a}^{-1}\bar{r}(\alpha, \theta) \tag{3.6}$$

There is a missing term in the transient heat conduction equation in (2.101), and we obtain this term by using consistency condition. Hence, we also derive the derivative of the curing evolution equation residual (r) with respect to temperature θ as shown in (3.7).

$$\frac{d\bar{r}(\alpha, \theta)}{d\theta} = \frac{\partial r}{\partial \theta}|_{\alpha} + \underbrace{\frac{\partial r}{\partial \alpha}|_{\theta}}_{\bar{a}} \cdot \frac{\partial \alpha}{\partial \theta} = 0$$

$$\frac{\partial \alpha}{\partial \theta} = -\bar{a}^{-1} \cdot \frac{\partial \bar{r}}{\partial \theta}|_{\alpha} \tag{3.7}$$

We used the staggered solution scheme to decrease the computation time. In the staggered solution scheme, we used the nodal temperature values at the previous time step in order to obtain the chemical heating part. Recall the chemical evolution equation in (3.2) to explain the staggered solution approach application with our chemo-thermal problem.

$$f(\alpha, \theta_n) = A \exp(-\frac{E}{R\theta_n})(1 - \alpha)^n \alpha^m \frac{1}{1 + \exp[C(\alpha - \alpha_c)]} \tag{3.8}$$

where θ_n is the nodal temperature values at the previous time step.

The evolution of the degree of curing depends on temperature and polymerization rate at a quadrature point as seen in (3.8). The temperature value in (3.8) is taken from previous thermal solution step. Then, the derivative of degree of curing with respect to temperature in (3.7) is removed from the thermal heating source part.

The curing induced polymer strength is modeled through the reaction conversion expressions that evaluate the mechanical properties in terms of degree of curing. We consider the following relation for the evolution of mechanical properties with the

39

curing progress in (3.9):

$$\Lambda = \Lambda_f - (\Lambda_f - \Lambda_i) \tanh(\frac{\alpha_n - 0.04}{-T_f})$$

$$\mu = \mu_f - (\mu_f - \mu_i) \exp(\frac{\alpha_n}{-T_f})$$

$$\alpha_\theta = \alpha_{\theta f} - (\alpha_{\theta f} - \alpha_{\theta i}) \exp(\frac{\alpha_n}{-T_f}) \qquad (3.9)$$

$$\xi_c = \xi_{cf} - (\xi_{cf} - \xi_{ci}) \exp(\frac{\alpha_n}{-T_f})$$

where Λ_f is the Lamé constant of polymer. Λ_i is the Lamé constant of monomer. μ_f is the ground shear modulus of polymer. μ_i is the ground shear modulus of monomer. $\alpha_{\theta f}$ is the thermal expansion coefficient of polymer. $\alpha_{\theta i}$ is the thermal expansion coefficient of monomer. ξ_{cf} is the chemical shrinkage coefficient of polymer. ξ_{ci} is the chemical shrinkage coefficient of monomer. T_f is a constant in switch function.

Hereby, the evolution of the mechanical and thermal properties are enhanced when the degree of curing completed, or the polymer is fully cured.

3.2 Thermal Conductivity and Chemical Heating

In this subsection, we introduce the constitutive relation for the thermal conductivity and chemical heating part of the polymerization process which is essential to simulate the initiation and propagation of a polymerization front. We solve the coupled system of partial differential equations depended on degree of curing α and temperature θ [3].

First of all, recall the relation in (2.101), and we derive the evolution and conduction relations for thermal part

$$\rho_0 c \dot{\theta} = \mathcal{H}_c + \mathcal{H}_e \qquad (3.10)$$

where $\mathcal{H}_c$ indicates the chemical heating due to the curing process, and $\mathcal{H}_e$ indicates the sum up of the internal heat source and heat flux.

Figure 3.1: The simulation of the carbon fiber reinforced composite frontally cured

The initiation, propagation, and chemical heating, as shown in numerical simulation in Figure 3.1, are modeled through the differential equation in (3.11). Therefore, the differential equation in (3.11) is a basic relation for modeling of the frontal polymerization.

$$\rho_0 c \dot{\theta} = \mathcal{A}_\alpha \dot{\alpha} + \rho_0 r_b - \mathrm{DIV}(\boldsymbol{Q}) \tag{3.11}$$

The relation in (3.11) is responsible for the local energy storage for changing temperature. Also, the first term in the right hand side of (3.11) denotes the chemical heating. It is specific for the polymerization type, so this term denotes the reaction enthalpy obtained by the experiments and parameter fitting studies conducted by the Sottos and coworkers [1]. To make it clearer, we encapsulate Sottos and coworkers' experiments and their findings briefly. First of all, Sottos, Geubelle and coworkers [1] carry out the Differential Scanning Calorimetry (DSC) experiments to determine the enthalphy of reaction by integrating the heat flow over the exothermic reaction. Thus, the enthalpy of reaction depends on heat but our relation in the right hand side of (2.101) seems to depend on only the degree of curing α. However, the degree of curing α intrinsically depends on temperature which is described in (3.2). The final term is related to thermal conduction and internal heat source. Thanks to Fourier's Law, we derive the inequality in (3.12):

$$-\frac{1}{\theta^2} \boldsymbol{Q} \cdot \nabla_{\boldsymbol{X}} \theta \geq \boldsymbol{0} \quad \text{where} \quad \boldsymbol{Q} = -\boldsymbol{K} \nabla_{\boldsymbol{X}} \theta \tag{3.12}$$

If we put more apparent flux term into (3.12), we obtain

$$\frac{1}{\theta^2} \boldsymbol{K} : (\nabla_{\boldsymbol{X}} \theta \otimes \nabla_{\boldsymbol{X}} \theta) \geq 0 \tag{3.13}$$

According to the relation in (3.13), the heat flux is proportional to the change of the temperature with respect to space and heat is conducted from hot part to cold part of the body for the conductivity tensor (K) positive definite. We use the isotropic conduction in our study, but it is possible to extend the directional conduction according to composite manufacturing.

3.3 Chemo-Thermo-Mechanic Elasticity

In this subsection, we develop the Neo-Hooken elasticity model for the stress and consistent tangent moduli derivation.
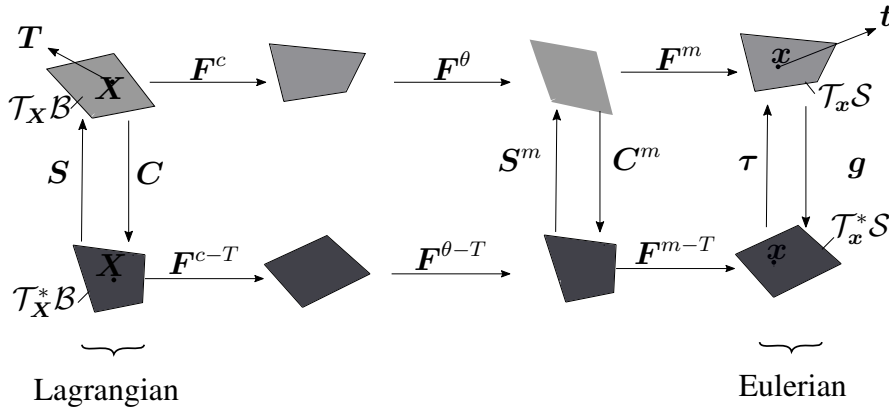
Figure 3.2: Schematic representation of the commutative diagram

Moreover, the deformation gradient is assumed to be decomposed into product of mechanical, thermal and chemical parts which was firstly studied by Höfer and Lion [17] as shown in (3.14) and depicted in the commutative diagram in Figure 3.2.

$$\boldsymbol{F} = \boldsymbol{F}^m \boldsymbol{F}^\theta \boldsymbol{F}^c \quad \text{where} \quad \boldsymbol{F}^\theta = J_\theta^{1/3}\mathbf{1}, \boldsymbol{F}^c = J_\alpha^{1/3}\mathbf{1} \tag{3.14}$$

We use the volumetric and isochoric split terms in our finite strain derivation. The commutative diagram of the multiplicative decomposition is depicted in Figure 3.3.

Then, the mechanical deformation gradient is expressed as (3.15).

$$\boldsymbol{F}^m = \boldsymbol{F}\boldsymbol{F}^{c-1}\boldsymbol{F}^{\theta-1} \tag{3.15}$$

42
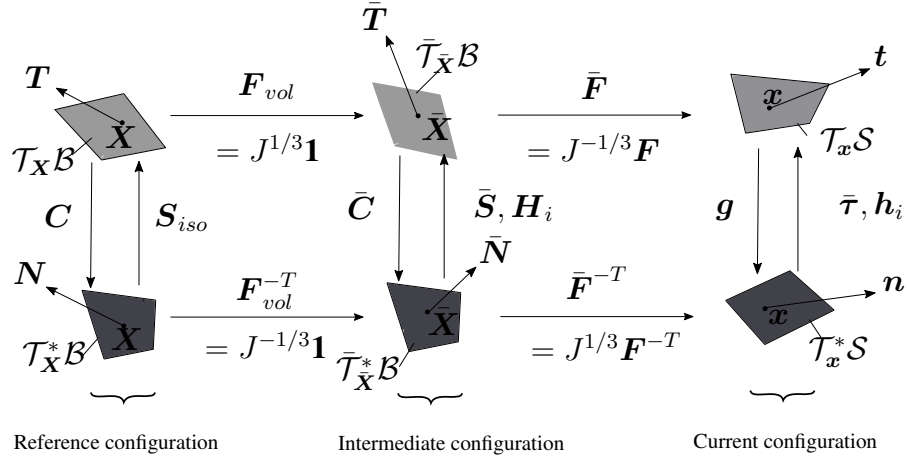
Figure 3.3: Commutative diagram of the isochoric-volumetric split approach

According to the decomposition of the deformation gradient in (3.15), we obtain the right Cauchy-Green tensor for mechanical part as expressed in (3.16)

$$\boldsymbol{C}^m = \xi\boldsymbol{C} \quad \text{with} \quad \xi = J_\theta^{-2/3} J_\alpha^{-2/3} \tag{3.16}$$

The free energy function is formulated as in (3.17) to provide the consistent stress response derivation.

$$\Psi(\boldsymbol{C},\theta,\alpha) := \Psi^m(\boldsymbol{C},\theta,\alpha) + \Psi^\theta(\theta) + \Psi^\alpha(\alpha,\theta) \tag{3.17}$$

We are interested in only mechanical free energy function in this section and we split the free energy function into the two parts such as volumetric and isocohoric free energy functions as shown in (3.18).

$$\Psi^m(\boldsymbol{C},\theta,\alpha) = \mathcal{U}(J_m) + \bar{\Psi}^m(\bar{\mathcal{I}}_1^m)$$
$$\text{where} \quad J_m^2 = \det(\boldsymbol{C}^m), \quad \bar{\mathcal{I}}_1^m = \operatorname{tr}(\bar{\boldsymbol{C}}^m) \tag{3.18}$$

where $\mathcal{U}(J)$ and $\bar{\Psi}(\bar{\mathcal{I}}_1^m)$ are the volumetric free energy function and the isochoric free energy function, respectively.

Moreover, the mechanical part of $\boldsymbol{F}$ split into volumetric and isochoric part. Owing to multiplicative split, an intermediate configuration $\mathcal{T}_{\boldsymbol{X}}\mathcal{B}$ and $\mathcal{T}_{\boldsymbol{X}}^*\mathcal{B}$ are introduced as expressed in (3.19)

$$\boldsymbol{F}^m = J_m^{1/3}\bar{\boldsymbol{F}}^m, \quad \bar{\boldsymbol{F}}^m = J_m^{-1/3}\boldsymbol{F}^m$$
$$\bar{\boldsymbol{C}}^m := \bar{\boldsymbol{F}}^{mT}\bar{\boldsymbol{F}}^m = J_m^{-2/3}\boldsymbol{C}^m \tag{3.19}$$
$$\bar{\mathcal{I}}_1^m = \operatorname{tr}(\bar{\boldsymbol{C}}^m)$$

43

We conduct the necessary derivation in Lagrange setting for the Lagrangian stress and tangent moduli. Then, we applied the push-forward operation to obtain Eulerian counterpart for the finite element formulation.

The isochoric part of the mechanical right Cauchy-Green tensor shown in the first relation in (3.20) is differentiated with respect to the mechanical right Cauchy-Green tensor in the second relation in (3.20) and we obtained the deviatoric projection.

$$
\begin{aligned}
\bar{\boldsymbol{C}}^m &= J_m^{-2/3}\boldsymbol{C}_m \\
\partial_{\boldsymbol{C}^m}\bar{\boldsymbol{C}}^m &= J_m^{-2/3}\mathbb{I} - \frac{-2}{3}J_m^{(-2/3-1)}\boldsymbol{C}^m \otimes \frac{J_m}{2}\boldsymbol{C}_m^{-1} \\
&= J_m^{-2/3}[\mathbb{I} - \frac{1}{3}\boldsymbol{C}^m \otimes \boldsymbol{C}^{m-1}]
\end{aligned}
\tag{3.20}
$$

We derive the volumetric stress response in (3.21) in the following part of the this chapter by using derivation in (3.20).

Volumetric Response:

We calculate the stress term directly using the free energy function. Thus, we take a derivative of the free energy function with respect to right Cauchy-Green tensor $\boldsymbol{C}^m$ as described in (3.21) for the volumetric stress response.

$$
\begin{aligned}
\boldsymbol{S}_{vol}^m &= 2\partial_{\boldsymbol{C}^m}\mathcal{U}(J_m) = \mathcal{U}'(J_m)2\partial_{\boldsymbol{C}^m}J_m \\
\boldsymbol{S}_{vol}^m &= \mathcal{P}(J_m)J_m\boldsymbol{C}^{m-1}
\end{aligned}
\tag{3.21}
$$

where $\mathcal{P}(J_m)$ is totally equal to $\mathcal{U}'(J_m)$.

The consistent tangent moduli are calculated by evaluating the material parameters to stimulate the curing process of polymer. Then, the moduli are calculated as described in (3.22).

$$
\begin{aligned}
\mathbb{C}_{vol}^m &= 2\partial_{\boldsymbol{C}_m}\boldsymbol{S}^m \\
&= [\mathcal{P}'(J_m) + \mathcal{P}(J_m)]\boldsymbol{C}^{m-1} \otimes J_m\boldsymbol{C}^{m-1} - 2\mathcal{P}(J_m)J_m\mathbb{I}_{\boldsymbol{C}^{m-1}} \\
&= J_m[\mathcal{P}'(J_m) + \mathcal{P}(J_m)]\boldsymbol{C}^{m-1} \otimes \boldsymbol{C}^{m-1} - 2\mathcal{P}(J_m)J_m\mathbb{I}_{\boldsymbol{C}^{m-1}}
\end{aligned}
\tag{3.22}
$$

We derived the incremental stress equation as shown in (3.23) after completing the evolution of the tangent moduli.

$$
\begin{aligned}
\Delta\boldsymbol{S}_{vol}^m &= \mathbb{C}_{vol}^m : \frac{1}{2}\Delta\boldsymbol{C}^m \\
\boldsymbol{S}_{vol}^m &= (\boldsymbol{S}_{vol}^m)_n + \Delta\boldsymbol{S}_{vol}^m
\end{aligned}
\tag{3.23}
$$

However, the stress relation in (3.23) is responsible for only mechanical part, so we extend it to total stress term. We derive the relation between total stress and mechanical stress as shown in (3.24). It is none other than the multiplication mechanical stress tensor with constant term devoted for thermal and chemical effects.

$$\boldsymbol{S}_{vol} = \boldsymbol{S}_{vol}^m : \partial_{\boldsymbol{C}} \boldsymbol{C}^m = \boldsymbol{S}_{vol}^m : \xi(\alpha, \theta)\mathbb{I} = \xi \boldsymbol{S}_{vol}^m \tag{3.24}$$

Then, we take the derivative of mechanical stress term with respect to right Cauchy-Green tensor, and we arrive the updated consistent tangent moduli as expressed in (3.25).

$$\mathbb{C}_{vol} = 2\partial_{\boldsymbol{C}} \boldsymbol{S}_{vol}^m = 2\partial_{\boldsymbol{C}^m}(\boldsymbol{S}_{vol}^m \xi) : \partial_{\boldsymbol{C}} \boldsymbol{C}^m = \xi^2 \mathbb{C}_{vol}^m \tag{3.25}$$

Bazant [32], Lackner and Mang [33] claim that the new elements of the concrete formed by new bonds within the micro-structure already formed which are initially in the load-free state can participate in carrying the load. The same analogy is also studied by Höfer and Lion [17]. Thus, based on the knowledge from the above studies [32, 17], we think that the new polymers formed do not directly participate in carrying the load since it will create an inconsistency with the second law of thermodynamics. Thus, we decided to use the incremental formula summarized in (3.26).

The incremental part for the volumetric response is :

$$\begin{aligned} \Delta \boldsymbol{S}_{vol}^m &= \mathbb{C}_{vol}^m : \frac{1}{2}\Delta \boldsymbol{C}_{vol}^m \\ \boldsymbol{S}_{vol}^m &= (\boldsymbol{S}_{vol}^m)_n + \Delta \boldsymbol{S}_{vol}^m \\ \boldsymbol{S}_{vol} &= \xi \boldsymbol{S}_{vol}^m \\ \mathbb{C}_{vol} &= \xi^2 \mathbb{C}_{vol}^m \end{aligned} \tag{3.26}$$

Isochoric Response:

We proceed with the derivation similar to the volumetric response. The only difference is that this part is responsible for the isochoric stress evolution. Thus, we take the derivative of isochoric free energy function with respect to mechanical right Cauchy-Green tensor as described in (3.27).

$$\bar{\boldsymbol{S}}_{iso}^m = 2\partial_{\bar{\boldsymbol{C}}^m} \bar{\Psi}(\bar{\mathbb{I}}^m) \tag{3.27}$$

If we rewrite relation in (3.28), we end up with

$$\begin{aligned} \boldsymbol{S}_{iso}^m &= 2s_1^m J_m^{-2/3}\mathbf{1} : [\mathbb{I} - \frac{1}{3}\boldsymbol{C}^m \otimes \boldsymbol{C}^{m-1}] \\ &= 2s_1^m J_m^{-2/3}[\mathbf{1} - \frac{1}{3}\operatorname{tr}(\boldsymbol{C}^m)\boldsymbol{C}^{m-1}] \end{aligned} \tag{3.28}$$

where $s_1^m := \partial_{\mathbb{I}_1^m}\bar{\Psi} = \frac{\mu}{2}$

Thus, we consider s_1^m as a constant in the subsequent derivation. Then, we need to update the consistent tangent moduli, so we take a derivative of isochoric stress response with respect to mechanical right Cauchy-Green tensor as in (3.28).

$$\begin{aligned} \mathbb{C}_{iso}^m = 2\partial_{\boldsymbol{C}^m}\boldsymbol{S}_{iso}^m &= 4s_1^m[\mathbf{1} - \frac{1}{3}\operatorname{tr}(\boldsymbol{C^m})\boldsymbol{C^{m-1}}] \otimes -\frac{2}{3}\mathbf{J_m^{(-2/3-1)}}\frac{\mathbf{J_m}}{2}\boldsymbol{C^{m-1}} \\ &+ 4s_1^m J_m^{-2/3}[-\frac{1}{3}\boldsymbol{C}^{m-1} \otimes \mathbf{1} + \frac{1}{3}\operatorname{tr}(\boldsymbol{C}^m)\mathbb{I}_{\boldsymbol{C}^{m-1}}] \end{aligned} \tag{3.29}$$

When we rewrite the expressions in (3.29), we arrive at

$$\begin{aligned} \mathbb{C}_{iso}^m &= \frac{4}{3}s_1^m J_m^{-2/3}[\frac{1}{3}\operatorname{tr}(\boldsymbol{C}^m)\boldsymbol{C}^{m-1} \otimes \boldsymbol{C}^{m-1} \\ &- (\mathbf{1} \otimes \boldsymbol{C}^{m-1} + \boldsymbol{C}^{m-1}\mathbf{1}) + \operatorname{tr}(\boldsymbol{C}^m)\mathbb{I}_{\boldsymbol{C}^{m-1}}] \end{aligned} \tag{3.30}$$

Then, we derive the total isochoric stress response as expressed in (3.31).

$$\begin{aligned} \boldsymbol{S}_{iso} &= 2s_1^m\mathbf{1} : J_m^{-2/3}[\mathbb{I} - \frac{1}{3}\boldsymbol{C}^m \otimes \boldsymbol{C}^{m-1}] : \xi\mathbb{I} \\ &= 2\xi s_1^m J_m^{-2/3}[\mathbf{1} - \frac{1}{3}tr(\boldsymbol{C}^m)\boldsymbol{C}^{m-1}] \\ &= 2s_1^m J^{-2/3}[\mathbf{1} - \frac{1}{3}\operatorname{tr}(\boldsymbol{C})\boldsymbol{C}^{-1}] \end{aligned} \tag{3.31}$$

We summarize the derivation regarding the stress and tangent moduli for isochoric part as described in (3.32).

$$\begin{aligned} \boldsymbol{S}_{iso} &= 2\partial_{\boldsymbol{C}^m}\Psi_{iso}^m : \partial_{\boldsymbol{C}}\boldsymbol{C}^m \\ \boldsymbol{S}_{iso} &= \xi\boldsymbol{S}_{iso}^m \\ \mathbb{C}_{iso} &= 4\partial_{\boldsymbol{C}}^2\Psi_{iso}^m = \partial_{\boldsymbol{C}}\boldsymbol{S}_{iso} = \partial_{\boldsymbol{C}^m}\xi\boldsymbol{S}_{iso}^m : \partial_{\boldsymbol{C}}\boldsymbol{C}^m \\ \mathbb{C}_{iso} &= \xi^2\mathbb{C}_{iso}^m \end{aligned} \tag{3.32}$$

where $\xi(\alpha, \theta) = \partial_{\mathbf{C}}\boldsymbol{C}^m$

46

The incremental parts for the isochoric response are summarized in (3.33):

$$\Delta \boldsymbol{S}_{iso}^m = \mathbb{C}_{iso}^m : \frac{1}{2}\Delta \boldsymbol{C}_{iso}^m$$

$$\boldsymbol{S}_{iso}^m = (\boldsymbol{S}_{iso}^m)_n + \Delta \boldsymbol{S}_{iso}^m$$

$$\boldsymbol{S}_{iso} = \xi \boldsymbol{S}_{iso}^m \tag{3.33}$$

$$\mathbb{C}_{iso} = \xi^2 \mathbb{C}_{iso}^m$$

We have finalized all necessary derivation for incremental formulation, at this point we derive the incremental part by combining volumetric and isochoric stress parts as shown in (3.34):

$$\Delta \boldsymbol{S}^m = \mathbb{C}^m : \frac{1}{2}\Delta \boldsymbol{C}^m$$

$$\boldsymbol{S}^m = (\boldsymbol{S}^m)_n + \Delta \boldsymbol{S}^m$$

$$\boldsymbol{S} = \xi \boldsymbol{S}^m \tag{3.34}$$

$$\mathbb{C} = \xi^2 \mathbb{C}^m$$

For the specific consistent mechanical tangent moduli of curing polymer:

$$
\begin{aligned}
\mathbb{C}_{vol}^m &= J_m(-2(\frac{\Lambda(\alpha)}{2}J_m - (\mu(\alpha) + \frac{\Lambda(\alpha)}{2})J_m^{-1})\mathbb{I}_{\boldsymbol{C}^{m-1}} \\
&\quad + [(\frac{\Lambda(\alpha)}{2} + (\mu(\alpha) + \frac{\Lambda(\alpha)}{2})J_m^{-2})J_m \\
&\quad + \frac{\Lambda(\alpha)}{2}J_m - (\mu(\alpha) + \frac{\Lambda(\alpha)}{2})J_m^{-1}]\boldsymbol{C}^{m-1} \otimes \boldsymbol{C}^{m-1}) \\
\mathbb{C}_{iso}^m &= \frac{2}{3}\mu(\alpha)J_m^{-2/3}[\frac{1}{3}\operatorname{tr}(\boldsymbol{C}^m)\boldsymbol{C}^{m-1} \otimes \boldsymbol{C}^{m-1} \\
&\quad - (\boldsymbol{1} \otimes \boldsymbol{C}^{m-1} + \boldsymbol{C}^{m-1} \otimes \boldsymbol{1}) + \operatorname{tr}(\boldsymbol{C}^m)\mathbb{I}_{\boldsymbol{C}^{m-1}}]
\end{aligned} \tag{3.35}
$$

We derive the stress and tangent moduli in Eulerian setting by using push-forward operation to satisfy the consistency with finite element formulation explained in Chapter 4.

Recalling that the Kirchhoff stress tensor $\boldsymbol{\tau}$ is the push forward of the second Piola-Kirchhoff stress tensor in (3.36) by using the relation $\boldsymbol{\tau} = \varphi_*(\boldsymbol{S}) = \boldsymbol{F}\boldsymbol{S}\boldsymbol{F}^T$ as depicted in Figure 3.4.
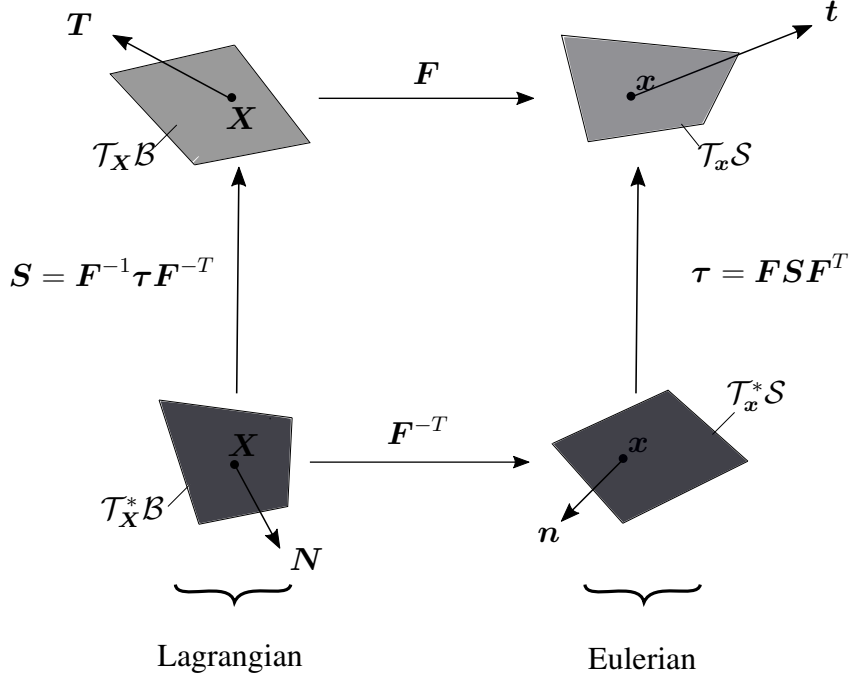
Figure 3.4: Geometric interpretation of the Lagrangian and Eulerian stress tensors on the commutative diagram

The push forward operation is applied on the volumetric stress response:

$$
\begin{aligned}
\boldsymbol{\tau}_{vol} = \boldsymbol{\varphi}_*(\boldsymbol{S}_{vol}) &= \boldsymbol{F}\boldsymbol{S}_{vol}\boldsymbol{F}^T \\
&= \boldsymbol{F}((\frac{\Lambda(\alpha)}{2} - (\mu(\alpha) + \frac{\Lambda(\alpha)}{2})J_m^{-1})J_m\boldsymbol{C}^{-1})\boldsymbol{F}^T \\
&= (\frac{\Lambda(\alpha)}{2} - (\mu(\alpha) + \frac{\Lambda(\alpha)}{2})J_m^{-1})J_m\boldsymbol{g}^{-1}
\end{aligned}
\tag{3.36}
$$

The push forward operation is applied on the isochoric stress response:

$$
\begin{aligned}
\boldsymbol{\tau}_{iso} = \boldsymbol{\varphi}_*(\boldsymbol{S}_{iso}) &= \boldsymbol{F}\boldsymbol{S}_{iso}\boldsymbol{F}^T \\
&= \boldsymbol{F}(2\frac{\mu(\alpha)}{2}J_m^{-2/3}[\mathbf{1} - \frac{1}{3}\operatorname{tr}(\boldsymbol{C})\boldsymbol{C}^{-1}])\boldsymbol{F}^T \\
&= \mu(\alpha)J_m^{-2/3}[\boldsymbol{b} - \frac{1}{3}\operatorname{tr}(\boldsymbol{b})\boldsymbol{g}^{-1}]
\end{aligned}
\tag{3.37}
$$

Starting from the definition of the material tangent moduli $\mathbb{C}$, given in (3.35) and incorporating the push forward operation, we obtain the relation between the Eulerian and Lagrangian moduli as shown in (3.38), (3.39) by separating volumetric and

isochoric, respectively. For volumetric tangent moduli:

$$
\begin{aligned}
\mathbb{c}_{vol} &= 2\partial_{\boldsymbol{g}}\boldsymbol{\tau}_{vol} \\
&= J_m[\frac{\Lambda(\alpha)}{2} + (\mu(\alpha) + \frac{\Lambda(\alpha)}{2})J_m^{-2} + \frac{\Lambda(\alpha)}{2}J_m \\
&\quad - (\mu(\alpha) + \frac{\Lambda(\alpha)}{2})J_m^{-1}]\boldsymbol{g}^{-1} \otimes \boldsymbol{g}^{-1} \\
&\quad - 2(\frac{\Lambda(\alpha)}{2}J_m - (\mu(\alpha) + \frac{\Lambda(\alpha)}{2})J_m^{-1})J_m\mathbb{I}_{\boldsymbol{g}^{-1}}
\end{aligned}
\tag{3.38}
$$

For isochoric tangent moduli:

$$
\begin{aligned}
\mathbb{c}_{iso} &= 2\partial_{\boldsymbol{g}}\boldsymbol{\tau}_{iso} \\
&= \frac{2}{3}\mu(\alpha)J_m^{-2/3}[\frac{1}{3}\,\mathrm{tr}(\boldsymbol{g})\boldsymbol{g}^{-1} \otimes \boldsymbol{g}^{-1} \\
&\quad - (\mathbf{1} \otimes \boldsymbol{g}^{-1} + \boldsymbol{g}^{-1} \otimes \mathbf{1}) + \mathrm{tr}(\boldsymbol{g})\mathbb{I}_{\boldsymbol{g}^{-1}}]
\end{aligned}
\tag{3.39}
$$

Table 3.1: Algorithmic Box: Elastic Response for the Chemo-Thermo-Mechanical
Coupled Problem

- Given database: History variables $\boldsymbol{C}_n$, θ_n, α_n, $\boldsymbol{S}_n^m$ and the current deformation
  gradient $\boldsymbol{F}_{n+1}$ and temperature θ_{n+1}

- Compute Jacobian
  J_θ and $J_\alpha \longrightarrow \xi(\alpha, \theta) = J_\theta^{-2/3} J_\alpha^{-2/3}$

- Compute Right Cauchy-Green Tensor
  $\boldsymbol{C} = \boldsymbol{F}^T \boldsymbol{F}$ and $\boldsymbol{C}^m = \xi \boldsymbol{C}$
  $\boldsymbol{C}_m^{-1}$ and $(\mathbb{I}_{\boldsymbol{C}_m^{-1}})_{ABCD} := \frac{1}{2}(C_{AC}^{m-1} C_{BD}^{m-1} + C_{AD}^{m-1} + C_{BC}^{m-1})$

- Compute material parameters with curing
  $\Lambda = \Lambda_f - (\Lambda_f - \Lambda_i) \tanh(\frac{\alpha_n - 0.04}{-T_f})$
  $\mu = \mu_f - (\mu_f - \mu_i) \exp(\frac{\alpha_n}{-T_f})$
  $\alpha_\theta = \alpha_{\theta f} - (\alpha_{\theta f} - \alpha_{\theta i}) \exp(\frac{\alpha_n}{-T_f})$
  $\xi_c = \xi_{cf} - (\xi_{cf} - \xi_{ci}) \exp(\frac{\alpha_n}{-T_f})$

- Compute moduli
  $\mathbb{C}_{vol}^m = J_m[\mathcal{P}'(J_m) + \mathcal{P}(J_m)]\boldsymbol{C}^{m-1} \otimes \boldsymbol{C}^{m-1} - 2\mathcal{P}(J_m)J_m \mathbb{I}_{\boldsymbol{C}^{m-1}}$
  $\mathbb{C}_{iso}^m = \frac{4}{3} s_1^m J_m^{-2/3}[\frac{1}{3} \operatorname{tr}(\boldsymbol{C}^m)\boldsymbol{C}^{m-1} \otimes \boldsymbol{C}^{m-1} - (\mathbf{1} \otimes \boldsymbol{C}^{m-1} + \boldsymbol{C}^{m-1} \otimes \mathbf{1}) +$
  $\operatorname{tr}(\boldsymbol{C}^m)\mathbb{I}_{\boldsymbol{C}^{m-1}}]$

- Compute increment
  $(\Delta \boldsymbol{C}^m)_{n+1} = (\boldsymbol{C}^m)_{n+1} - (\boldsymbol{C}^m)_n$
  $\Delta \boldsymbol{S}_{vol}^m = \mathbb{C}_{vol}^m : \frac{1}{2}\Delta \boldsymbol{C}^m$
  $\Delta \boldsymbol{S}_{iso}^m = \mathbb{C}_{iso}^m : \frac{1}{2}\Delta \boldsymbol{C}^m$

- Compute stress and modulus
  $\Delta \boldsymbol{S}^m = \mathbb{C}^m : \frac{1}{2}\Delta \boldsymbol{C}^m$
  $\boldsymbol{S}^m = (\boldsymbol{S}^m)_n + \Delta \boldsymbol{S}^m$
  $\boldsymbol{S} = \xi \boldsymbol{S}^m$
  $\mathbb{C} = \xi^2 \mathbb{C}^m$

- Update the history and push forward the stress and moduli.

CHAPTER 4

DISCRETIZATION AND FINITE ELEMENT IMPLEMENTATION OF COUPLED PROBLEM

In this section, we work on the weak forms of the governing differential equations with the help of their strong forms are tabulated in Table 2.1. We used the finite element and finite difference methods to discretize the body in space and time for the respective cases. The set of nonlinear equations that arise from discretization is solved by using the iterative Newton technique for the nodal degrees of freedom.

4.1 3-D Finite Element Formulation at Large Strain in Eulerian Setting

The balance of linear momentum equation and the transient heat conduction equation are solved numerically in this part of the thesis. The strong forms of the governing differential equations are multiplied with the corresponding square integrable test functions ($\delta\boldsymbol{\varphi}$ and $\delta\theta$) as shown in (4.2), (4.6) to derive the weak form of the equation set. The essential boundary conditions $\boldsymbol{\varphi} = \bar{\boldsymbol{\varphi}}$ on $\partial\mathcal{B}_{\varphi}$ and $\theta = \bar{\theta}$ on $\partial\mathcal{B}_{\theta}$ are satisifed by selecting the appropriate test functions. We set the weak forms of the coupled differential equations by using the Galerkin finite element method. All constructed equation sets are integrated over the body and are formed as in (4.1) for the mechanical, thermal problems, respectively.

$$
\begin{aligned}
G^{\varphi}(\delta\boldsymbol{\varphi};\boldsymbol{\varphi},\theta) \quad &= \quad G_{\text{int}}^{\varphi}(\delta\boldsymbol{\varphi};\boldsymbol{\varphi},\theta) \quad &- \quad G_{\text{ext}}^{\varphi}(\delta\boldsymbol{\varphi};\boldsymbol{\varphi},\theta) \quad &= 0 \\
G^{\theta}(\delta\theta;\boldsymbol{\varphi},\theta) \quad &= \quad G_{\text{int}}^{\theta}(\delta\theta;\boldsymbol{\varphi},\theta) \quad &- \quad G_{\text{ext}}^{\theta}(\delta\theta;\theta) \quad &= 0
\end{aligned}
\tag{4.1}
$$

The strong form of the balance of linear momentum equation multiplied by test function is given in (4.2).

$$
\int_{\mathcal{B}} -\delta\boldsymbol{\varphi}[J\operatorname{div}(J^{-1}\boldsymbol{\tau}) + \boldsymbol{B}]\,dV \quad \text{in} \quad \mathcal{B}
\tag{4.2}
$$

Then, we derive the Galerkin functional as in (4.3).

$$G^{\varphi}(\delta\boldsymbol{\varphi}; \boldsymbol{\varphi}, \theta) = \int_{\mathcal{B}} \delta\boldsymbol{\varphi}[J \operatorname{div}(\frac{\boldsymbol{\tau}}{J}) + \boldsymbol{B}]\, dV \quad \text{in} \quad \mathcal{B}$$

$$= -\int_{\mathcal{S}} \operatorname{div}(\delta\boldsymbol{\varphi}\boldsymbol{\sigma})\, dv + \int_{\mathcal{S}} \nabla_{\boldsymbol{x}}\delta\boldsymbol{\varphi} : \boldsymbol{\sigma}\, dv - \int_{\mathcal{B}} \delta\boldsymbol{\varphi} \cdot \boldsymbol{B}\, dV \qquad (4.3)$$

$$= -\int_{\partial\mathcal{S}} \delta\boldsymbol{\varphi}(\boldsymbol{\sigma}\boldsymbol{n})\, da + \int_{\mathcal{S}} \nabla_{\boldsymbol{x}}\delta\boldsymbol{\varphi} : \boldsymbol{\sigma}\, dv - \int_{\mathcal{B}} \delta\boldsymbol{\varphi} \cdot \boldsymbol{B}\, dV$$

The relation in (4.3) can be reexpressed as shown in (4.4).

$$G^{\varphi}(\delta\boldsymbol{\varphi}; \boldsymbol{\varphi}, \theta) = -\int_{\partial\mathcal{B}_{\varphi}} \delta\boldsymbol{\varphi} \cdot \boldsymbol{T}\, dA + \int_{\mathcal{B}} \nabla_{\boldsymbol{x}}\delta\boldsymbol{\varphi} : \boldsymbol{\tau}\, dV - \int_{\mathcal{B}} \delta\boldsymbol{\varphi} \cdot \boldsymbol{B}\, dV \qquad (4.4)$$

The Galerkin equation sets in (4.1) has been derived with help of (4.4).

$$G_{\text{int}}^{\varphi}(\delta\boldsymbol{\varphi}; \boldsymbol{\varphi}, \theta) = \int_{\mathcal{B}} \nabla_{\boldsymbol{x}}\delta\boldsymbol{\varphi} : \boldsymbol{\tau}\, dV$$

$$G_{\text{ext}}^{\varphi}(\delta\boldsymbol{\varphi}; \boldsymbol{\varphi}, \theta) = \int_{\partial\mathcal{B}_{\varphi}} \delta\boldsymbol{\varphi} \cdot \boldsymbol{T}\, dA + \int_{\mathcal{B}} \delta\boldsymbol{\varphi} \cdot \boldsymbol{B}\, dV \qquad (4.5)$$

Similarly, the strong form of the conservation of the energy equation in (2.101) is multiplied by the corresponding test function as expressed in (4.6).

$$\int_{\mathcal{B}} \delta\theta(\rho_0 c\dot{\theta} - \mathcal{H}_e - \mathcal{H}_c)\, dV \quad \text{in} \quad \mathcal{B} \qquad (4.6)$$

The Galerkin function is expressed as (4.7) for the chemo-thermal part.

$$G^{\theta}(\delta\theta; \boldsymbol{\varphi}, \theta) = \int_{\mathcal{B}} \delta\theta(\rho_0 c\dot{\theta} - \mathcal{H}_c - \mathcal{H}_e)\, dV \qquad (4.7)$$

The Galerkin functional for thermal part can also be writen explicitly as in (4.8).

$$G^{\theta}(\delta\theta; \boldsymbol{\varphi}, \theta) = \int_{\mathcal{B}} \delta\theta(\rho_0 c\dot{\theta} + \underbrace{J \operatorname{div}(J^{-1}\tilde{\boldsymbol{q}})}_{T1} - \mathcal{H}_c - \rho_0 r_b)\, dV \qquad (4.8)$$

where $\tilde{\boldsymbol{q}} := J\boldsymbol{q}$ and $J \operatorname{div}(\boldsymbol{q}) = \operatorname{DIV}(\boldsymbol{Q})$ as we know from (2.93).

We focus on the last term named as T1 in the right hand side of (4.8).

$$\int_{\mathcal{B}} \delta\theta J \operatorname{div}(J^{-1}\tilde{\boldsymbol{q}})\, dV = \int_{\mathcal{S}} \delta\theta \operatorname{div}(J^{-1}\tilde{\boldsymbol{q}})\, dv \qquad (4.9)$$

We apply the integration by parts to the relation in (4.9) and obtain,

$$\int_{\mathcal{S}} \delta\theta \operatorname{div}(J^{-1}\tilde{\boldsymbol{q}})\, dv = \int_{\mathcal{S}} (\operatorname{div}(\delta\theta J^{-1}\tilde{\boldsymbol{q}}) - \nabla\delta\theta J^{-1}\tilde{\boldsymbol{q}})\, dv$$

$$= \int_{\partial\mathcal{B}_h} \delta\theta\tilde{\boldsymbol{h}}_{\theta}\, dA - \int_{\mathcal{B}} \nabla\delta\theta \cdot \tilde{\boldsymbol{q}}\, dV \qquad (4.10)$$

52

Then, we put the relation in (4.10) into (4.8).

$$G^\theta(\delta\theta; \boldsymbol{\varphi}, \theta) = \int_{\mathcal{B}} \delta\theta(\rho_0 c\dot{\theta} - \mathcal{H}_c - \rho_0 r_b) - \nabla\delta\theta \cdot \tilde{\boldsymbol{q}}\, dV$$
$$+ \int_{\partial\mathcal{B}_h} \delta\theta\tilde{\boldsymbol{h}}_\theta\, dA$$

(4.11)

For $G^\theta(\delta\theta; \theta, \alpha)$ gets form :

$$G^\theta_{\text{int}}(\delta\theta; \boldsymbol{\varphi}, \theta) = \int_{\mathcal{B}} \delta\theta\rho_0 c\dot{\theta} - \nabla_{\boldsymbol{x}}\delta\theta \cdot \tilde{\boldsymbol{q}}\, dV$$
$$G^\theta_{\text{ext}}(\delta\theta; \theta) = \int_{\mathcal{B}} \delta\theta(\mathcal{H}_c + \rho_0 r_b)\, dV - \int_{\partial\mathcal{B}_h} \delta\theta\tilde{\boldsymbol{h}}_\theta\, dA$$

(4.12)

The relations in (4.5) and (4.12) obtained by Galerkin method are nonlinear functions of the field variables due to the gradient operators and non-linear constitutive models. Thus, we linearize these equation sets with respect to field variables to utilize the Newton-type iteration schemes within the implicit finite element framework.

$$\text{Lin}G^\varphi(\delta\boldsymbol{\varphi}, \boldsymbol{\varphi}, \theta)|_{\bar{\boldsymbol{\varphi}}, \bar{\theta}} \quad := G^\varphi(\delta\boldsymbol{\varphi}, \bar{\boldsymbol{\varphi}}, \bar{\theta}) \quad + \Delta G^\varphi(\delta\boldsymbol{\varphi}, \bar{\boldsymbol{\varphi}}, \bar{\theta}; \Delta\boldsymbol{\varphi}, \Delta\theta) \quad = \boldsymbol{0}$$
$$\text{Lin}G^\theta(\delta\theta, \boldsymbol{\varphi}, \theta)|_{\bar{\theta}} \quad := G^\theta(\delta\theta, \bar{\boldsymbol{\varphi}}, \bar{\theta}) \quad + \Delta G^\theta(\delta\theta, \bar{\boldsymbol{\varphi}}, \bar{\theta}; \Delta\boldsymbol{\varphi}, \Delta\theta) \quad = \boldsymbol{0}$$

(4.13)

The incremental terms obtained by the Gateaux derivative are expressed in the decomposed form in (4.14).

$$\Delta G^\varphi = \Delta G^\varphi_{\text{int}} - \Delta G^\varphi_{\text{ext}}$$
$$\Delta G^\theta = \Delta G^\theta_{\text{int}} - \Delta G^\theta_{\text{ext}}$$

(4.14)

Then, we define the incremental terms of the linearized Galerkin functional responsible for the mechanical part in (4.5) as shown in (4.15).

$$\Delta G^\varphi_{\text{int}}(\delta\boldsymbol{\varphi}, \Delta\boldsymbol{\varphi}, \boldsymbol{\varphi}, \theta) = \int_{\mathcal{B}} \Delta(\nabla_{\boldsymbol{x}}(\delta\boldsymbol{\varphi})) : \boldsymbol{\tau}\, dV + \int_{\mathcal{B}} \nabla_{\boldsymbol{x}}(\delta\boldsymbol{\varphi}) : \Delta\boldsymbol{\tau}\, dV$$

(4.15)

The incremental term $(\nabla_{\boldsymbol{x}}(\delta\boldsymbol{\varphi}))$ is derived as in (4.16).

$$\Delta(\nabla_{\boldsymbol{x}}(\delta\boldsymbol{\varphi})) = \Delta(\nabla_{\boldsymbol{X}}\delta\boldsymbol{\varphi}\boldsymbol{F}^{-1}) = \nabla_{\boldsymbol{x}}\delta\boldsymbol{\varphi}\Delta(\boldsymbol{F}^{-1})$$
$$= \nabla_{\boldsymbol{X}}\delta\boldsymbol{\varphi}(-\boldsymbol{F}^{-1}\Delta\boldsymbol{F}\boldsymbol{F}^{-1}) = -\nabla_{\boldsymbol{x}}\delta\boldsymbol{\varphi}\nabla_{\boldsymbol{x}}\Delta\boldsymbol{\varphi}$$

(4.16)

where $\nabla_{\boldsymbol{x}}\Delta\boldsymbol{\varphi} := \Delta\boldsymbol{F}\boldsymbol{F}^{-1}$.

The incremental stress term is derived as in (4.17).

$$\Delta\boldsymbol{\tau} = \mathcal{L}_{\Delta\boldsymbol{\varphi}}\boldsymbol{\tau} + \nabla_{\boldsymbol{x}}(\Delta\boldsymbol{\varphi})\boldsymbol{\tau} + \boldsymbol{\tau}(\nabla^T_{\boldsymbol{x}}\Delta\boldsymbol{\varphi}) + \boldsymbol{\mathcal{C}}^{\varphi\theta}\Delta\theta$$
$$= \mathbb{c} : \frac{1}{2}\mathcal{L}_{\Delta\boldsymbol{\varphi}}\boldsymbol{g} + \nabla_{\boldsymbol{x}}(\Delta\boldsymbol{\varphi})\boldsymbol{\tau} + \boldsymbol{\tau}(\nabla^T_{\boldsymbol{x}}\Delta\boldsymbol{\varphi}) + \boldsymbol{\mathcal{C}}^{\varphi\theta}\Delta\theta$$

(4.17)

where $\quad \mathbb{c} = 2\partial_{\boldsymbol{g}}\boldsymbol{\tau}, \quad \boldsymbol{C}^{\varphi\theta} = \partial_\theta\boldsymbol{\tau}, \quad \frac{1}{2}\mathcal{L}_{\Delta\boldsymbol{\varphi}}\boldsymbol{g} = \mathrm{sym}(\boldsymbol{g}\nabla_{\boldsymbol{x}}(\Delta\boldsymbol{\varphi}))$

Insertion of (4.16)-(4.17) into (4.18) yields the form:

$$
\begin{aligned}
\Delta G_{\mathrm{int}}^{\varphi}(\delta\boldsymbol{\varphi}, \boldsymbol{\varphi}, \theta) &= \int_{\mathcal{B}} -\nabla_{\boldsymbol{x}}(\delta\boldsymbol{\varphi})\nabla_{\boldsymbol{x}}(\Delta\boldsymbol{\varphi}) : \boldsymbol{\tau}\, dV \\
&+ \int_{\mathcal{B}} \nabla_{\boldsymbol{x}}(\delta\boldsymbol{\varphi})[\mathbb{C} : \nabla_{\boldsymbol{x}}(\Delta\boldsymbol{\varphi}) + \nabla_{\boldsymbol{x}}(\Delta\boldsymbol{\varphi})\boldsymbol{\tau} + \boldsymbol{\tau}\nabla_{\boldsymbol{x}}^T(\Delta\boldsymbol{\varphi})]\, dV \\
&= \underbrace{\int_{\mathcal{B}} \nabla_{\boldsymbol{x}}(\delta\boldsymbol{\varphi}) : \mathbb{C} : (g\nabla_{\boldsymbol{x}}(\Delta\boldsymbol{\varphi}))\, dV}_{\text{Material Part}} \\
&+ \underbrace{\int_{\mathcal{B}} \nabla_{\boldsymbol{x}}(\delta\boldsymbol{\varphi}) : (\nabla_{\boldsymbol{x}}(\Delta\boldsymbol{\varphi})\boldsymbol{\tau})\, dV}_{\text{Geometric Part}} \\
&+ \int_{\mathcal{B}} \nabla_{\boldsymbol{x}}(\delta\boldsymbol{\varphi}) : (\boldsymbol{C}^{\varphi\theta}\Delta\theta)\, dV
\end{aligned}
\tag{4.18}
$$

The external incremental term $\Delta G_{\mathrm{ext}}^{\varphi}$ is zero since neither the body force $\boldsymbol{B}$ nor the traction force acting on domain is deformation-dependent.

Then, we derive the incremental terms of the linearized Galerkin functional for the thermal part in (4.13) as shown in (4.19).

$$
\Delta G_{\mathrm{int}}^{\theta}(\delta\theta, \theta) = \int_{\mathcal{B}} \delta\theta\rho_0 c\frac{\Delta\theta}{\Delta t} - \Delta(\nabla_{\boldsymbol{x}}\delta\theta)\cdot\tilde{\boldsymbol{q}} - \nabla_{\boldsymbol{x}}\delta\theta\cdot\Delta\tilde{\boldsymbol{q}}
\tag{4.19}
$$

Similar to (4.16), the linearization of the $\nabla_{\boldsymbol{x}}(\delta\theta)$ leads to

$$
\Delta(\nabla_{\boldsymbol{x}}\delta\theta) = -\nabla_{\boldsymbol{x}}(\delta\theta)\nabla_{\boldsymbol{x}}(\Delta\boldsymbol{\varphi})
\tag{4.20}
$$

Then, we derive the incremental thermal flux terms in (4.19) based on the definiton of the spatial thermal flux.

$$
\Delta\tilde{\boldsymbol{q}} = \mathcal{L}_{\Delta\boldsymbol{\varphi}}\tilde{\boldsymbol{q}} + \nabla_{\boldsymbol{x}}(\Delta\boldsymbol{\varphi})\cdot\tilde{\boldsymbol{q}} + \tilde{\boldsymbol{K}}\cdot\nabla_{\boldsymbol{x}}(\Delta\theta)
\tag{4.21}
$$

where $\mathcal{L}_{\Delta\boldsymbol{\varphi}}$ is the Lie derivative of the potential heat flux.

$$
\mathcal{L}_{\Delta\boldsymbol{\varphi}}\tilde{\boldsymbol{q}} = \mathbb{C}^{\theta\varphi} : \frac{1}{2}\mathcal{L}_{\Delta\boldsymbol{\varphi}}\boldsymbol{g} = \mathbb{C}^{\theta\varphi} : (\boldsymbol{g}\nabla_{\boldsymbol{x}}(\Delta\boldsymbol{\varphi}))
\tag{4.22}
$$

We define the second-order conduction tensor which is also dependent on deformation and third-order mixed moduli as expressed in (4.23).

$$
\boldsymbol{K} := -\partial_{\nabla_{\boldsymbol{x}}\theta}\tilde{\boldsymbol{q}}, \quad \mathbb{C}^{\theta\varphi} := 2\partial_{\boldsymbol{g}}\tilde{\boldsymbol{q}}
\tag{4.23}
$$

54

Then, we put (4.20) and (4.21) into (4.19) and we obtain,

$$\Delta G^\theta_{\text{int}}(\delta\theta, \boldsymbol{\varphi}, \theta) = \int_\mathcal{B} \delta\theta \rho_0 c \frac{\Delta\theta}{\Delta t} + \nabla_{\boldsymbol{x}}(\delta\theta) \cdot \boldsymbol{K} \cdot \nabla_{\boldsymbol{x}}(\Delta\theta) \\ + \nabla_{\boldsymbol{x}}(\delta\theta) \cdot \mathbb{C}^{\theta\varphi} : (\boldsymbol{g}\nabla_{\boldsymbol{x}}(\Delta\boldsymbol{\varphi})) \, dV \tag{4.24}$$

Unlike the mechanical external Galerkin function increment G^φ_{ext}, the incremental external term in the linearized thermal Galerkin function depends on the field variables with external heat source term and chemical heating term. Then, we obtain

$$\Delta G^\theta_{\text{ext}}(\delta\theta; \theta) = \int_\mathcal{B} \delta\theta(\Delta\mathcal{H}_c + \Delta(\rho_0 r_b)) \, dV \tag{4.25}$$

with the increment of the chemical and thermal heating,

$$\Delta\mathcal{H}_c = \partial_\theta \mathcal{H}_c \Delta\theta \quad \text{and} \quad \Delta(\rho_0 r_b) = 0 \tag{4.26}$$

To this end, we discretize our domain $\mathcal{B}$ into element subdomain $\mathcal{B}^h_e$ in element level as shown in (4.27). Then, we applied the interpolation and and respective weight functions through the element domain with the discrete nodal values and shape functions.

$$\boldsymbol{\varphi}^h_e = \sum_{i=1}^n N^i \boldsymbol{d}^e_i$$
$$\theta^h_e = \sum_{i=1}^n N^i T^e_i$$
$$\delta\boldsymbol{\varphi}^h_e = \sum_{i=1}^n N^i \delta\boldsymbol{d}^e_i$$
$$\Delta\boldsymbol{\varphi}^h_e = \sum_{i=1}^n N^i \Delta\boldsymbol{d}^e_i$$
$$\delta\theta^h_e = \sum_{i=1}^n N^i \delta\phi^e_i \tag{4.27}$$
$$\nabla_{\boldsymbol{x}}\delta\boldsymbol{\varphi}^h_e = \sum_{i=1}^n \delta\boldsymbol{d}^e_i \otimes \nabla_{\boldsymbol{x}}N^i$$
$$\nabla_{\boldsymbol{x}}\Delta\boldsymbol{\varphi}^h_e = \sum_{i=1}^n \Delta\boldsymbol{d}^e_i \otimes \nabla_{\boldsymbol{x}}N^i$$
$$\nabla_{\boldsymbol{x}}\delta\theta^h_e = \sum_{i=1}^n \delta T^e_i \nabla_{\boldsymbol{x}}N^i$$
$$\nabla_{\boldsymbol{x}}\Delta\theta^h_e = \sum_{i=1}^n \Delta T^e_i \nabla_{\boldsymbol{x}}N^i$$

We derived the residual and consistent tangent expressions to conduct the Newton-type iterative algorithm as described in (4.28) and (4.29) in the staggered solution scheme. Thus, we omit the coupled terms before proceeding with the residual and

tangent expressions.

$$\boldsymbol{R}_I^{\varphi} = \underset{e=1}{\overset{n_{el}}{\mathbf{A}}} \Big\{ \int_{\mathcal{B}_e^h} \nabla_{\boldsymbol{x}} N^i \boldsymbol{\tau} \, dV - \int_{\mathcal{B}_e^h} N^i \boldsymbol{B} \, dV - \int_{\partial \mathcal{B}_t^e} N^i \boldsymbol{T} \, dA \Big\}$$

$$\boldsymbol{R}_J^{\theta} = \underset{e=1}{\overset{n_{el}}{\mathbf{A}}} \Big\{ \int_{\mathcal{B}_e^h} N^j \rho_0 c \frac{\Delta \theta}{\Delta t} \, dV - \int_{\mathcal{B}_e^h} \nabla_{\boldsymbol{x}} N^j . \tilde{\boldsymbol{q}} \, dV - \int_{\mathcal{B}_e^h} N^j (f_{\theta} + \mathcal{H}_c) \, dV \Big\}$$

(4.28)

Similarly, we construct the tangent matrices coming from the linearization of the residual vectors in (4.29).

$$\mathcal{K}_{IJ-mat}^{\varphi\varphi} = \underset{e=1}{\overset{n_{el}}{\mathbf{A}}} \Big\{ \int_{\partial \mathcal{B}_t^e} \nabla_{\boldsymbol{x}} N^i \cdot \mathbb{C}^{\varphi\varphi} \cdot \nabla_{\boldsymbol{x}} N^j \, dV \Big\}$$

$$\mathcal{K}_{IJ-geo}^{\varphi\varphi} = \underset{e=1}{\overset{n_{el}}{\mathbf{A}}} \Big\{ \{ \int_{\partial \mathcal{B}_t^e} \nabla_{\boldsymbol{x}} N^i \cdot (\nabla_{\boldsymbol{x}} N^j \boldsymbol{\tau}) \, dV \Big\}$$

$$\mathcal{K}_{IJ}^{\theta\theta} = \underset{e=1}{\overset{n_{el}}{\mathbf{A}}} \Big\{ \int_{\mathcal{B}_\theta^e} \nabla_{\boldsymbol{x}} N^i \frac{\partial \tilde{\boldsymbol{q}}}{\partial \nabla_{\boldsymbol{x}} \theta} \nabla_{\boldsymbol{x}} N^j \, dV - \int_{\mathcal{B}_\theta^e} N^i \frac{\rho_0 c}{dt} N^j \, dV$$

(4.29)

$$- \int_{\mathcal{B}_\theta^e} N^i (\partial_\theta \mathcal{H}_c) N^i \, dV \Big\}$$

In the staggered solution scheme approach, the values of the temperature values are taken from the previous time step for the solution of the displacement field as depicted in Figure 4.1. Then, the solution algorithm is conducted one by one.
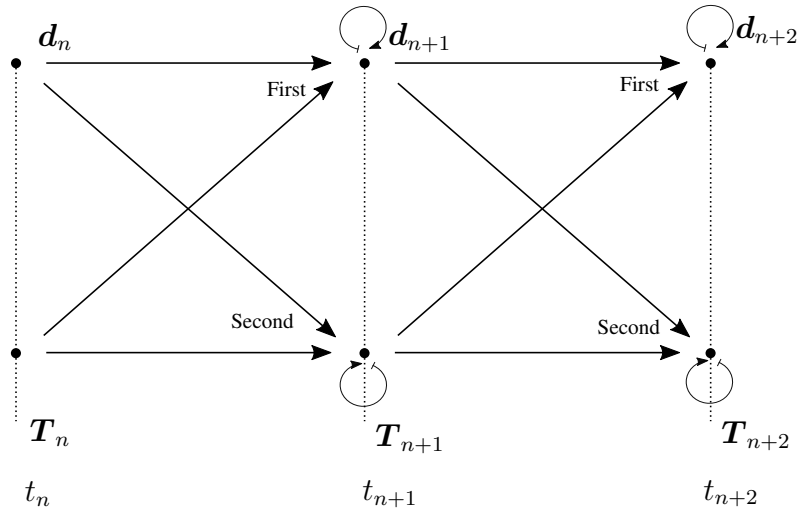
Figure 4.1: The illustration of the staggered solution methodology

Therefore, the coupled terms are set to zero as shown in (4.30).

$$\mathcal{K}^{\varphi\theta} = \mathbf{0}, \quad \mathcal{K}^{\theta\varphi} = \mathbf{0} \tag{4.30}$$

Then, after constructed residual and consistent tangent moduli, we solve linear algebra problem by using the Newton-Raphson iteration scheme.

$$\begin{aligned}
\boldsymbol{D} &= \overline{\boldsymbol{D}} - \mathcal{K}^{\varphi\varphi-1} \cdot \boldsymbol{R}^{\varphi} \\
\boldsymbol{T} &= \overline{\boldsymbol{T}} - \mathcal{K}^{\theta\theta-1} \cdot \boldsymbol{R}^{\theta}
\end{aligned} \tag{4.31}$$

CHAPTER 5

NUMERICAL EXAMPLES

In this chapter, we illustrate representative numerical examples regarding the chemical, thermal and mechanical properties of frontally polymerized material under different chemical and thermal conditions. We start to verify our approach by performing spatial and temporal convergence analyses in Section 5.1. Then, the planar and non-planar examples are illustrated under different chemo-thermal conditions. Pojman and coworkers [11] have examined composite systems created using metal strips which are benchmark examples in the literature. In these studies, they examine how the front speed changes with the system size and the effects of a metal strip on front velocity, shape and width. However, the studies in the literature are not limited to the effect of a metal strip, carbon fibers are also used in the experimental analysis. Thus, we investigate the polymerization front, rate and behavior of the chemical and thermal coupled problems with carbon fiber and without carbon fiber. In addition, numerical examples similar to Sottos and coworkers's paper [1, 3] are conducted for the optimum amount of carbon fiber.

We exemplify the thermodynamic model we have developed with the problem in Geubelle's studies [3] and validate our model with spatial and temporal convergence studies. Then, we study four different examples which are planar front examples, non-planar front examples, planar examples with two sides heating and chemo-thermo-mechanical examples.

The main aim of the example in Section 5.2.1 is description of the planar front propagation, chemical heating and the degree of polymerization. We present the result of the temperature and the degree of curing profile and also 2D model view.

59

The example in Section 5.2.2 is about the evolution of the fiber reinforced composite where we examine how the front and polymerization change with different amounts of fiber. We show that there should be an optimum fiber ratio for polymerization by examining our results as in Geubelle and coworkers' study [3].

The example in Section 5.2.3 is the planar frontal polymerization with the heating on two opposite sides. The main motivation for this study is to investigate how the polymerization and frontal characteristics would change in this case and how much the polymerization time would decrease.

The examples in Section 5.3 are devoted to chemo-thermo-mechanical boundary-value problems. We propose a new, incremental finite elasticity coupled with the chemo-thermal fields and material properties evolution with the degree of curing for the first time so it is the main section of our thesis. We observe how the mechanical and thermal properties of the frontally polymerized material change by examining our results. Moreover, we examine evolution of the stress accumluations that may lead to a strength loss in the final product. We also investigate the expansion and contraction of the material frontally polymerized.

For the model problem, we apply the thermal heating on a certain side of the domain during the trigger period. During heating, the other sides of the domain are insulated, i.e. in the flux-free state. Once the heating is completed, the heated side is also insulated. We use computational models based on the results obtained from the convergence studies described in Section 5.1. Moreover, the chemo-thermal coupled problem is solved with help of the staggered scheme approach. To make it clear, the temperature values calculated in the previous step are used to the chemical heating part in solution of the chemo-thermal coupled problem. The solution time of the problem is significantly reduced thanks to this technique. For the chemo-thermo-mechanical model problem, we also use identical thermal and chemical conditions with the chemo-thermal problem. Besides using the staggered approach in the chemo-thermal part, we also use the same approach in the solution of the chemo-thermal-mechanical problem. In this approach, we use the temperature nodal values from the previous time step in the solution of the mechanical problem. Thus, we can increase the computational efficiency within acceptable tolerance limits.

5.1 Convergence Analysis

In this section, we examine the effect of the spatial and temporal discretization we have used in our model on the convergence of solution. Thus, we have conducted the spatial and temporal discretization convergence analysis to determine the optimum values by using FEAP© v8.5 FEM solver [34]. For the chemo-thermal model problem, we choose a square domain with the dimensions 7.5 mm × 7.5 mm as in Geubelle and coworkers' study [3] and as shown in Figure 5.1.
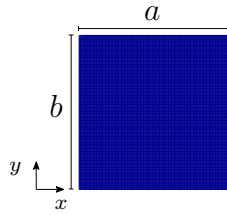
Figure 5.1: The domain size for the 2D model problem. $a = 7.5$ mm, $b = 7.5$ mm

We summarize the initial and boundary conditions of the chemo-thermal problem in (5.1).

$$
\begin{aligned}
\theta(x, y, 0) &= 293 \text{ K}, \\
\alpha(x, y, 0) &= 0.05, \\
\theta(0, y, t) &= 453 \text{ K} \qquad \text{for} \quad 0 \leq t \leq t_{trig}, \\
\nabla\theta|_{(0,y,t)} &= 0 \qquad\qquad \text{for} \quad t > t_{trig}, \\
\nabla\theta|_{(x,0,t)} &= 0 \qquad\qquad \text{for} \quad t \geq 0, \\
\nabla\theta|_{(7.5,y,t)} &= 0 \qquad\qquad \text{for} \quad t \geq 0, \\
\nabla\theta|_{(x,7.5,t)} &= 0 \qquad\qquad \text{for} \quad t \geq 0.
\end{aligned}
\tag{5.1}
$$

We also tabulate the material properties that we use in the following examples in Table 5.1:

Table 5.1: The summary of the chemo-thermal material properties used in simulations

Material	Parameters	Unit	Definition	Value
Carbon Fiber	κ	$[\frac{W}{m \cdot K}]$	Thermal conductivity	9.30×10^0
	ρ	$[\frac{kg}{m^3}]$	Density	18.00×10^2
	C_p	$[\frac{J}{kg \cdot K}]$	Specific heat	75.36×10^1
PSU Foam	κ	$[\frac{W}{m \cdot K}]$	Thermal conductivity	2.20×10^{-2}
	ρ	$[\frac{kg}{m^3}]$	Density	32.50×10^0
	C_p	$[\frac{J}{kg \cdot K}]$	Specific heat	14.53×10^2
Monomer (DPCD)	κ	$[\frac{W}{m \cdot K}]$	Thermal conductivity	1.50×10^{-1}
	ρ	$[\frac{kg}{m^3}]$	Density	98.00×10^1
	C_p	$[\frac{J}{kg \cdot K}]$	Specific heat	16.00×10^2
	A	$[\frac{1}{s}]$	Pre-exponential factor	8.22×10^{15}
	E	$[\frac{kJ}{mol}]$	Activation energy	11.07×10^1
	H_r	$[\frac{J}{g}]$	Total enthalpy of reaction	35.00×10^1
	n	$[-]$	Orders of reaction	1.72×10^0
	m	$[-]$	Orders of reaction	7.70×10^{-1}
	C	$[-]$	Diffusion constant	14.48×10^0
	α_c	$[-]$	Diffusion constant	4.10×10^{-1}
	R	$[\frac{J}{mol \cdot K}]$	Universal gas constant	83.14×10^{-1}

5.1.1 Spatial Discretization Convergence Analysis

The sharp gradient in the temperature profile with the advancing front complicates the solution of the problem and requires a minimum mesh size in moving front of the polymerization. Moreover, the size of meshes affects the approximation quality and precision of the finite element approach. Also, we used the time-discretization adaptivity tool of FEAP$^©$ in the spatial convergence analysis so the maximum time step of $\Delta t = 10^{-3}$ s and minimum time step of $\Delta t = 10^{-5}$ s.

We discretize our model domain into 50, 100, 230, and 300 4-node quadrilateral elements in each direction. In other words, we have specified four different element sizes, $h = 0.15$ mm, $h = 0.075$ mm, $h = 0.033$ mm, and $h = 0.025$ mm. In turn, we have examined their convergence status by using these mesh sizes.
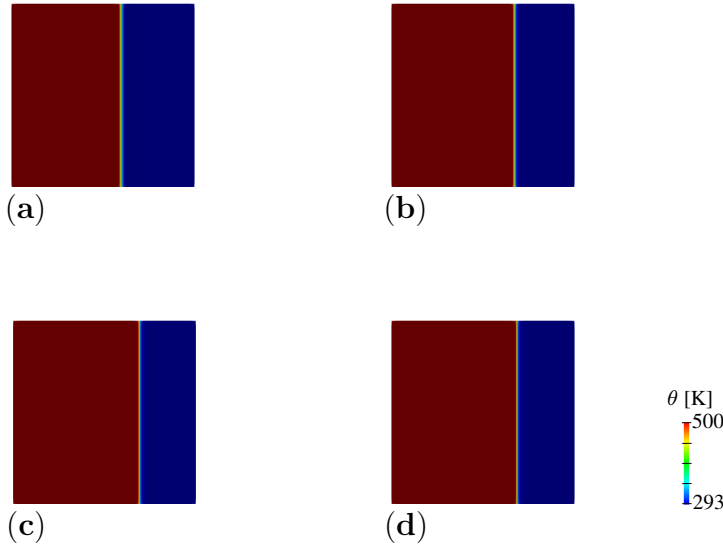
Figure 5.2: The spatial convergence analyzes of the 2D model domain. a) $h = 0.15$ mm, b) $h = 0.075$ mm, c) $h = 0.033$ mm, d) $h = 0.025$ mm at $t = 3.5$ s

The temperature results of the analyses for the mesh sizes of $h = 0.15$ mm, $h = 0.075$ mm, $h = 0.033$ mm and $h = 0.025$ mm are presented in Figure 5.2.
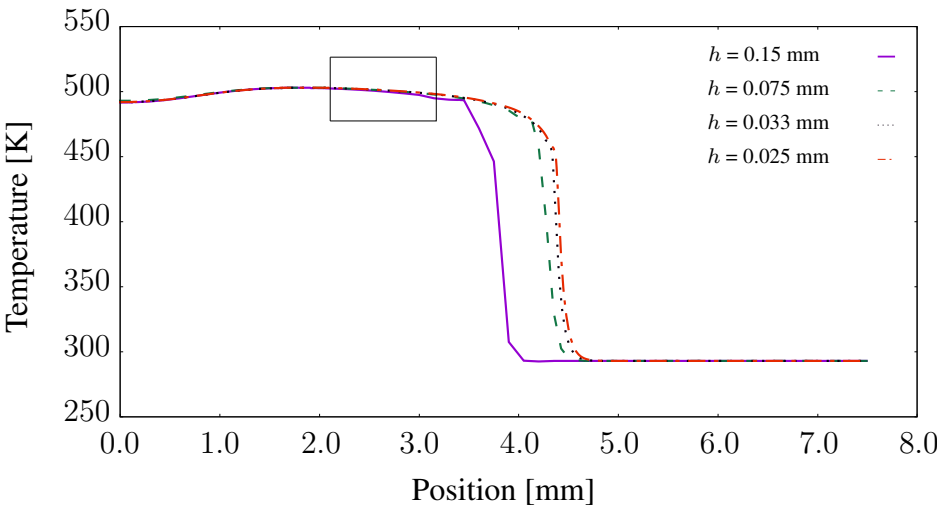
Figure 5.3: The spatial convergence analyses of the 2D model domain

63

In these examples, heating is applied from the left side of the domain up to 453 K as shown in Figure 5.9 during t_{trig} = 1 s. Afterwards, the heat source is removed and this side is isolated. We observe that for the coarser mesh sizes front move slower and diverge from the general convergence trend. We also present our results for the analyzes of four different mesh sizes which are h = 0.15 mm, h = 0.075 mm, h = 0.033 mm and h = 0.025 mm graphically in Figure 5.3.

We observe that the spatial discretization converges when the element size is decreased. Thus, we get closer by fitting the position between x = 2.2 mm and x = 3 mm in Figure 5.3 to examine the results better. The result is presented in Figure 5.4:
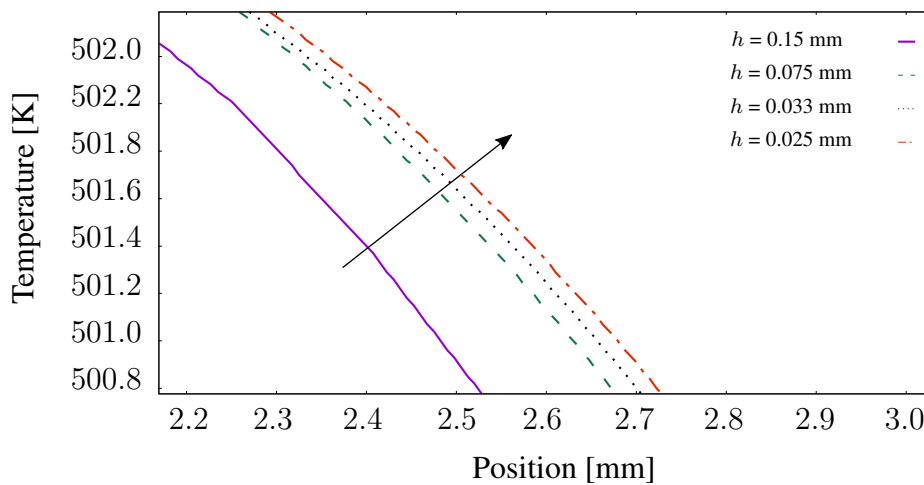
Figure 5.4: Close up view for position fitting between x = 2.2 mm and x = 3 mm, (Arrow direction shows convergent behavior)

It can be seen that the results are close to each other in the direction indicated by the arrow in Figure 5.4. Thus, the direction of the arrow denotes better convergence performance of the corresponding mesh size.

According to the results presented in Figure 5.4, we observe that the convergence performance improves as the mesh size gets smaller. The reducing the size after a certain point does not have much effect on the precision of the solution, but it increases the cost of the computation and reduces the efficiency. Thus, we have performed the spatial convergence analysis to choose an optimal size. Especially, there is no significant convergence performance difference between mesh sizes h = 0.033 mm and h = 0.025

mm as seen from the graph in Figure 5.4. However, we know that the $h = 0.033$ mm mesh size deviates from the reference solution (solution corresponding to h = 0.025 mm), but we observe that the results are within the acceptable error tolerance limits. As a result, we use the value of $h = 0.033$ mm as the mesh size in the following 2D analyses.

Especially in the composite study in the non-planar examples discussed in detail in Section 5.2.2, we find that the front shape is affected by the mesh size a lot. We realize that the numerical results deviated from the experimental studies. Moreover, we observe stair-like patterns in the front shape in coarser meshes as shown in Figure 5.5. This phenomenon shows the another importance of the spatial discretization convergence analysis.

(a)   (b)
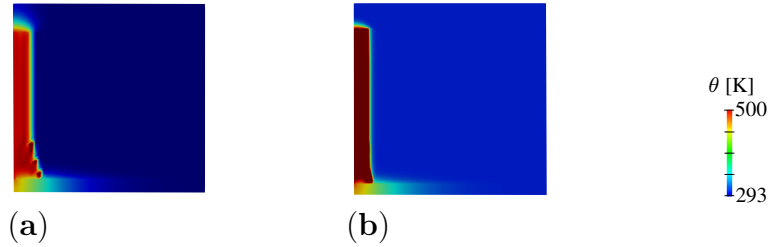
Figure 5.5: The mesh size analysis of the 2D model domain. a) $h = 0.15$ mm, b) $h = 0.033$ mm at $t = 0.5$ s.

5.1.2 Temporal Convergence Analysis

Similar to the spatial convergence analysis, the temporal convergence also affects the computation performance of our thermodynamical model. We conduct the temporal convergence analysis for the four different time steps of $\Delta t = 4 \times 10^{-3}$ s, $\Delta t = 10^{-3}$ s, $\Delta t = 5 \times 10^{-4}$ s, $\Delta t = 10^{-4}$ s to calibrate the time step required to overcome this sharp gradient and stiff problem.

We have used the adaptive time-step module of FEAP$^{\copyright}$ to increase the computation speed. In the time adaptive module, we used the the maximum time step of $\Delta t_{\max} = 4 \times 10^{-3}$ s, $\Delta t_{\max} = 10^{-3}$ s, $\Delta t_{\max} = 5 \times 10^{-4}$ s, $\Delta t_{\max} = 10^{-4}$ s, respectively and minimum time step is taken as $\Delta t_{\min} = 10^{-5}$ s. In turn, the finite element analyses are conducted for different time steps. We present the results of the analyses in Figure

5.6.

As it can be seen from the contour plots in Figure 5.6, the larger time increments result in a polymerization front that moves faster and diverges from the general convergence trend.
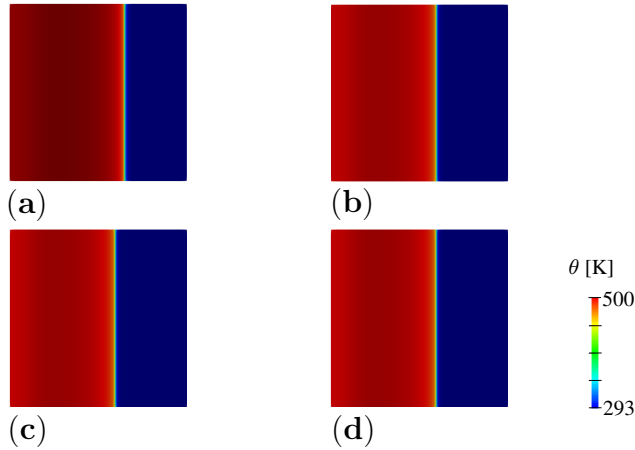
Figure 5.6: The temporal discretization convergence performance for a) $\Delta t = 4 \times 10^{-3}$ s, b) $\Delta t = 10^{-3}$ s, c) $\Delta t = 5 \times 10^{-4}$ s, d) $\Delta t = 10^{-4}$ s at $t = 3.5$ s,

We observe that temporal discretization converges when the time step is decreased. Thus, we get closer by fitting the position between $x = 3.7$ mm and $x = 4.4$ mm in Figure 5.7 to examine the results better as shown in Figure 5.8: It can be seen that
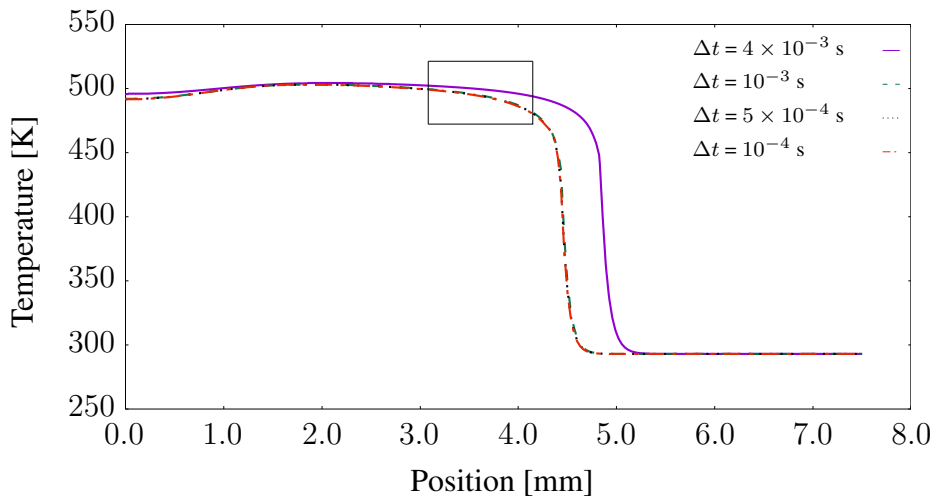
Figure 5.7: The temporal discretization convergence performance for a) $\Delta t = 4 \times 10^{-3}$ s, b) $\Delta t = 10^{-3}$ s, c) $\Delta t = 5 \times 10^{-4}$ s, d) $\Delta t = 10^{-4}$ s at $t = 3.5$ s,

the results are close to each other in the direction indicated by the arrow in Figure 5.8. Therefore, the direction of the arrow represents a better convergence performance for the corresponding time steps.
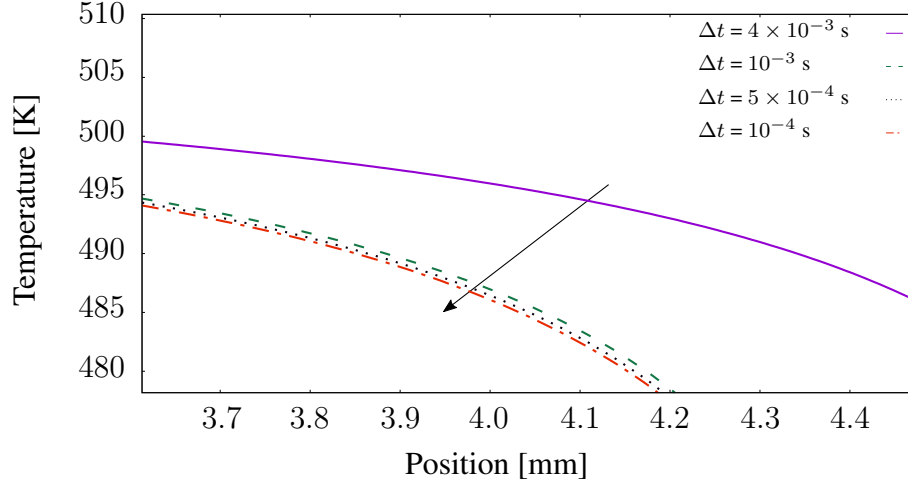
Figure 5.8: The temporal discretization convergence performance for a) $\Delta t = 4 \times 10^{-3}$ s, b) $\Delta t = 10^{-3}$ s, c) $\Delta t = 5 \times 10^{-4}$ s, d) $\Delta t = 10^{-4}$ s at $t = 3.5$ s, (Arrow direction shows convergent behavior)

The results of the temporal convergence analysis indicate that $\Delta t = 10^{-3}$ s is a reasonable time step as shown the results in Figure 5.8. Thus, we used time step of $\Delta t = 10^{-3}$ s in the subsequent simulations.

5.2 Chemo-Thermal Numerical Examples

In this section, the chemo-thermal analyses are conducted to examine the characteristics of the front, polymerization and temperature variation. We investigate three examples, namely the planar front, the non-planar front, and the planar front heating on two opposite sides. We use the material properties in Table 5.1 in the following examples:

5.2.1 Planar Front

In this example, the problem is very stiff and highly nonlinear due to the sharp gradients of temperature and the degree of curing in the vicinity of the front. We apply the thermal heating on the left side of the domain for $t = t_{trig} = 1$ s as depicted in Figure 5.9. Then, we investigate the chemical and thermal evolution in the material. The domain size is 7.5 mm x 7.5 mm and we used 4-node quadrilateral elements of size $h = 0.033$ mm. The time increment $\Delta t = 10^{-3}$ s is used in the simulation.
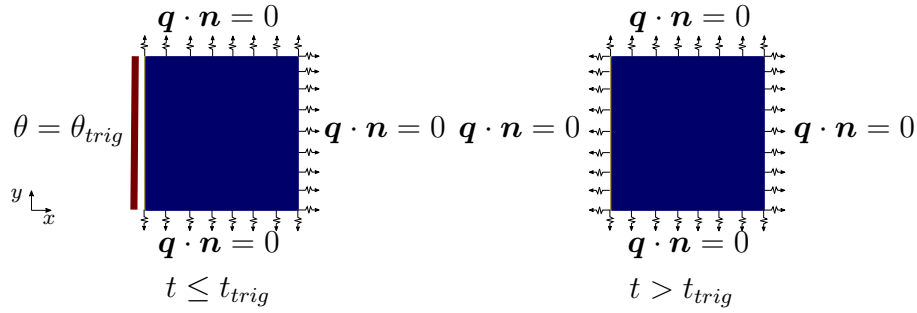
Figure 5.9: Boundary condition for the 2D model problem

We summarize the initial and boundary conditions in (5.2).

$$
\begin{aligned}
\theta(x, y, 0) &= 293 \text{ K}, \\
\alpha(x, y, 0) &= 0.05, \\
\theta(0, y, t) &= 453 \text{ K} \qquad \text{for} \quad 0 \leq t \leq t_{trig}, \\
\nabla\theta|_{(0,y,t)} &= 0 \qquad\qquad \text{for} \quad t > t_{trig}, \\
\nabla\theta|_{(x,0,t)} &= 0 \qquad\qquad \text{for} \quad t \geq 0, \\
\nabla\theta|_{(7.5,y,t)} &= 0 \qquad\qquad \text{for} \quad t \geq 0, \\
\nabla\theta|_{(x,7.5,t)} &= 0 \qquad\qquad \text{for} \quad t \geq 0.
\end{aligned}
\tag{5.2}
$$

We present the temperature distribution in Figure 5.10 at different times of frontal polymerization.

68
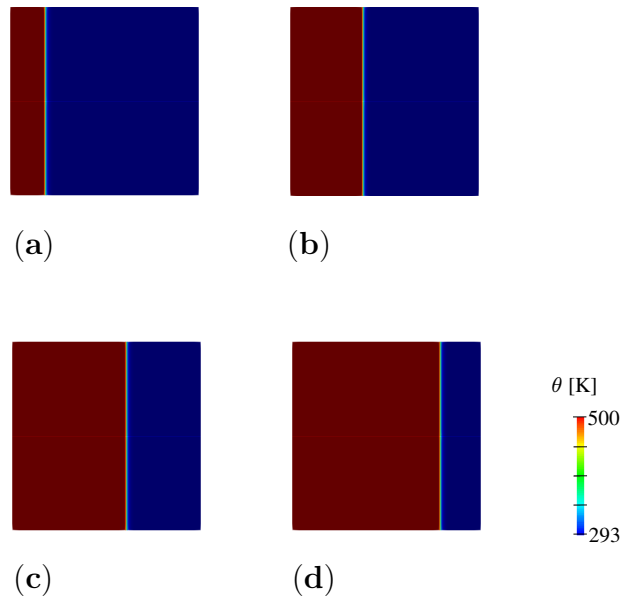
Figure 5.10: The temperature distribution at, a) $t = 1$ s, b) $t = 2$ s, c) $t = 3$ s, d) $t = 4$ s

The comparison between our numerical simulations and the results of the experiment conducted by Sottos and coworkers [3], indicates that we have obtained qualitatively similar results as shown in Figure 5.11.
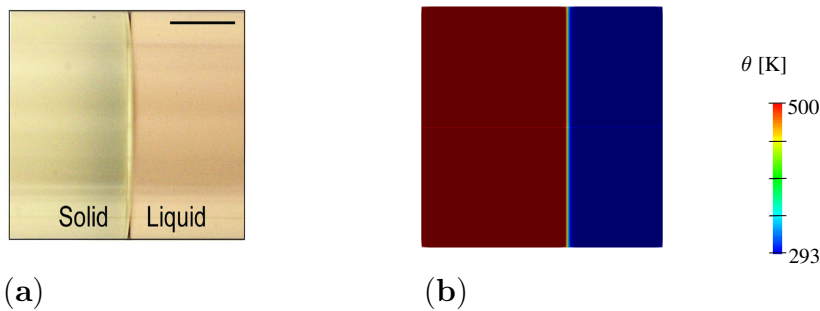
Figure 5.11: The comparison between the experimental result [3] and numerical result

We present the temperature and the degree of curing curves corresponding to the simulations given in Figure 5.10 in Figure 5.12. According to our analyses, we observe that temperature variation is between about 500 K and 293 K.
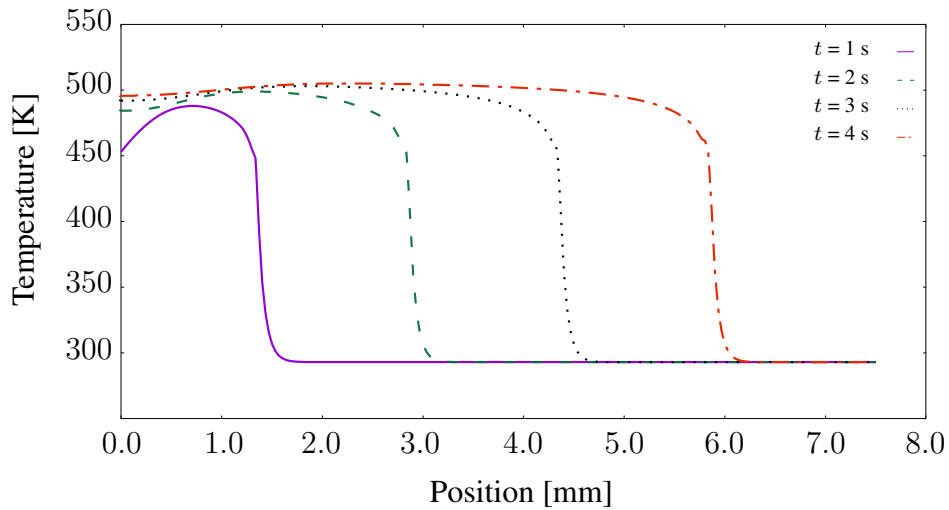
Figure 5.12: The temperature variation with respect to position

The degree of curing variation with respect to position is presented in Figure 5.13. As seen in Figure 5.12 and Figure 5.13, the temperature and the degree of curing have a similar propagation trend with respect to position.
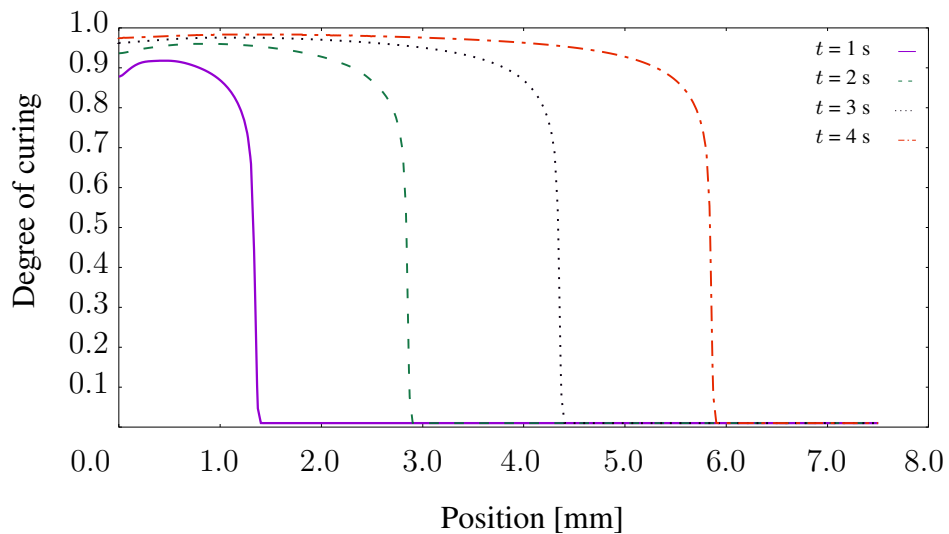
Figure 5.13: The evolution of the degree of curing with respect to position

5.2.2   Non-Planar Front in Composites

In this example, we investigate the behavior of the fiber reinforced polymer composite which is frontally polymerized. Similar to planar front examples, the problem is also

very stiff and highly nonlinear due to the sharp gradient temperature and the degree of curing in the vicinity of the front. The thermal conduction property of the fiber is greater than that of the monomer, so the fiber is used in the frontal polymerization process to increase the propagation of the polymerization front. Therefore, we investigate the effect of carbon fiber and the amount of carbon fiber on the shape and speed of the front for the frontal polymerization process quantitatively.
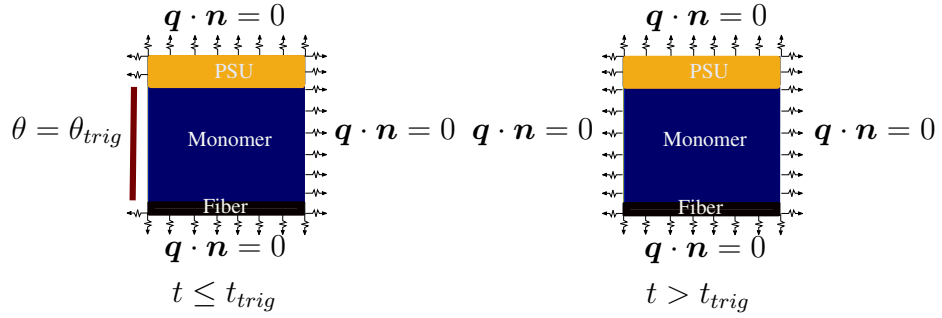
Figure 5.14: Boundary condition for the 2D model problem

We applied the thermal heating on the left side of the domain for $t \leq t_{trig} = 1$ s as depicted in Figure 5.14. The polymerization is initiated when the heat source contact with monomer and it does not contact with the fiber. Then, we investigate the chemical and thermal evolution in the material. The domain size is 7.5 mm $\times$ 7.5 mm and we use 4-node quadrilateral elements of mesh size of $h = 0.033$ mm. The time increment $\Delta t = 10^{-3}$ s is used in the simulation. We consider the four different amounts of fiber which are 0.25 mm $\times$ 7.5 mm, 0.50mm $\times$ 7.5 mm, 0.75 mm $\times$ 7.5 mm and 1.0 mm $\times$ 7.5 mm in our simulations.

Table 5.2: The summary of the thickness variation in composite samples

Simulation	a	b	c	d	f
1	7.50 mm	7.50 mm	1.00 mm	6.25 mm	0.25 mm
2	7.50 mm	7.50 mm	1.00 mm	6.00 mm	0.50 mm
3	7.50 mm	7.50 mm	1.00 mm	5.75 mm	0.75 mm
4	7.50 mm	7.50 mm	1.00 mm	5.50 mm	1.00 mm

We tabulate the dimensions of the components in Table 5.2 where a and b denotes

for domain size, c, d and f represents thickness of the glass, monomer, and fiber, respectively and as depicted in Figure 5.15.
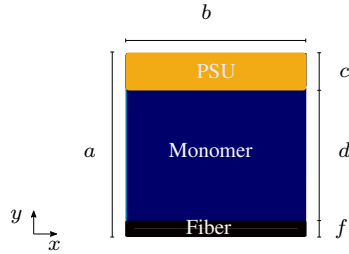
Figure 5.15: Dimension of the 2-D geometry forthe composite model problem

We summarize the initial and boundary conditions in (5.3).

$$
\begin{aligned}
\theta(x, y, 0) &= 293 \text{ K}, \\
\alpha(x, y, 0) &= 0.05, \\
\theta(0, y, t) &= 453 \text{ K} \quad \text{for} \quad 0 \leq t \leq t_{trig} \quad \text{where} \quad y = [f, f + d], \\
\nabla\theta|_{(0,y,t)} &= 0 \quad \text{for} \quad t > t_{trig}, \\
\nabla\theta|_{(x,0,t)} &= 0 \quad \text{for} \quad t \geq 0, \\
\nabla\theta|_{(7.5,y,t)} &= 0 \quad \text{for} \quad t \geq 0, \\
\nabla\theta|_{(x,7.5,t)} &= 0 \quad \text{for} \quad t \geq 0.
\end{aligned}
\tag{5.3}
$$

The contour plots in Figure 5.16 show the temperature distribution according to the fiber ratio which increase from top to bottom. The contour plots are placed from left to right according to the progression of time. It can be seen that the temperature diffusion accelerates in proportion to the fiber ratio. The distinct change from flat to the conical front shape is observed at $t = 4$ s in Figure 5.16. This is consistent with the experiment results in [1].
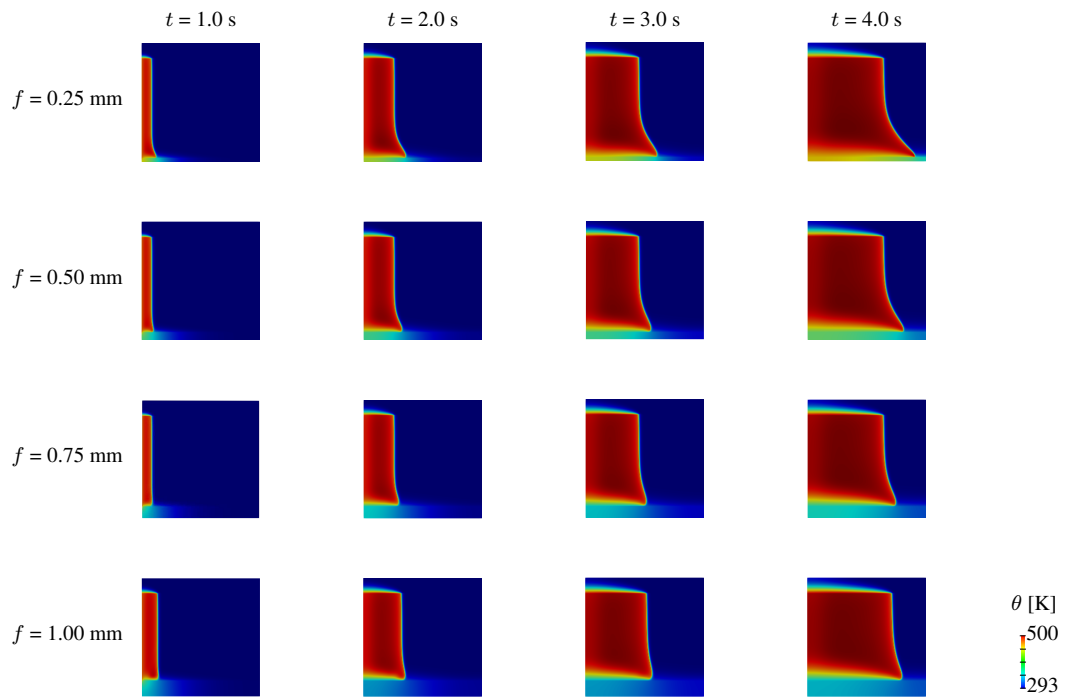
Figure 5.16: Temperature variation in the composite with distinct fiber fractions and at different times

When we compare our numerical simulations with the experiment conducted by Sottos and coworkers [3], we observed that we have obtained qualitatively compatible results as shown in Figure 5.17. Because of the symmetry, we have modeled only half of the experimental sample in our analysis.

(a) (b)
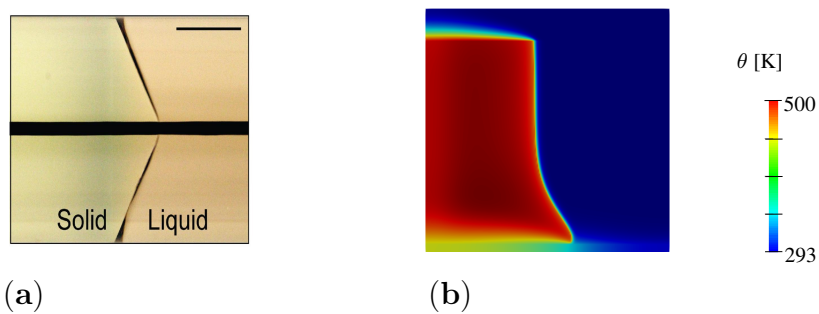
Figure 5.17: The comparison between the experimental result [3] and numerical result

We have extracted sections from 0.25 mm above the fiber for the temperature and the degree of curing simulation in Figures 5.18 and 5.19.
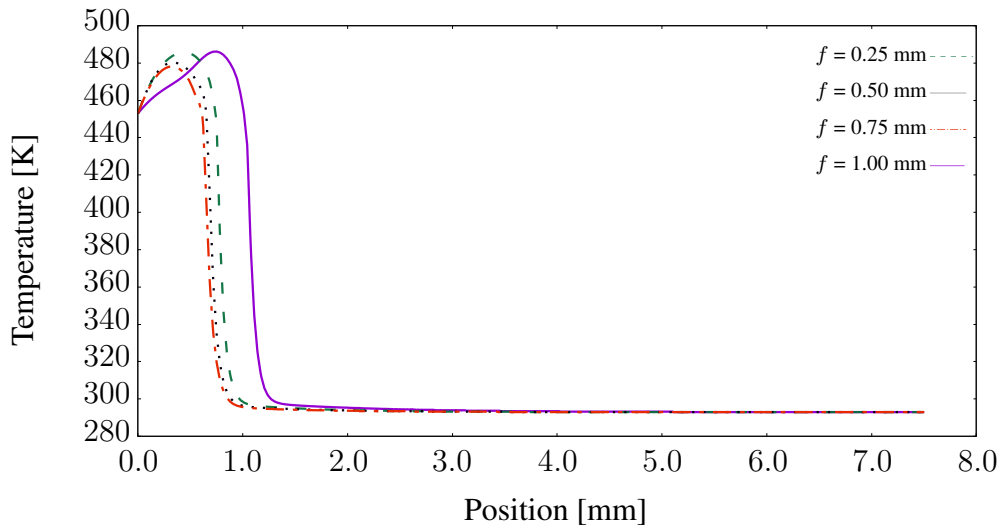
Figure 5.18: Temperature variation in the composite at $t = 1$ s, where f represents the fiber thickness.

According to result in Figure 5.18, we observe that the temperature diffusion is faster in resin that has a higher fiber ratio at $t = 1$ s compared with the other composites.
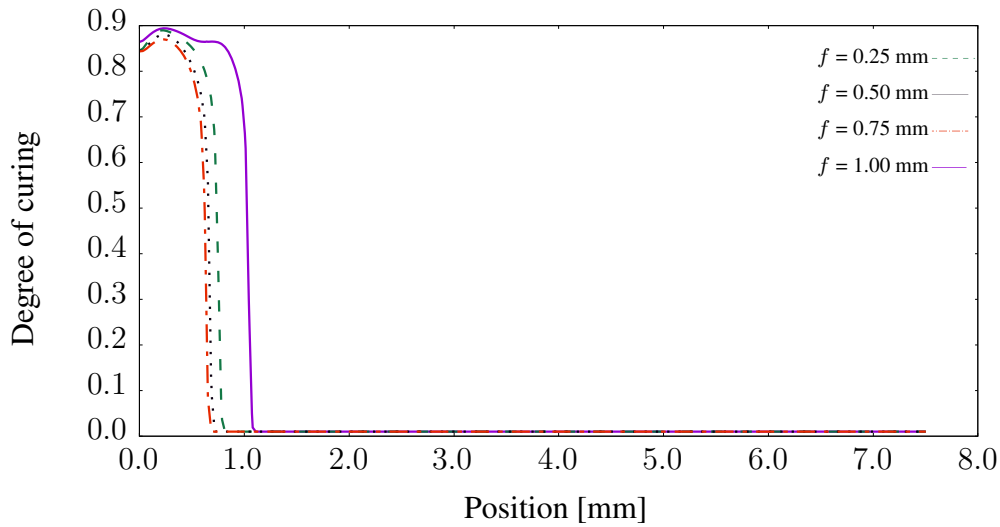
Figure 5.19: The evolution of the degree of curing at $t = 1$ s, where f represents the fiber thickness.

Similarly, it can be seen that the curing propagation is also higher in the resin that has a higher fiber ratio at $t = 1$ s as shown in Figure 5.19. .
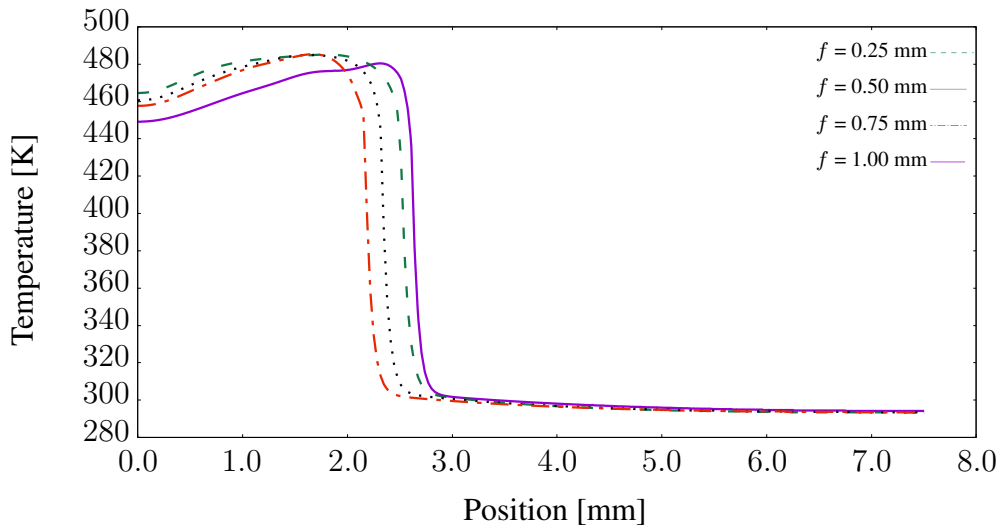
Figure 5.20: Temperature variation in the composite at $t = 2$ s, where f represents the fiber thickness.

We also obtain similar results for temperature distribution and polymerization evolution at $t = 2$ s as shown in Figure 5.20. However, the temperature diffusion in the composite that has low fiber content almost captures the temperature profile in composite that has the highest fiber ratio.
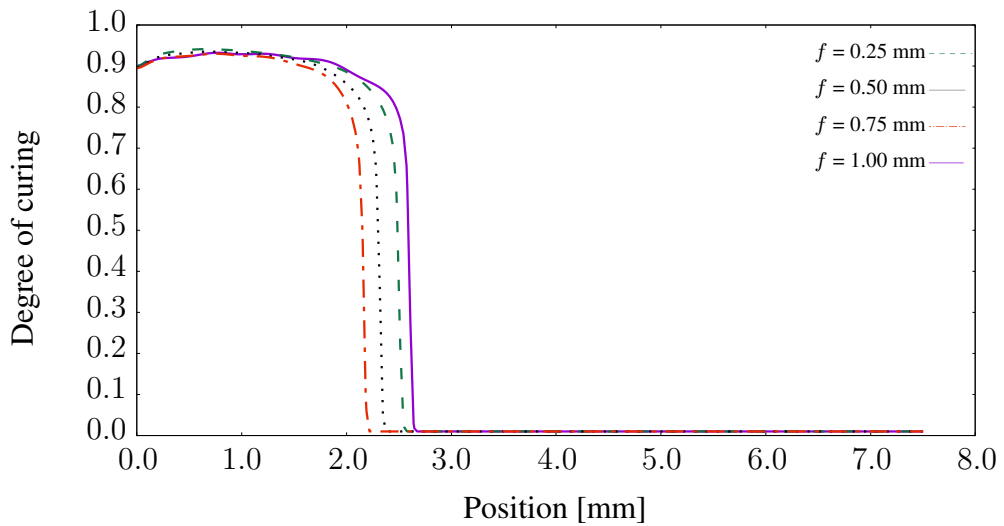
Figure 5.21: The evolution of the degree of curing at $t = 2$ s, where f represents the fiber thickness.

We also observe similar behavior for the degree of curing at $t = 2$ s as shown in Figure

5.21. The front propagation speed of the composite with the lowest fiber reaches the speed of the composite with the highest fiber ratio.
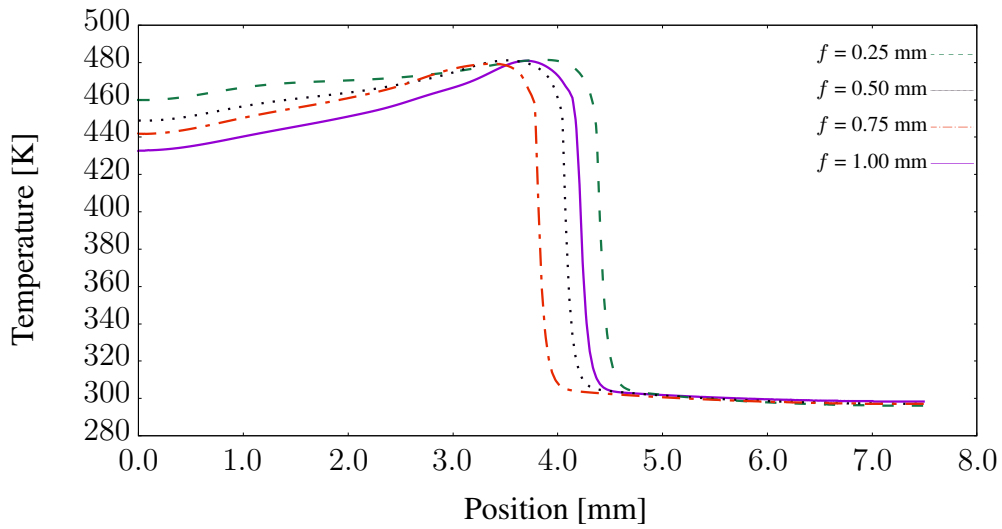
Figure 5.22: Temperature variation in the composite at $t = 3$ s, where f represents the fiber thickness.

Surprisingly, after $t = 3$ s, the temperature diffusion with the lowest fiber content composite moves faster than the with the highest fiber content one as shown in Figure 5.22.
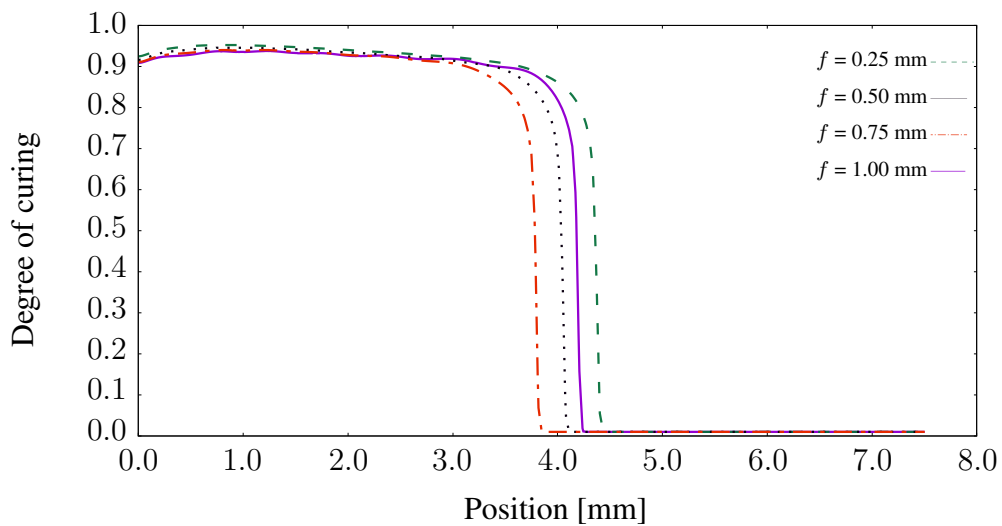
Figure 5.23: The evolution of degree of curing at $t = 3$ s, where f represents the fiber thickness.

76

In Figure 5.23, the curing propagation of the composite that has the lowest fiber also moves faster than with the one with the greatest fiber content.
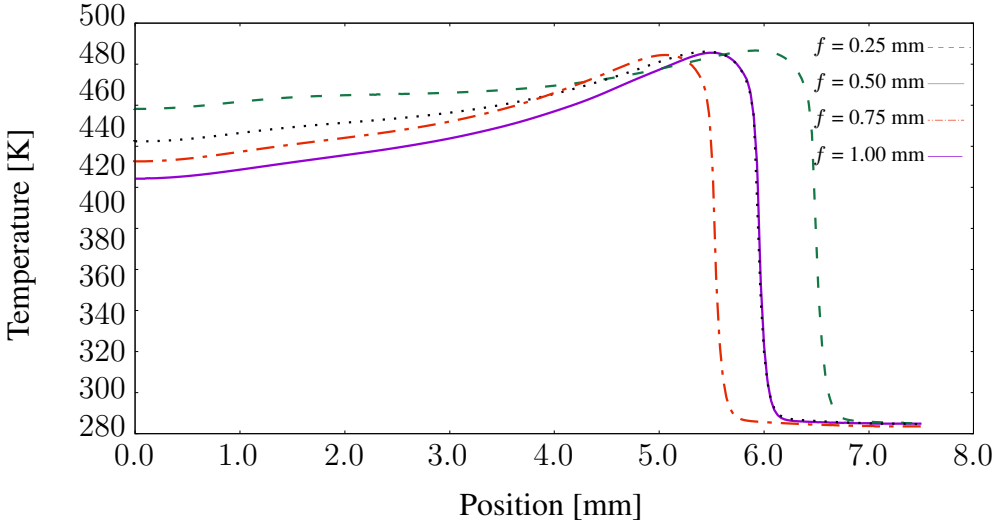
Figure 5.24: Temperature variation in the composite at $t = 4$ s, where f represents the fiber thickness.

After the $t = 4$ s, it becomes clear that the temperature distribution in the composite with low fiber is moving faster than in the composite with high fiber content as depicted in Figure 5.24.
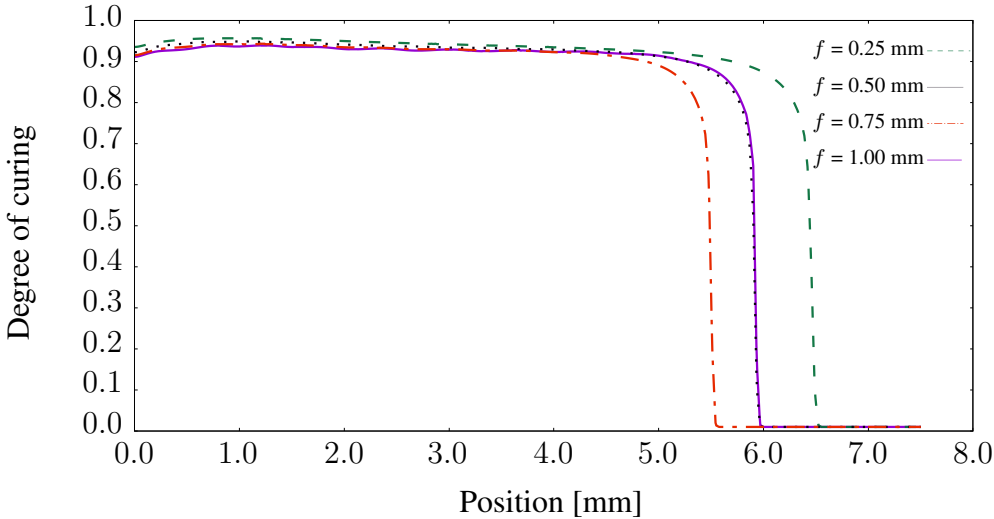
Figure 5.25: The evolution of degree of curing at $t = 4$ s, where f represents the fiber thickness.

We observe that the degree of curing has also a similar trend as temperature. The curing propagation comparisons in terms of carbon fiber are presented in Figure 5.25.

The reason for the behavior of the material depicted in Figure 5.25 is that the thermal diffusion rate increased at an optimum rate of fiber activates the chemical reaction and prevents the direct diffusion. Then, the polymerization reaction release heat, and more heat is transferred to the next monomer thanks to the fiber. It can prove the increase in thermal diffusion. Also, if we had excluded the heat source from our simulations suddenly, we would have obtained similar results because the chemical reaction is the main governing mechanism for this problem. Thus, it will be a very critical study to find the optimum fiber ratio that will provide the conduction to propagate polymerization properly.

As explained above, we have kept the domain size fixed in our simulations to compare the results of analyses consistently. In other words, as we increased the amount of fiber, we decreased the same amount of monomer. Therefore, we could not observe that the propagation of the polymerization moves faster in the composite that has a lower amount of fiber. We think that if the amount of monomer were fixed and only the amount of fiber changed, this difference could be observed more clearly.

Sottos and coworkers [3] notice a similar observation regarding the relation between temperature and curing propagation with fiber ration in the composite. Moreover, Sottos and coworkers claim that if the amount of fiber is increased, the analytical and modeling results diverge from each other due to the increasing thermal diffusion with higher fiber fractions. Therefore, this situation leads to an optimization problem between carbon fiber amount and polymerization. Also, Sottos and coworkers [3] state that the maximum temperature reached by the chemical reaction decreased with increasing carbon ratio. We also obtain the same result qualitatively as depicted in Figure 5.24.

As a result of our analysis, we observe that

- the sample with a fiber content of 0.25 mm thickness achieved optimum polymerization, compared to the others,
- temperature variations and the degree of polymerization evolution have the same

propagation trend,

- maximum reaction temperature is obtained in the polymer composite has the lowest fiber content.

5.2.3 Planar Front Propagation for Two Opposite Side Heating

In this example, we investigate the behavior of frontally polymerized material which is subjected to two opposite-side heating as shown in Figure 5.26. The behavior of this problem is slightly different from the previous examples. Thus, we investigate the chemical and thermal evolution in the material. The domain size is 7.5 mm × 7.5 mm and we used the 4-node quadrilateral elements of size $h = 0.033$ mm. The time increment $\Delta t = 10^{-4}$ s is used in the simulation.
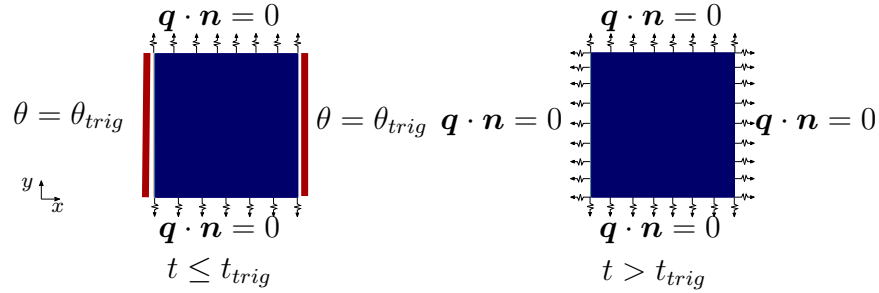
Figure 5.26: Boundary condition for the 2D model problem

We summarize the initial and boundary conditions in (5.4).

$$
\begin{aligned}
\theta(x, y, 0) &= 293 \text{ K}, \\
\alpha(x, y, 0) &= 0.05, \\
\theta(0, y, t) &= 453 \text{ K} \quad \text{for} \quad 0 \leq t \leq t_{trig}, \\
\theta(7.5, y, t) &= 453 \text{ K} \quad \text{for} \quad 0 \leq t \leq t_{trig}, \\
\nabla\theta|_{(0,y,t)} &= 0 \quad \text{for} \quad t > t_{trig}, \\
\nabla\theta|_{(x,0,t)} &= 0 \quad \text{for} \quad t \geq 0, \\
\nabla\theta|_{(7.5,y,t)} &= 0 \quad \text{for} \quad t > t_{trig}, \\
\nabla\theta|_{(x,7.5,t)} &= 0 \quad \text{for} \quad t \geq 0.
\end{aligned}
\tag{5.4}
$$

We present the simulations of the two-side heating in Figure 5.27.
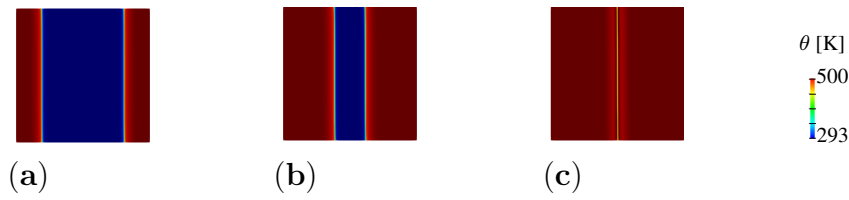
Figure 5.27: Temperature variation at a) $t = 1.0$ s, b) $t = 2.0$ s, c) $t = 2.5$ s

In this example, since we apply identical heating from both sides, the polymerization is completed in a half of the time of the one-sided heating. We take the section from the middle of the material and the thermal variation and chemical evolution of these sections are presented in Figure 5.28 and 5.29
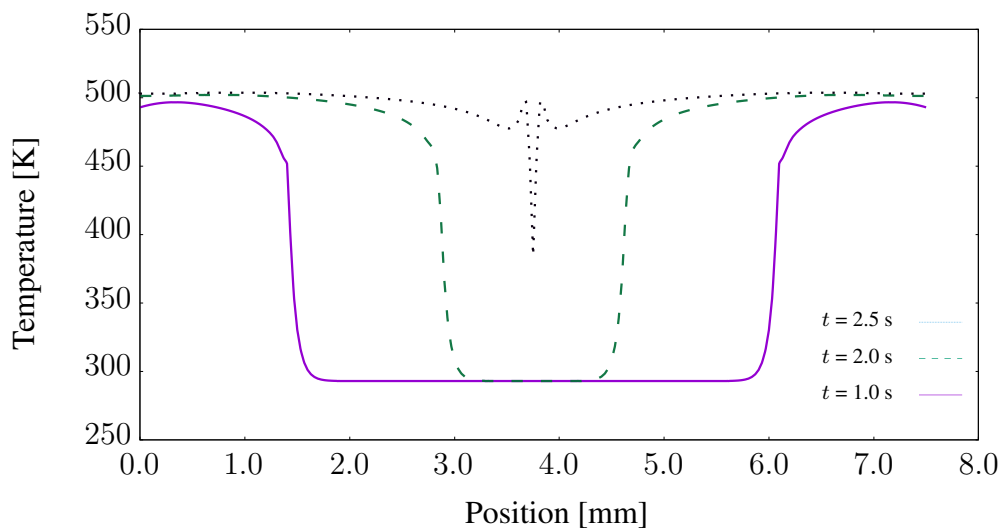

Figure 5.28: Temperature variation in composite at a) $t = 1.0$ s, b) $t = 2.0$ s, c) $t = 2.5$ s

As can be seen from Figure in 5.28, it has been observed that there is a temperature overshoot at the points where the temperatures converge. If the polymerization is allowed to continue in this way, severe degradation may be observed in this merging fronts of temperature as explained in [1].

80
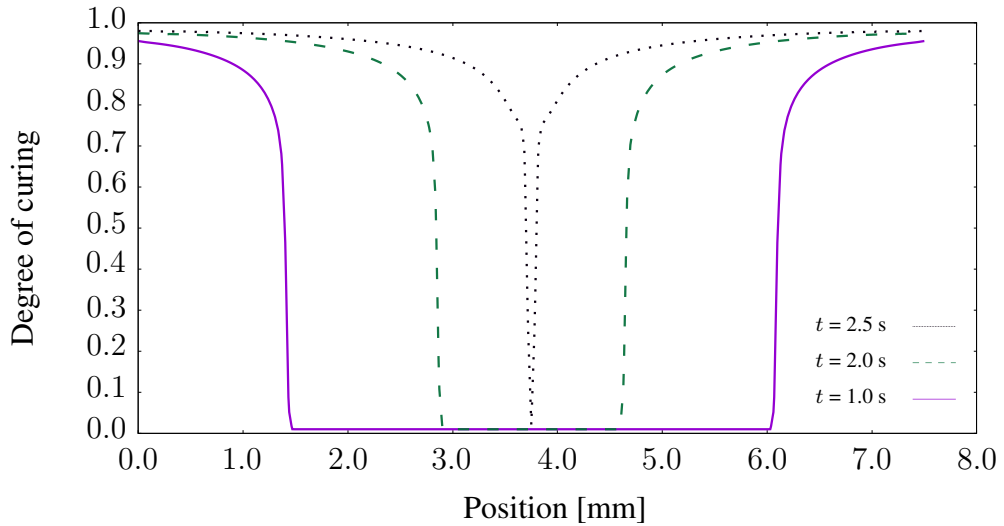
Figure 5.29: Degree of curing evolution with respect to position at a) $t = 1.0$ s, b) $t = 2.0$ s, c) $t = 2.5$ s

5.3 Chemo-Thermo-Mechanical Examples

In this section, we represent the behavior of the polymer and reinforced composite which are frontally polymerized. The problem is also very stiff and highly nonlinear due to the sharp temperature gradient and the degree of curing in the vicinity of the front for thermal and chemical part. Due to the formation of high expansion and chemical shrinkage, the mechanical part is also highly stiff.

We apply the thermal heating on the left side of the domain. Then, we investigate the chemical, thermal and mechanical evolution in the material. The domain size is 3.0 mm $\times$ 3.0 mm and we use the 4-node quadrilateral elements of size $h = 0.033$ mm. The time increment of $\Delta t = 10^{-4}$ s is used in the simulation. The material parameters which are used in the simulations are tabulated in Table 5.3.

Note that we also summarize material properties which we used in the following examples in Table 5.3:

Table 5.3: The summary of the material chemical, thermal and mechanical properties used in simulations

Material	Parameters	Unit	Definition	Value
Fiber	Λ	[MPa]	Lamé constant	30.36×10^4
	μ	[MPa]	Shear modulus	15.65×10^4
	α_θ	$[\frac{1}{K}]$	Thermal expansion coefficient	4.10×10^{-7}
	κ	$[\frac{W}{m \cdot K}]$	Thermal conductivity	9.30×10^0
	ρ	$[\frac{kg}{m^3}]$	Density	18.00×10^2
	C_p	$[\frac{J}{kg \cdot K}]$	Specific heat	75.36×10^1
PSU Foam	Λ	[MPa]	Lamé constant	12.60×10^0
	μ	[MPa]	Shear modulus	6.15×10^0
	α_θ	$[\frac{1}{K}]$	Thermal expansion coefficient	5.00×10^{-5}
	κ	$[\frac{W}{m \cdot K}]$	Thermal conductivity	2.20×10^{-2}
	ρ	$[\frac{kg}{m^3}]$	Density	32.50×10^0
	C_p	$[\frac{J}{kg \cdot K}]$	Specific heat	14.53×10^2
Monomer (DPCD)	Λ	[MPa]	Lamé constant	6.21×10^0
	μ	[MPa]	Shear modulus	6.9×10^{-1}
	α_θ	$[\frac{1}{K}]$	Thermal expansion coefficient	79.00×10^{-6}
	ξ_c	[%]	Chemical shrinkage coefficient	-6.00×10^{-2}
	κ	$[\frac{W}{m \cdot K}]$	Thermal conductivity	1.50×10^{-1}
	ρ	$[\frac{kg}{m^3}]$	Density	98.00×10^1
	C_p	$[\frac{J}{kg \cdot K}]$	Specific heat	16.00×10^2
	A	$[\frac{1}{s}]$	Pre-exponential factor	8.22×10^{15}
	E	$[\frac{kJ}{mol}]$	Activation energy	11.07×10^1
	A	$[\frac{1}{s}]$	Pre-exponential factor	8.22×10^{15}

	H_r	$[\frac{J}{g}]$	Total enthalpy of reaction	35.00×10^1
Monomer	n	[]	Orders of reaction	1.72×10^0
(DPCD)	m	[]	Orders of reaction	7.70×10^{-1}
	C	[]	Diffusion constant	14.48×10^0
	α_c	[]	Diffusion constant	4.10×10^{-1}
	R	$[\frac{J}{mol \cdot K}]$	universal gas constant	83.14×10^{-1}
	Λ	[MPa]	Lamé constant	6.21×10^3
	μ	[MPa]	Shear modulus	6.90×10^2
Polymer	α_θ	$[\frac{1}{K}]$	Thermal expansion coefficient	79.00×10^{-9}
(DPCD)	ξ_c	[%]	Chemical shrinkage coefficient	-6.00×10^{-3}
	κ	$[\frac{W}{m \cdot K}]$	Thermal conductivity	15.00×10^{-2}
	ρ	$[\frac{kg}{m^3}]$	Density	98.00×10^1
	C_p	$[\frac{K}{kg \cdot K}]$	Specific heat	16.00×10^2

The mechanical material properties are adopted from [1] for mono-poly/mer. The chemical shrinkage coefficient and thermal expansion coefficient of mono-poly/mer are adopted from [35], [36], respectively. Besides, the thermal and mechanical properties of fiber and polyisocyanurate foam are borrowed from [37] and [38], respectively.

$$\Lambda = \Lambda_f - (\Lambda_f - \Lambda_i) \tanh(\frac{\alpha_n - 0.04}{-T_f})$$
$$\mu = \mu_f - (\mu_f - \mu_i) \exp(\frac{\alpha_n}{-T_f})$$
$$\alpha_\theta = \alpha_{\theta f} - (\alpha_{\theta f} - \alpha_{\theta i}) \exp(\frac{\alpha_n}{-T_f})$$
$$\xi_c = \xi_{cf} - (\xi_{cf} - \xi_{ci}) \exp(\frac{\alpha_n}{-T_f})$$

(5.5)

The curing-induced growth of polymer in rigidity is modeled through the reaction conversion expressions that evaluate the mechanical properties in terms of the degree of curing as explained in Chapter 3. This behavior is modeled by the switch functions as shown in (5.5).

We present the evolution of the material properties in Figures 5.30, 5.31, 5.32 and

5.33. The Lamé constant (Λ) of polymer is 6.21×10^3 MPa. On the other hand, the Lamé constant (Λ) of monomer is 6.21×10^0 MPa as depicted in Figure 5.30.
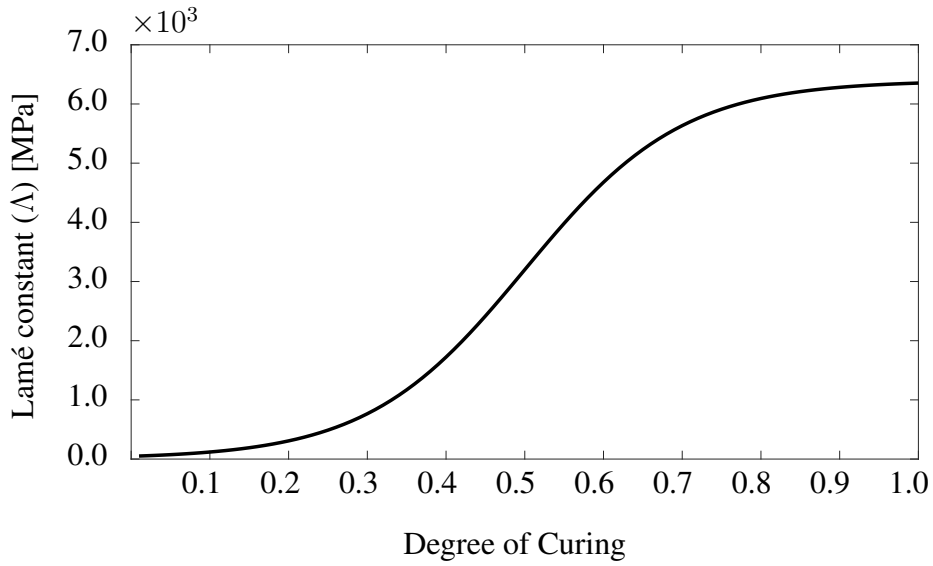
Figure 5.30: The evolution of the Lamé constant with respect to the degree of curing

In Figure 5.31, the evolution of the shear modulus evolution is presented. The shear modulus of polymer is 6.9×10^2 MPa and the shear modulus of monomer is 6.9×10^{-1} MPa.
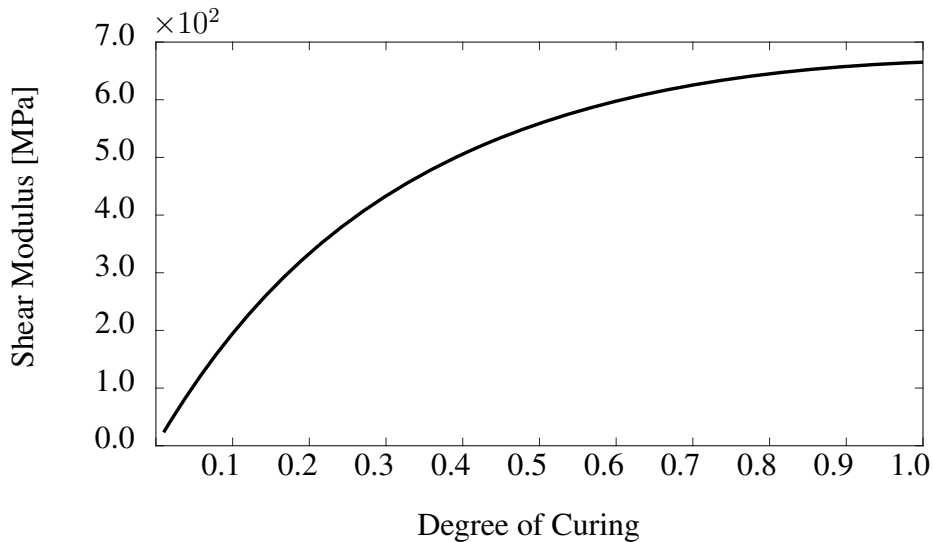

Figure 5.31: The evolution of the shear modulus with respect to the degree of curing

The thermal expansion coefficient is evaluated with the degree of curing as shown in

84

Figure 5.32. The thermal expansion coefficient of polymer is 7.96×10^{-9} 1/K and the thermal expansion coefficient of monomer is 7.96×10^{-6} 1/K. We observe that the thermal expansion coefficient has a decreasing trend in the reasoning to the degree of curing.
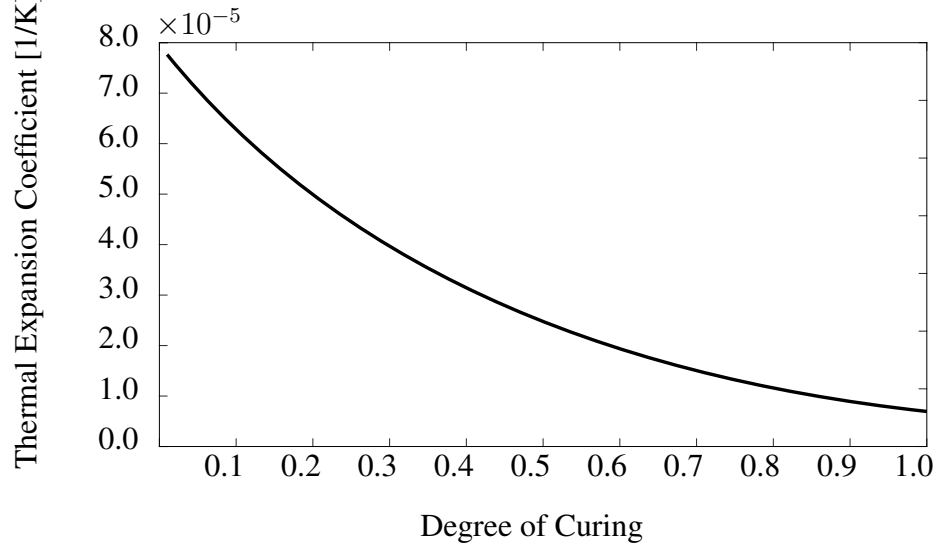
Figure 5.32: The evolution of the thermal expansion coefficient with respect to the degree of curing

The chemical shrinkage coefficient of polymer is -6×10^{-3} and -6×10^{-2} is obtained for monomer as shown in Figure 5.33.
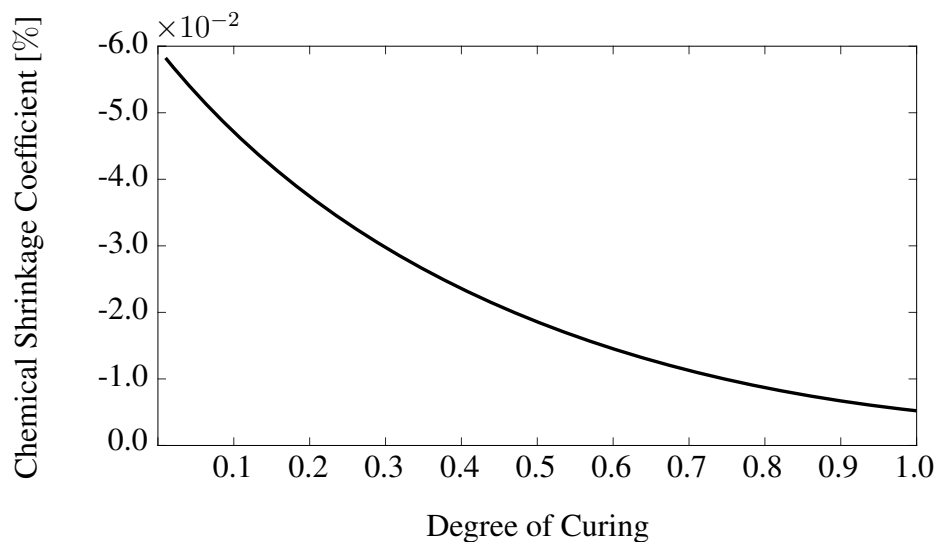
Figure 5.33: The evolution of the chemical shrinkage coefficient with respect to the degree of curing

Similar to the thermal expansion coefficient, the chemical shrinkage coefficient also has a decreasing trend with respect to curing.

5.3.1 2D Planar Front

In this example, we investigate the mechanical behavior of frontally polymerized material which is subjected to heating from right side of the domain as shown in Figure 5.34. The domain size is 3.0 mm × 3.0 mm and we used 4-node quadrilateral elements size of $h = 0.033$ mm. Time increment is used $\Delta t = 10^{-4}$ s in the simulation.
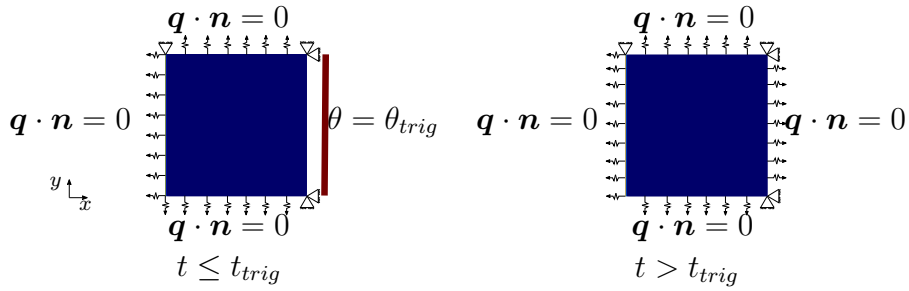
Figure 5.34: Boundary conditions for chemo-thermo-mechanical problem

The initial and boundary conditions for thermal problem are described in (5.6).

$$
\begin{aligned}
&\theta(x, y, 0) = 293 \text{ K}, \\
&\alpha(x, y, 0) = 0.05, \\
&\theta(0, y, t) = 453 \text{ K} \quad \text{for} \quad 0 \leq t \leq t_{trig}, \\
&\nabla\theta|_{(0,y,t)} = 0 \quad \text{for} \quad t > t_{trig}, \\
&\nabla\theta|_{(x,0,t)} = 0 \quad \text{for} \quad t \geq 0, \\
&\nabla\theta|_{(3,y,t)} = 0 \quad \text{for} \quad t \geq 0, \\
&\nabla\theta|_{(x,3,t)} = 0 \quad \text{for} \quad t \geq 0,
\end{aligned}
\tag{5.6}
$$

86

The boundary conditions for mechanical problem are described in (5.7).

$$u_x|_{(3,0,t)} = 0,$$
$$u_y|_{(3,0,t)} = 0,$$
$$u_x|_{(3,3,t)} = 0, \tag{5.7}$$
$$u_y|_{(3,3,t)} = 0,$$
$$u_y|_{(0,3,t)} = 0.$$

The temperature distribution in this example, which has a similar trend to that of the chemo-thermal simulation, presented in Figure 5.35 since we assumed that the mechanical part has a little effect on the thermal and chemical part.
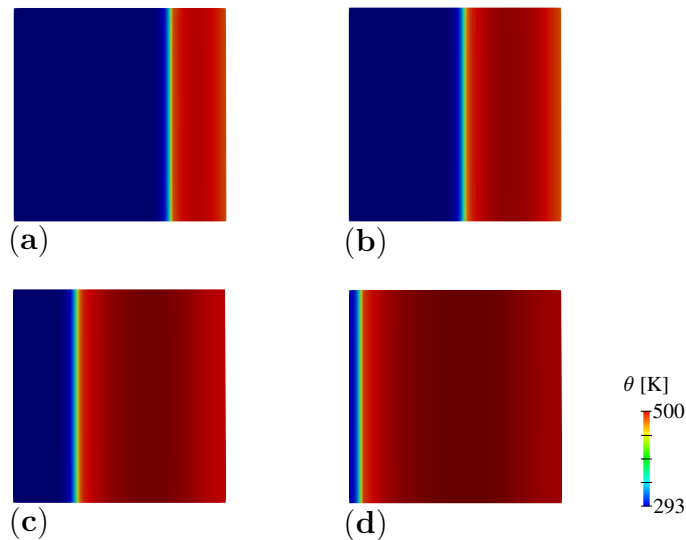
Figure 5.35: Thermal variation of chemo-thermo-mechanical coupled problem, a) $t = 0.5$ s, b) $t = 1.0$ s, c) $t = 1.5$ s, d) $t = 2.0$ s

We have also described how the temperature distribution propagate in the x-axis direction in Figure 5.36.
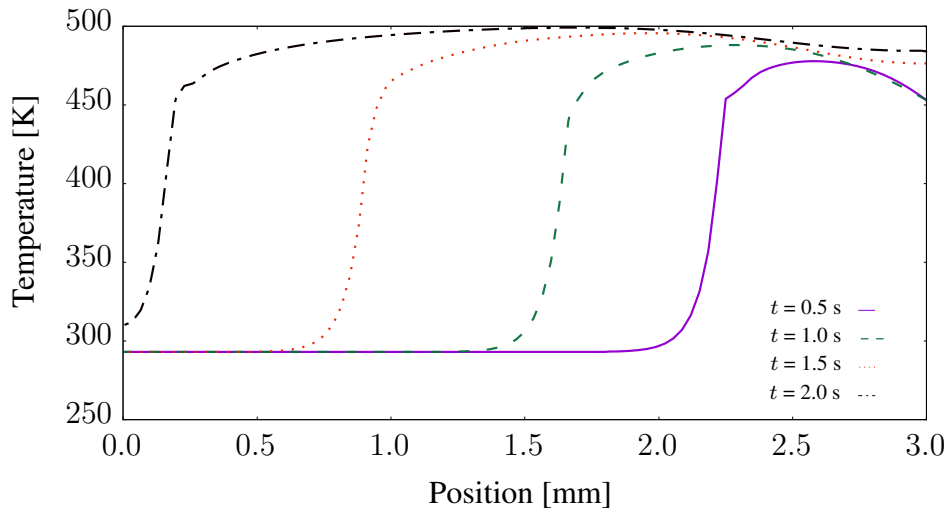
Figure 5.36: The variation of temperature variation with respect to position and time

Similarly, the polymerization propagation shows the same characteristic with chemo-thermal problem as shown in Figure 5.37.
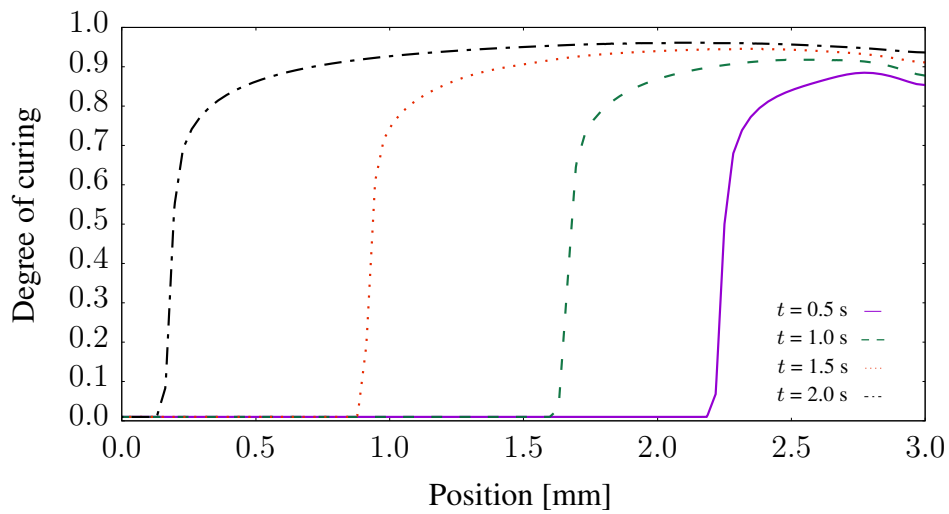
Figure 5.37: The evolution of the degree of curing with respect to position and time

In Figure 5.38, it is observed that there is expansion in the places where initially the heat is applied. However, it is apparent that shrinkage starts at the edges with the effect of polymerization and this propagates with the polymerization front. An asymmetric behavior has occurred due to the mechanical boundary conditions.
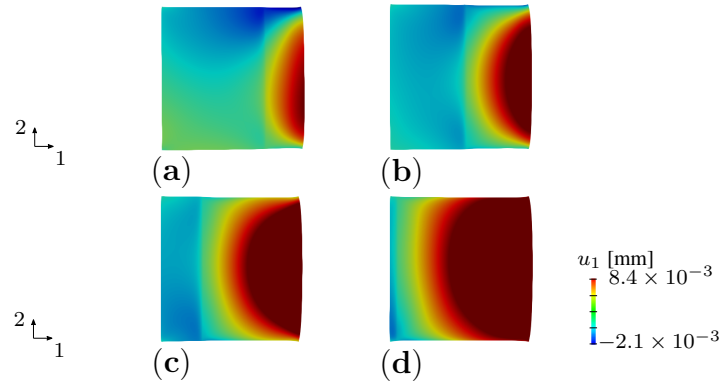
Figure 5.38: Displacement simulation u_1 for material frontally polymerized at a) $t = 0.5$ s, b) $t = 1.0$ s, c) $t = 1.5$ s, d) $t = 2.0$ s

Similarly, we observe a downward deformation at the upper edge and an upward deformation at the lower edge due to the boundary conditions as shown in Figure 5.39. On the right edge, we observe an outward expansion of the sample.
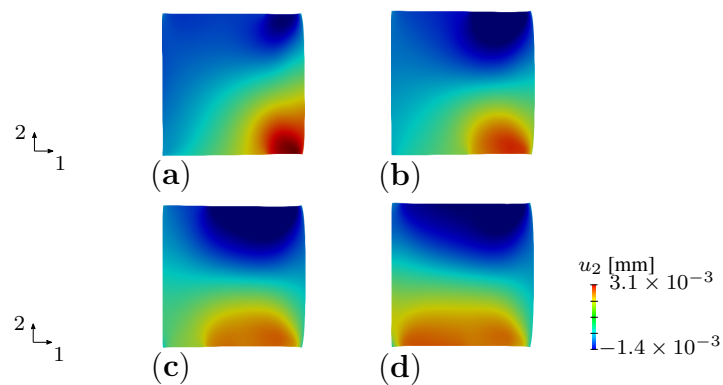

Figure 5.39: Displacement simulation u_2 for material frontally polymerized at a) $t = 0.5$ s, b) $t = 1.0$ s, c) $t = 1.5$ s, d) $t = 2.0$ s

From the stress point of view, the stress is appeared in the region of the front of polymerization and moving along with as shown in Figure 5.40.
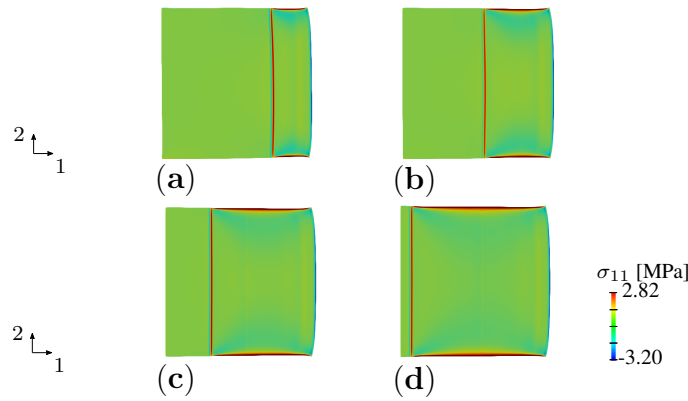
Figure 5.40: σ_{11} simulation for material frontally polymerized at a) $t = 0.5$ s, b) $t = 1.0$ s, c) $t = 1.5$ s, d) $t = 2.0$ s

Although these stresses do not accumulate in the inner regions due to the boundary conditions, it is observed that they remain at a significant amount in the side regions. This causes a loss of strength at the edges of the material because stress accumulations may act as imperfection, so it is a very crucial problem as these regions are in direct contact with the outside.
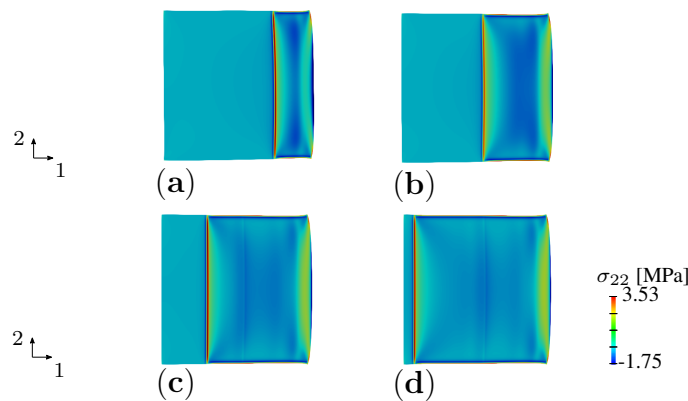
Figure 5.41: σ_{22} simulation for material frontally polymerized at a) $t = 0.5$ s, b) $t = 1.0$ s, c) $t = 1.5$ s, d) $t = 2.0$ s

If we look at the stress view in σ_{22} direction, we observe that they accumulate on the right and left boundaries due to the boundary conditions as seen in Figure 5.41. A large amount of stress accumulation is observed on the sides of the domain.
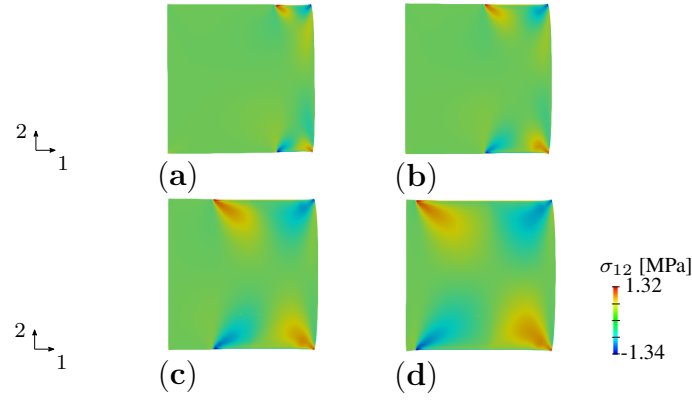
Figure 5.42: σ_{12} simulation for material frontally polymerized at a) $t = 0.5$ s, b) $t = 1.0$ s, c) $t = 1.5$ s, d) $t = 2.0$ s

In terms of shear stress, we obtain compatible results with the stress axial stress. According to these results, it is observed that the material tries to rotate counterclockwise direction in accordance with the boundary conditions. Thus, shear stress accumulations are observed in Figure 5.42.

According to the results obtained, the deformations and stresses that will occur during the manufacturing of the polymer are described computationally. These strains can also be determined experimentally using methods such as the digital image correlation (DIC).

The serious accumulation of stresses is observed according to the results of analyses, although the magnitude of stress that will affect the strength of the material is relatively small concerning the strength of the final product. These stresses may differ according to manufacturing conditions and material properties used in composite structures, and they may cause serious strength losses.

5.3.2 2D Non-Planar Front

In this example, we investigate the mechanical behavior of a frontally polymerized fiber-reinforced composite material which is subjected to heating from left side of the domain as shown in Figure 5.43. The domain size is 3.0 mm $\times$ 3.0 mm and we used 4-node quadrilateral elements of size $h = 0.033$ mm. The time increment is used

$\Delta t = 10^{-4}$ s in the simulation. Moreover, the thicknesses of the fiber and glass are 0.5 mm and 0.75 mm, respectively.

The initial and boundary conditions for the thermal problem are shown in Figure 5.43 (a) and described in (5.8).

$$\theta(x, y, 0) = 293 \text{ K},$$
$$\alpha(x, y, 0) = 0.05,$$
$$\theta(0, y, t) = 453 \text{ K} \quad \text{for} \quad 0 \leq t \leq t_{trig} \quad \text{where} \quad y = [0.5, 2.25],$$
$$\nabla\theta|_{(0,y,t)} = 0 \quad \text{for} \quad t > t_{trig}, \tag{5.8}$$
$$\nabla\theta|_{(x,0,t)} = 0 \quad \text{for} \quad t \geq 0,$$
$$\nabla\theta|_{(3,y,t)} = 0 \quad \text{for} \quad t \geq 0,$$
$$\nabla\theta|_{(x,3,t)} = 0 \quad \text{for} \quad t \geq 0.$$

Also, the boundary conditions for the mechanical part are depicted in Figure 5.43 (b) and defined as in (5.9)

$$u_x|_{(x,0,t)} = 0,$$
$$u_y|_{(x,0,t)} = 0,$$
$$u_x|_{(x,3,t)} = 0, \tag{5.9}$$
$$u_y|_{(x,3,t)} = 0$$
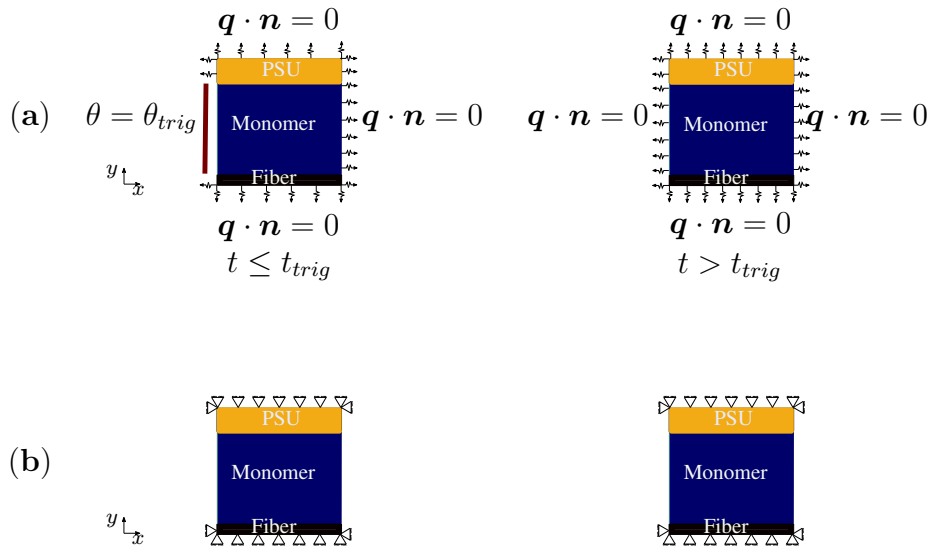
Figure 5.43: Boundary conditions for the chemo-thermo-mechanical coupled 2D problem a)thermal boundary conditions, b) for mechanical boundary conditions.

The temperature distribution in this example, which has a similar trend to that of the chemo-thermal simulation of the fiber reinforced composite example in Section 5.2.1, is presented in Figure 5.44 since we assumed that the mechanical part has no effect on the thermal and chemical parts. We can observe the polymerization front characteristic changing from flat to conical shape.
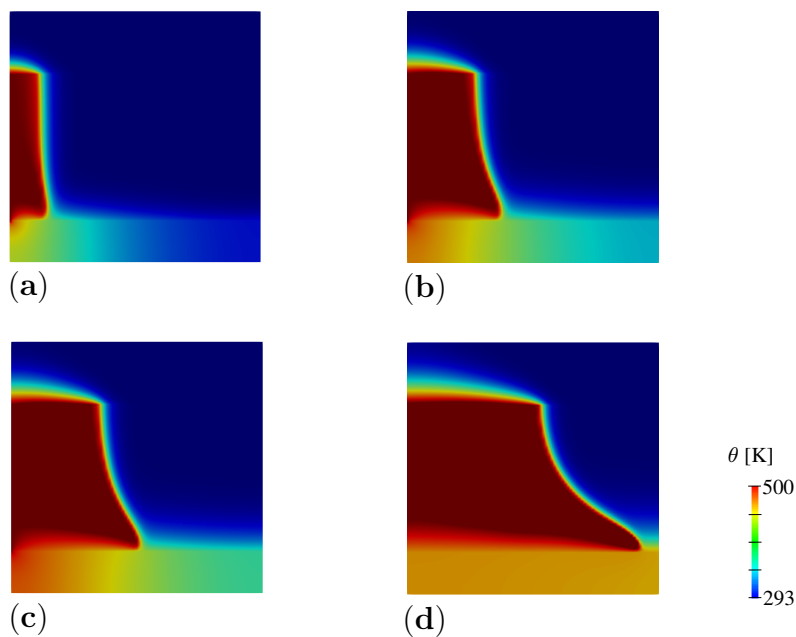

Figure 5.44: Temperature propagation of chemo-thermo-mechanical coupled problem for composite sample at a) $t = 0.2$ s, b) $t = 0.6$ s, c) $t = 1.0$ s, d) $t = 1.4$ s.

We have extracted sections from 0.25 mm above the fiber in the materials we used in the simulations above for the temperature and the degree of curing curves presented in Figures 5.45 and 5.46.

It is observed that the temperature diffusion was much faster in the composite structure compared to the planar front sample discussed in Section 5.3.1.
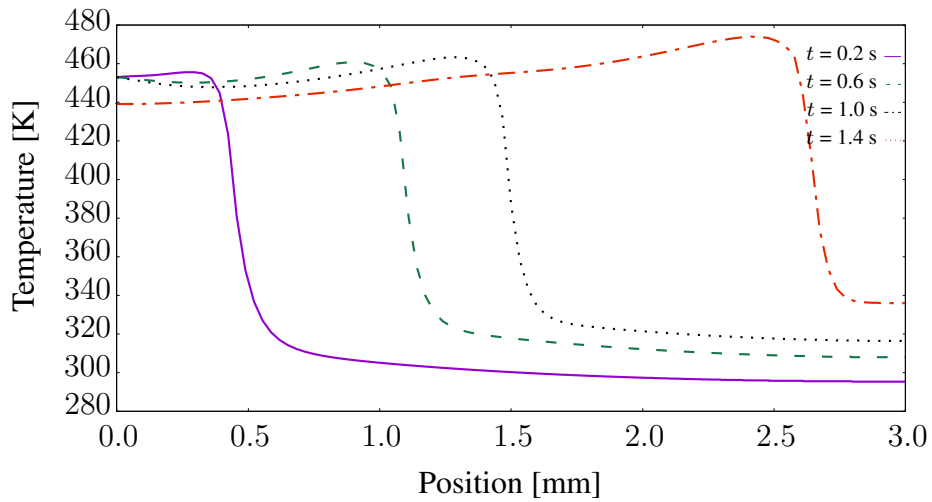
Figure 5.45: Temperature distribution with respect to position and time

Similarly, the polymerization propagation shows the same characteristic as temperature as shown in Figure 5.46. Also, we can observe that the polymerization propagation in a composite structure is faster than the planar front sample discussed in Section 5.3.1. The use of fiber is important for manufacturing, since this will both accelerate the polymerization and allow the next monomer to react without diffusing the heat released from the previous reaction.
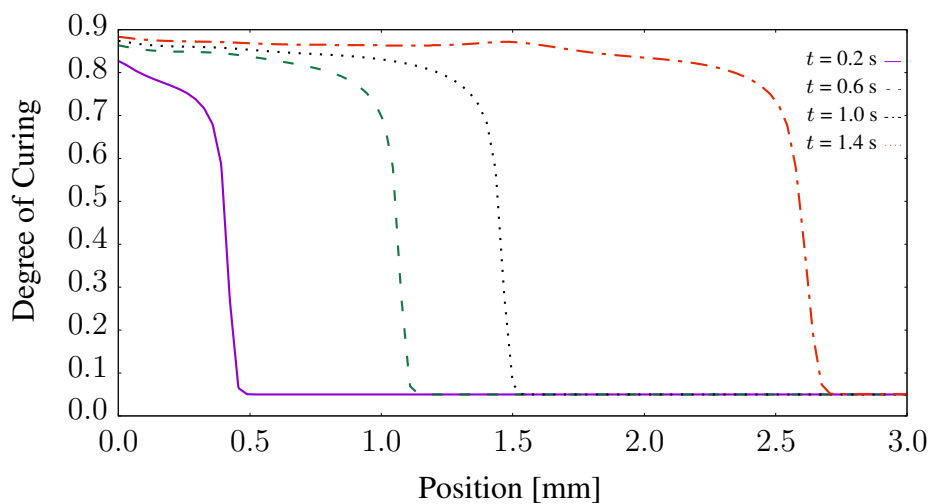
Figure 5.46: Degree of curing evaluation with respect to position and time
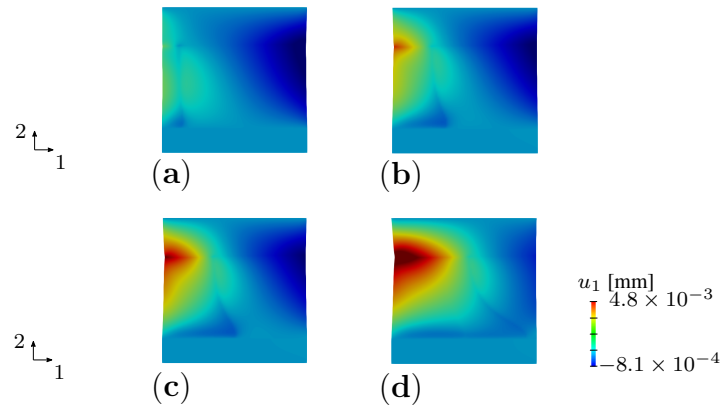
Figure 5.47: Displacement u_1 simulation for material frontally polymerized at a) $t = 0.2$ s, b) $t = 0.6$ s, c) $t = 1.0$ s, d) $t = 1.4$s.

In the deformation part, we observe that high amount of shrinkage occurs in regions for the junction of the fiber and the monomer due to polymerization. On the other hand, it is observed that serious expansion is formed in the region between PSU foam and monomer as well due to the shrinkage of the monomer.
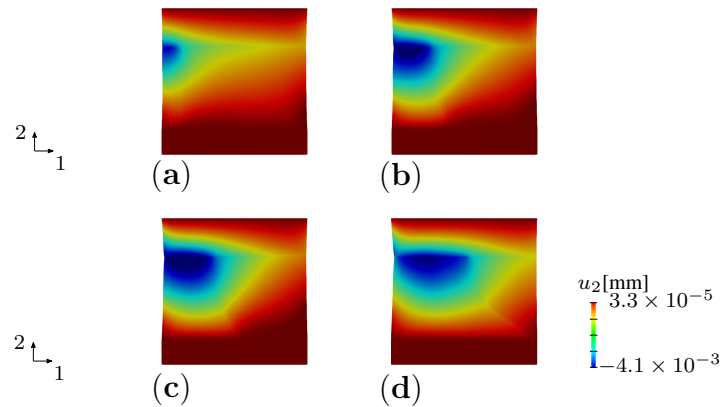

Figure 5.48: Displacement simulation u_2 for material frontally polymerized at a) $t = 0.2$ s, b) $t = 0.6$ s, c) $t = 1.0$ s, d) $t = 1.4$s.

In the $y - y$ direction, an upward deformation occurred between the monomer and the fiber as shown in Figure 5.48. The fiber tries to stretch with temperature increase whereas polymer shrinks due to the polymerization. The monomer expands due to temperature, but when we compare the expansion and contraction values, it is seen that the contraction dominates.
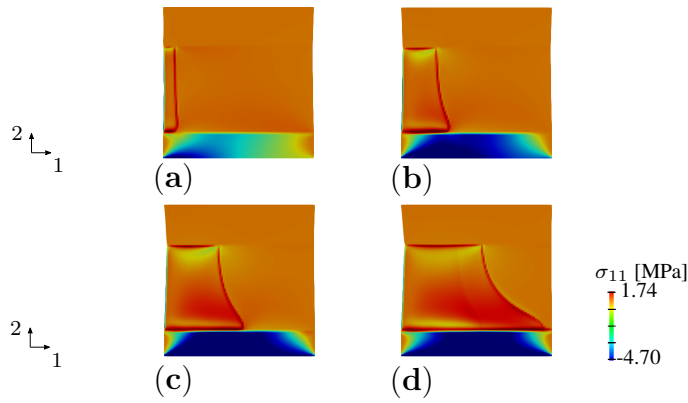
Figure 5.49: σ_{11} simulation for material frontally polymerized at a) $t = 0.2$ s, b) $t = 0.6$ s, c) $t = 1.0$ s, d) $t = 1.4$ s

In Figure 5.49, huge stress jump occurs between the fiber and the monomer in the x-x direction.
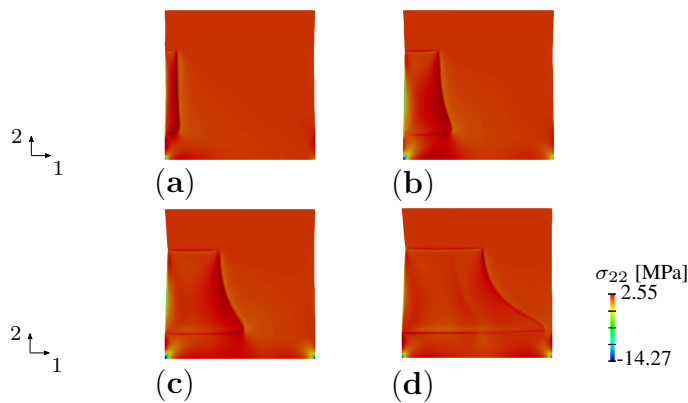

Figure 5.50: σ_{22} simulation for material frontally polymerized at a) $t = 0.2$ s, b) $t = 0.6$ s, c) $t = 1.0$ s, d) $t = 1.4$ s

Similar to the displacement results, while the fiber expands with temperature, the monomer shrinks with polymerization and both materials apply the restriction to each other. Thus, it is observed that compressive stresses (σ_{11}) occur in the fiber and tensile stresses (σ_{11}) in the monomer. Moreover, it is important to note that it reaches a relatively large value on Figure 5.49 as about 9 MPa at the corners.
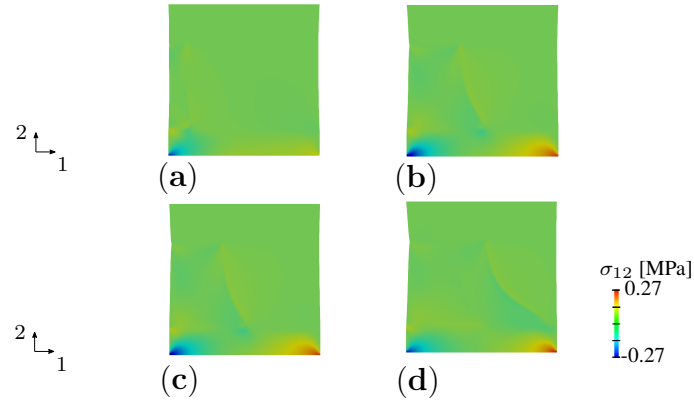
Figure 5.51: σ_{12} simulation for material frontally polymerized at a) $t = 0.2$ s, b) $t = 0.6$ s, c) $t = 1.0$ s, d) $t = 1.4$ s

In y-y direction, we can observe that stresses occur between the monomer and the fiber. There are also stresses around the polymerization front.

Shear stress accumulation is observed in the supports as shown in Figure 5.51. It has been detected that there are small shear stresses around the front in the inner regions.

According to the results of the analyses, the deformations and stresses that will occur during the manufacturing of the fiber reinforced composite are examined computationally. We observe the serious stress accumulations in the composite material, although the magnitude of stress that will affect the strength of the material is relatively small concerning the strength of the final product similar to planar front example. However, we observe the stresses between the fiber and the monomer, and it may cause a severe loss of the strength in the final product. Therefore, this interface will have a significant effect on the strength of the composite product.

5.3.3 3D Planar Front Examples

In this example, we investigate the behavior of frontally polmerized matieral which is subjected to heating from left side of the domain as shown in Figure 5.52. Then, we investigate the chemical, thermal and mechanical evolution in the material. The domain size is 3.0 mm $\times$ 3.0 mm $\times$ 1.0 mm and we used the mesh size of $h = 0.033$ mm. Time increment $\Delta t = 10^{-4}$ s is used in the simulation.
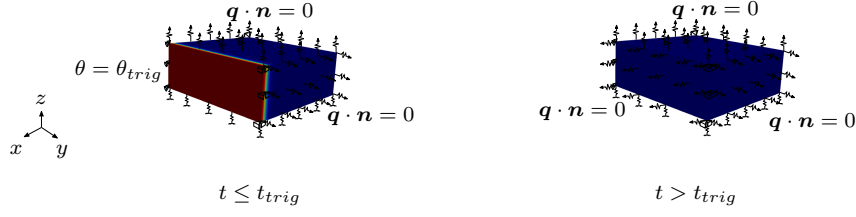
Figure 5.52: Boundary conditions for the 3D chemo-thermo-mechanical coupled problem.

The boundary conditions for mechanical problem are described in (5.10).

$$u_x|_{(0,0,z,t)} = 0,$$
$$u_y|_{(0,0,z,t)} = 0,$$
$$u_x|_{(0,3,z,t)} = 0, \qquad \qquad (5.10)$$
$$u_y|_{(0,3,z,t)} = 0,$$
$$u_y|_{(0,3,z,t)} = 0.$$

The initial and boundary conditions for thermal problem are described in (5.11).

$$\theta(x, y, z, 0) = 293 \text{ K},$$
$$\alpha(x, y, z, 0) = 0.05,$$
$$\theta(0, y, z, t) = 453 \text{ K} \quad \text{for} \quad 0 \le t \le t_{trig},$$
$$\nabla\theta|_{(0,y,z,t)} = 0 \quad \text{for} \quad t > t_{trig},$$
$$\nabla\theta|_{(x,0,z,t)} = 0 \quad \text{for} \quad t \ge 0, \qquad (5.11)$$
$$\nabla\theta|_{(3,y,z,t)} = 0 \quad \text{for} \quad t \ge 0,$$
$$\nabla\theta|_{(x,3,z,t)} = 0 \quad \text{for} \quad t \ge 0,$$
$$\nabla\theta|_{(x,y,0,t)} = 0 \quad \text{for} \quad t \ge 0,$$
$$\nabla\theta|_{(x,y,1,t)} = 0 \quad \text{for} \quad t \ge 0,$$

We have also compression-only springs through the bottom part of the domain in order to observe the upward displacements properly.

The temperature distribution of this problem, has a similar trend to that of previous planar front simulations, presented in Figure 5.53.
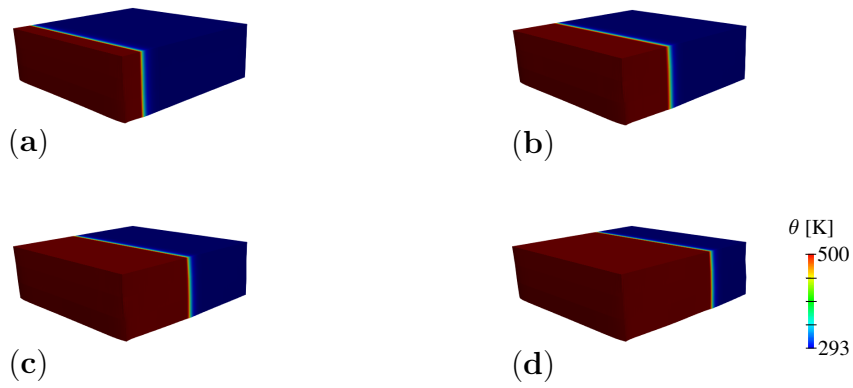
98

Figure 5.53: Temperature propagation of chemo-thermo-mechanical 3D coupled problem at a) t = 0.2 s, b) t = 0.6 s, c) t = 1.0 s, d) t = 1.4 s.

We have also depicted the temperature distribution propagation in thr x-axis direction in Figure 5.54. The section is taken through the midpoint of the domain.
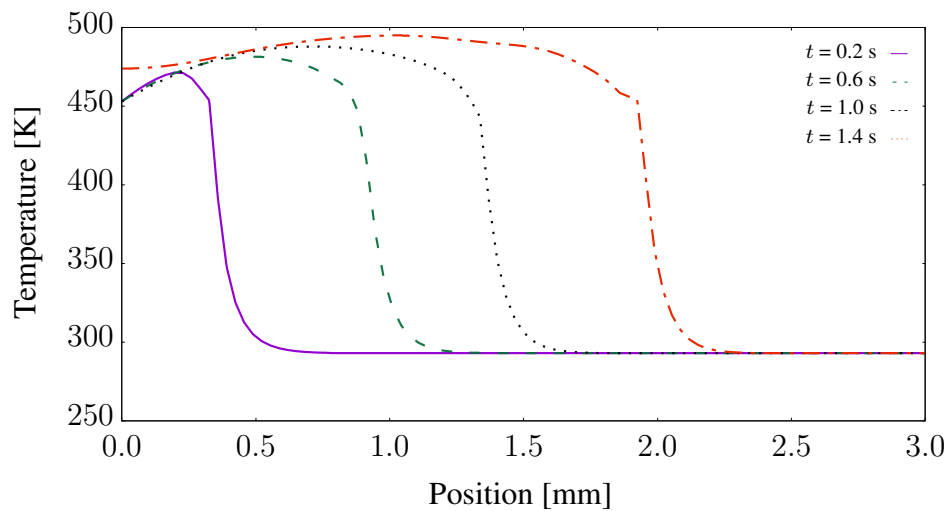

Figure 5.54: Temperature propagation of chemo-thermo-mechanical 3D coupled problem at a) t = 0.2 s, b) t = 0.6 s, c) t = 1.0 s, d) t = 1.4 s.

Similarly, the polymerization propagation shows the similar graphical characteristic with the temperature profile as shown in Figure 5.55.
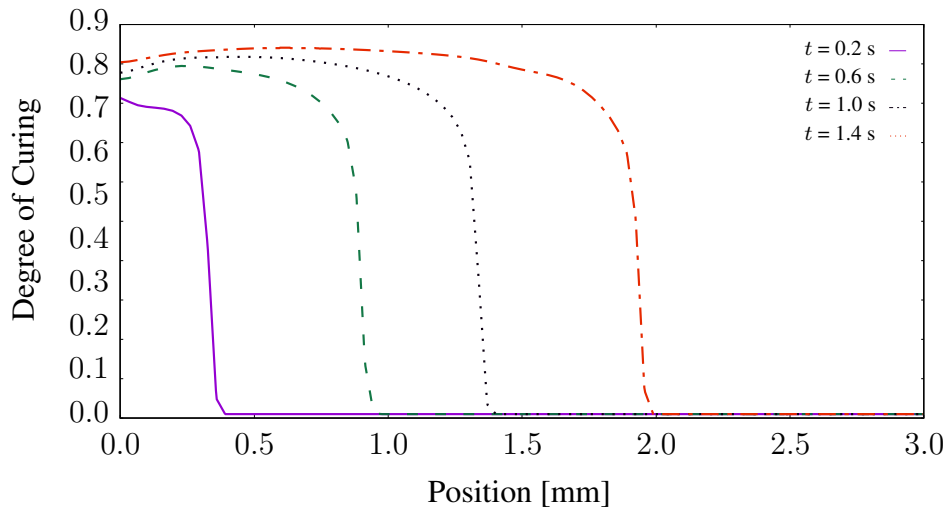
Figure 5.55: The polymerization propagation of chemo-thermo-mechanical 3D coupled problem at a) t = 0.2 s, b) t = 0.6 s, c) t = 1.0 s, d) t = 1.4 s.

In Figure 5.56, we observe that the top of the domain displaces the reverse direction of 1-1 due to shrinkage and boundary conditions. On the other hand, it is observed that the inside and bottom of the domain move the the direction of 1-1. Moreover, the shrinkage deformations also progress with the propagation of the polymerization.
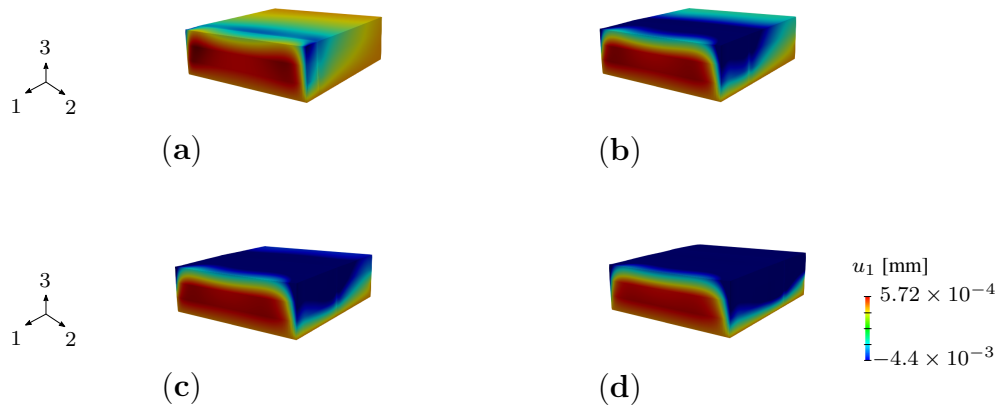

Figure 5.56: Displacement u_1 simulation for material frontally polymerized at a) $t = 0.2$ s, b) $t = 0.6$ s, c) $t = 1.0$ s, d) $t = 1.4$s.

In 2-2 direction, the inward displacements around the boundary are observed due to the shrinkage and boundary conditions as shown in Figure 5.57.
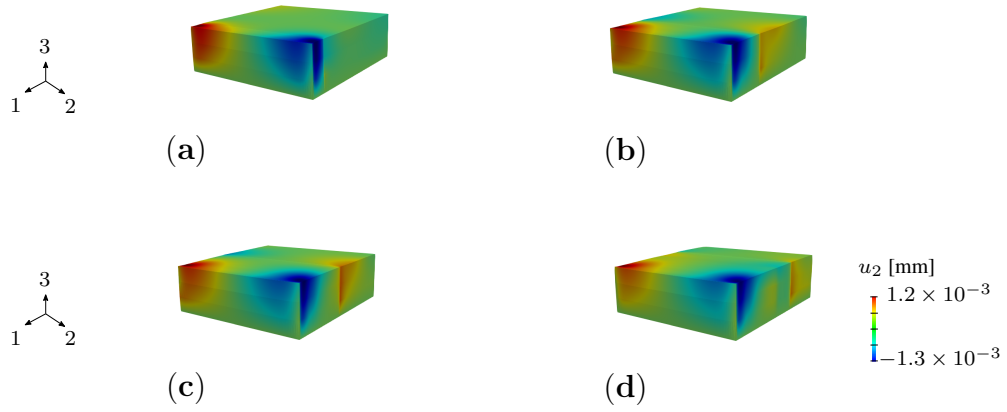
Figure 5.57: Displacement simulation u_2 for material frontally polymerized at a) $t = 0.2$ s, b) $t = 0.6$ s, c) $t = 1.0$ s, d) $t = 1.4$s.

Also, it is observed that the material is trying to move upwards direction. On the other hand, the left edge of the domain moves to downward direction due to the boundary conditions as shown in Figure 5.58.
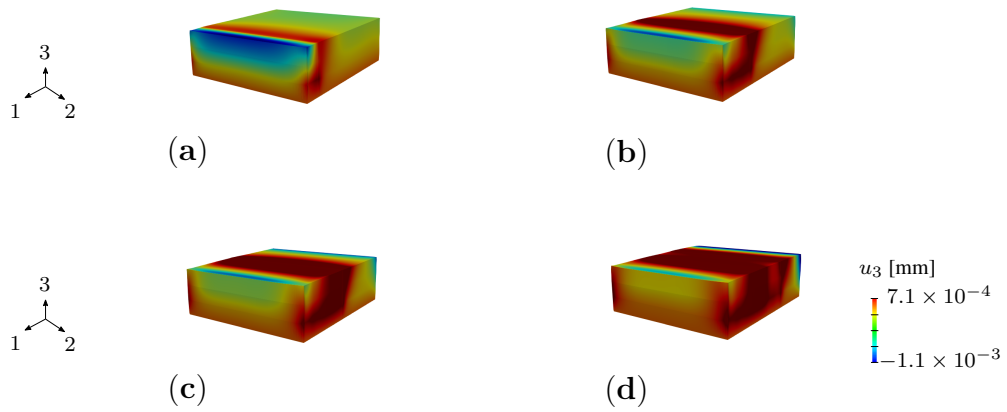

Figure 5.58: Displacement simulation u_3 for material frontally polymerized at a) $t = 0.2$ s, b) $t = 0.6$ s, c) $t = 1.0$ s, d) $t = 1.4$s.

In the stress point of view, stresses are accumulated more on the left and right side of the domain due to the boundary conditions. Moreover, we observe the stress accumulations in the inner side of the domain as shown in Figure 5.59.
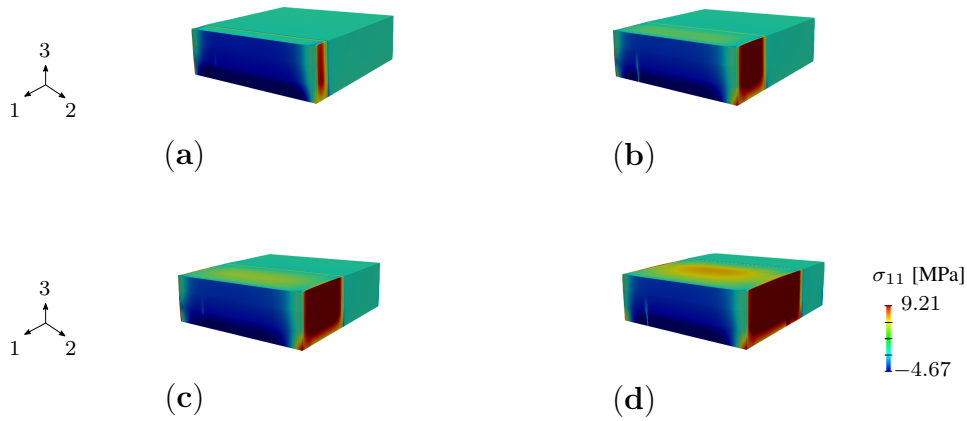
Figure 5.59: σ_{11} simulation for material frontally polymerized at a) $t = 0.2$ s, b) $t = 0.6$ s, c) $t = 1.0$ s, d) $t = 1.4$ s

In the 2-2 direction, we also observe the stress accumulations on the left and right side of the domain but the stress values are not as much as high in the 1-1 direction. The stress accumulations are dependent on the boundary conditions as shown in Figure 5.60.
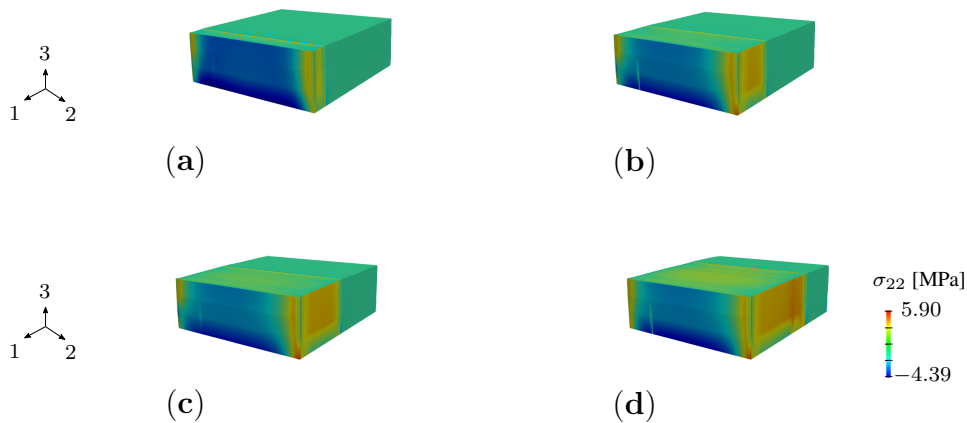

Figure 5.60: σ_{22} simulation for material frontally polymerized at a) $t = 0.2$ s, b) $t = 0.6$ s, c) $t = 1.0$ s, d) $t = 1.4$ s

In the 3-3 direction, the stress accumulations are observed the regions similar to the 1-1 and 2-2 directions as shown in Figure 5.61. They are also dependent on the boundary conditions.

Figure 5.61: σ_{33} simulation for material frontally polymerized at a) $t = 0.2$ s, b) $t = 0.6$ s, c) $t = 1.0$ s, d) $t = 1.4$ s

Based on the results of analyses, we have also shear stress accumulations which are represented in Figure 5.62, 5.63, 5.64.

For σ_{12} accumulations:
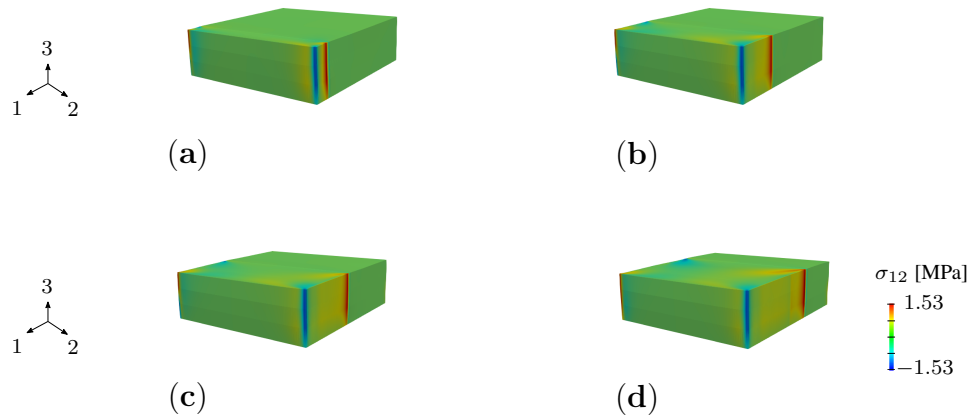
Figure 5.62: σ_{12} simulation for material frontally polymerized at a) $t = 0.2$ s, b) $t = 0.6$ s, c) $t = 1.0$ s, d) $t = 1.4$ s

For σ_{23} accumulations:
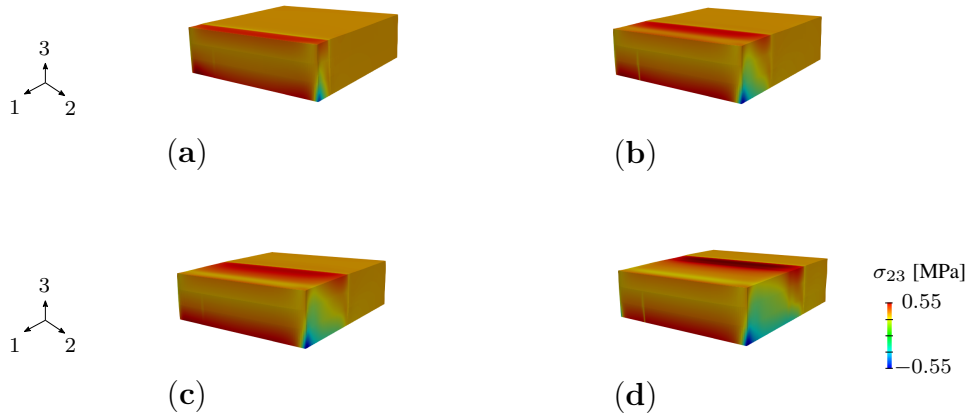
Figure 5.63: σ_{23} simulation for material frontally polymerized at a) $t = 0.2$ s, b) $t = 0.6$ s, c) $t = 1.0$ s, d) $t = 1.4$ s
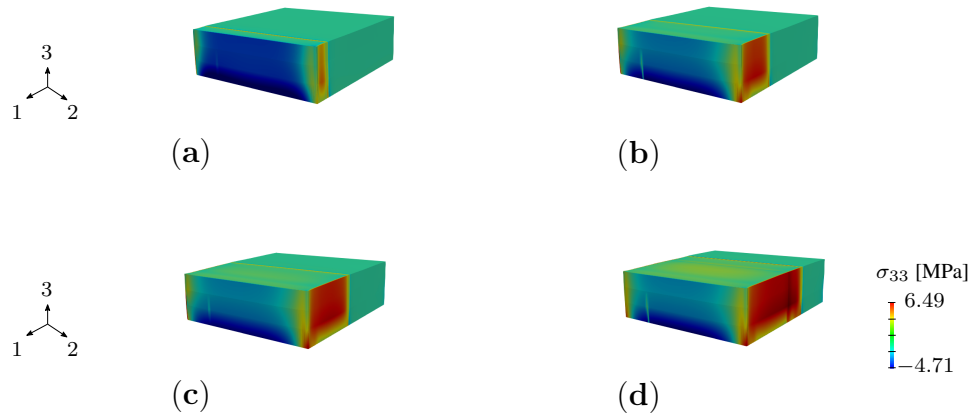
For σ_{13} accumulations:
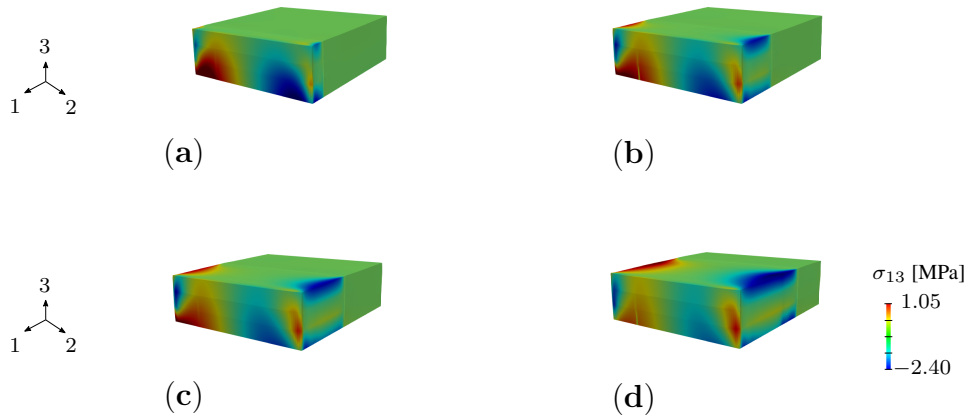
Figure 5.64: σ_{13} simulation for material frontally polymerized at a) $t = 0.2$ s, b) $t = 0.6$ s, c) $t = 1.0$ s, d) $t = 1.4$ s

According to the results of the analysis, we observe that the stress accumulations on the left and right sides of the domain due to the boundary conditions. These stress accumulations act as imperfections, so they lead to strength loss. The material produced by frontal polymerization is used in the high-performance required area. Therefore, they make the importance of the prediction of these stress accumulation even more pronounced.

CHAPTER 6

CONCLUDING REMARKS

6.1 Summary and Conclusions

In this thesis, the thermodynamical constitutive framework and computational model have been developed for the frontally polymerized materials. Frontal polymerization is an alternative curing method based on a self-propagating, self-sustained exothermic reaction front that transforms liquid monomers into cured polymers. Recently, it has been at the forefront of studies on the literature regarding self-autonomous materials. Therefore, many researchers have worked on the thermal and chemical aspects of this emerging curing method. However, until now, to our best knowledge nobody has conducted a study on the thermomechanical aspects of frontal polymerization in the literature. Thus, there is a gap in the scientific literature regarding this issue. In this thesis, a computational model has been developed for the chemo-thermal, and then the chemo-thermo-mechanical coupled problem with the motivation of being the first work to account for the thermo-mechanical coupling.

In Chapter 1, we have overviewed for milestone studies regarding the chemical, thermal, and mechanical aspects of polymerization in the literature. We have examined the thermodynamical settings of each study and paid attention to their mechanical approach during the polymerization process. Then, we have reviewed the papers investigating the chemical and thermal states of frontal polymerization, and we notice that Sottos, Geubelle, and coworkers have recently done remarkable studies in this field. Thus, we have developed our model based on their studies [3].

The thermodynamical framework for frontal polymerization technique has been developed by satisfying thermodynamical restrictions in Chapter 2. We have introduced

the governing differential equations for the solution of the chemo-thermo-mechanical problem of frontal polymerization. Then, we have worked on the theory of frontal polymerization technique and polymerized material behavior.

We have developed an incremental constitutive modeling approach to the chemo-thermo-mechanical coupling for material whose properties evolve through curing in Chapter 3. We have worked on the ordinary differential equation regarding the chemical evolution of curing with the help of the Newton-Raphson method. The contribution of the term that arises from the chemical heating part into the thermal tangent term is removed by using a staggered solution approach. Thanks to this method, the capability of algorithm and computational efficiency are increased. Then, we have developed the incremental elastic model to predict the stress accumulations that accumulates and evolves due to the chemical shrinkage and thermal expansion. Moreover, the thermoelastic model also allows the material properties to evolve with curing, and this satisfies the thermodynamical consistency mentioned in the study conducted by Höfer and Lion [13]. The whole derivation is arranged in the Lagrangean setting and then they are transformed to Eulerian counterparts by push forward operation for the finite element discretization.

In Chapter 4, the finite element method has been developed for the solution of the coupled governing differential equations. Since the staggered solution method has been used, the coupled terms were eliminated and the chemo-thermo-mechanical coupled problem was solved as two independent problems at a time step. During this solution, the temperature values have been taken from the previous time step, and the chemical shrinkage and thermal expansion values have been calculated using this value. Then, the corresponding stress terms have been obtained.

We have considered representative numerical examples for the chemo-thermal and chemo-thermo-mechanical aspects of frontal polymerization in Chapter 5. First we have performed spatial and temporal convergence studies to show the accuracy of our model, and as a result of these studies, we have obtained the optimum size of mesh and time step. Then, we have worked on chemo-thermal numerical examples. These examples are concerned with the case of a planar front, a non-planar front for a composite structure, and a planar front with two-side heating. We have examined that

the chemical and thermal properties of frontal polymerization with these examples. We have concluded that there must be an optimum fiber ratio for the polymerization to be effective for composite structures through our studies. Then, we have calculated and simulated the stress accumulations in the material using our chemo-thermo-mechanical model analyses and the obtained results have revealed that a significant amount of accumulated stresses may lead to a strength loss in the final product polymerized with this method. Furthermore, it has been found that the nature and latent of the stress accumulations depends on both mechanical and thermal boundary conditions. Another important factor has strong effect on the stress accumulations in the internal constraints that are introduced by the composite structure of polymers and the uneven distribution of the degree of polymerization in the product.

6.2 Challenges

The nature of the problem requires a small mesh size and a small time step around the sharp gradient in temperature and the degree of curing front. This situation increased the computational cost of the solution to this problem. In addition, since there was no study in the literature in which both incremental and decomposed deformation gradients, it was a challenging task how to calculate stress. Also, the limited experiments on this field related to stress-strain made it difficult to evaluate the importance of the problem in practice.

The shrinkage of the material due to polymerization after being exposed to very high temperatures caused stability and convergence problems in the solution method.

6.3 Future Studies

The thermodynamical framework that we have developed allows for an incremental elastic material analysis. In future studies, this can be extended to viscoelastic and viscoplastic material models. Moreover, one can work on optimization studies for the ideal polymerization process with different fiber types and ratios and heating protocols. In addition, a model can be developed that considers the evolution mate-

rial properties with respect to the glass transition temperature. These are the studies planned to be conducted in the future.

REFERENCES

[1] I. D. Robertson, M. Yourdkhani, P. J. Centellas, J. E. Aw, D. G. Ivanoff, E. Goli, E. M. Lloyd, L. M. Dean, N. R. Sottos, P. H. Geubelle, J. S. Moore, and S. R. White, "Rapid energy-efficient manufacturing of polymers and composites via frontal polymerization," *Nature*, vol. 557, p. 223227, 2018.

[2] P. Sikdar, M. M. Uddin, T. Dip, S. Islam, M. S. Hoque, A. Dhar, and S. Wu, "Recent advances in smart hydrogels synthesis," *Materials Advances*, 2021.

[3] E. Goli, N. Parikh, M. Yourdkhani, N. Hibbard, J. Moore, N. Sottos, and P. Geubelle, "Frontal polymerization of unidirectional carbon-fiber-reinforced composites," *Composites Part A: Applied Science and Manufacturing*, vol. 130, p. 105689, 2020.

[4] L. M. Dean, Q. Wu, O. Alshangiti, J. S. Moore, and N. R. Sottos, "Rapid synthesis of elastomers and thermosets with tunable thermomechanical properties," *ACS Macro Letters*, vol. 9, no. 6, 2020.

[5] I. Robertson, L. Dean, G. Rudebusch, N. Sottos, S. White, and J. Moore, "Alkyl phosphite inhibitors for frontal ring-opening metathesis polymerization greatly increase pot life," *ACS Macro Letters*, vol. 6, pp. 609–612, 2017.

[6] P. M. Goldfeder and V. A. Volpert, "A model of frontal polymerization using complex initiation," *Mathematical Problems in Engineering*, vol. 5, p. 745605, 1999.

[7] W. Callister and D. Rethwisch, *Materials Science and Engineering*. 2011.

[8] Y. Chekanov, D. Arrington, G. Brust, and J. A. Pojman, "Frontal curing of epoxy resins: Comparison of mechanical and thermal properties to batch-cured materials," *Journal of Applied Polymer Science*, vol. 66, no. 6, pp. 1209–1216, 1997.

[9] S. Davtyan, A. Berlin, and A. Tonoyan, "Advances and problems of frontal polymerization processes," *Review Journal of Chemistry*, vol. 1, pp. 56–92, 2011.

[10] J. Pojman, R. Craven, A. Khan, and W. West, "Convective instabilities in traveling fronts of addition polymerization," *Journal of Physical Chemistry*, vol. 96, pp. 7466–7472, 1992.

[11] Y. Gao, F. Shaon, A. Kumar, S. Bynum, D. Gary, D. Sharp, J. A. Pojman, and P. H. Geubelle, "Rapid frontal polymerization achieved with thermally conductive metal strips," *Chaos: An Interdisciplinary Journal of Nonlinear Science*, vol. 31, no. 7, p. 073113, 2021.

[12] E. Frulloni, M. Salinas, L. Torre, A. Mariani, and J. Kenny, "Numerical modeling and experimental study of the frontal polymerization of the diglycidyl ether of bisphenol a/diethylenetriamine epoxy system," *Journal of Applied Polymer Science*, vol. 96, pp. 1756 – 1766, 2005.

[13] P. Höfer and A. Lion, "On the phenomenological representation of curing phenomena in continuum mechanics," *Archive of Mechanics*, vol. 59, p. 5989, 2007.

[14] P. Haupt and A. Lion, "On finite linear viscoelasticity of incompressible isotropic materials," *Acta Mechanica*, vol. 159, pp. 87–124, 2002.

[15] M. Hossain, G. Possart, and P. Steinmann, "A small-strain model to simulate the curing of thermosets," *Computational Mechanics*, vol. 43, p. 769779, 2009.

[16] M. Hossain, G. Possart, and P. Steinmann, "A finite strain framework for the simulation of polymer curing. part i: elasticity," *Computational Mechanics*, vol. 44, p. 621630, 2009.

[17] A. Lion and P. Höfer, "On the phenomenological representation of curing phenomena in continuum mechanics1," *Archives of Mechanics*, vol. 59, 2007.

[18] M. Hossain, G. Possart, and P. Steinmann, "A finite strain framework for the simulation of polymer curing. part ii. viscoelasticity and shrinkage," *Computational Mechanics*, vol. 46, p. 363375, 2009.

[19] P. Sreejith, K. Kannan, and K. Rajagopal, "A thermodynamic framework for additive manufacturing, using amorphous polymers, capable of predicting residual stress, warpage and shrinkage," *International Journal of Engineering Science*, p. 103412, 2021.

[20] K. Rajagopal and A. Srinivasa, "A thermodynamic frame work for rate type fluid models," *Journal of Non-Newtonian Fluid Mechanics*, vol. 88, pp. 207–227, 2000.

[21] T. Sain, K. Loeffel, and S. Chester, "A thermo-chemo-mechanically coupled constitutive model for curing of glassy polymers," *Journal of the Mechanics and Physics of Solids*, vol. 116, 2018.

[22] T. N'Guyen, S. Lejeunes, D. Eyheramendy, and A. Boukamel, "A thermodynamical framework for the thermo-chemo-mechanical couplings in soft materials at finite strain," *Mechanics of Materials*, vol. 95, 2016.

[23] R. Saito, Y. Yamaguchi, S. Matsubara, S. Moriguchi, Y. Mihara, T. Kobayashi, and K. Terada, "Decoupled two-scale viscoelastic analysis of frp in consideration of dependence of resin properties on degree of cure," *International Journal of Solids and Structures*, vol. 190, pp. 199–215, 2020.

[24] Y. Yamanaka, S. Matsubara, R. Saito, S. Moriguchi, and K. Terada, "Thermo-mechanical coupled incremental variational formulation for thermosetting resins subjected to curing process," *International Journal of Solids and Structures*, vol. 216, pp. 30–42, 2021.

[25] E. Tadmor, R. Miller, and R. Elliott, "Continuum mechanics and thermodynamics," *Continuum Mechanics and Thermodynamics*, 2011.

[26] M. Silhavy, *The Mechanics and Thermodynamics of Continuous Media*. 2002.

[27] A. Munjiza, E. Rougier, and E. Knight, *Large Strain Finite Element Method: A Practical Course*. 2014.

[28] N. Ottosen and M. Ristinmaa, *The Mechanics of Constitutive Modeling*. 2005.

[29] P. Haupt, *Continuum Mechanics and Theory of Materials*, vol. 55. 2002.

[30] B. Coleman and M. Gurtin, "Thermodynamics with internal state variables," *The Journal of Chemical Physics*, vol. 47, pp. 597–613, 1967.

[31] K. Loeffel and L. Anand, "A chemo-thermo-mechanically coupled theory for elastic–viscoplastic deformation, diffusion, and volumetric swelling due to a

chemical reaction," *International Journal of Plasticity*, vol. 27, pp. 1409–1431, 2011.

[32] Z. Bazant, "Thermodynamics of solidifying or melting viscoelastic material," *Journal of the Engineering Mechanics Division*, vol. 105, pp. 933–952, 1979.

[33] R. Lackner and H. Mang, "Chemoplastic material model for the simulation of early-age cracking: From the constitutive law to numerical analyses of massive concrete structures," *Cement and Concrete Composites*, vol. 26, pp. 551–562, 2004.

[34] R. Taylor and S. Govindjee, "FEAP-finite element analysis program," 2017.

[35] S. Kovačič and C. Slugovc, "Ring-opening metathesis polymerisation derived poly(dicyclopentadiene) based materials," *Materials Chemistry Frontiers*, vol. 4, 2020.

[36] V. Toplosky and R. Walsh, "Thermal and mechanical properties of poly-dicyclopentadiene (dcpd) at cryogenic temperatures," *AIP Conference Proceedings*, vol. 824, pp. 219–224, 2006.

[37] M. Minus and S. Kumar, "The processing, properties, and structure of carbon fibers," *JOM*, vol. 57, pp. 52–58, 2005.

[38] U. Stirna, I. Beverte, V. Yakushin, and U. Cabulis, "Mechanical properties of rigid polyurethane foams at room and cryogenic temperatures," 2011.